
This manuscript is a **preprint** and has been submitted for publication in **Sedimentology**. This version of the manuscript has not undergone peer-review. Subsequent versions of the manuscript may have slightly different content. If accepted, the final version of this manuscript will be available via the “Peer-reviewed Publication” DOI link on the right-hand side of this webpage. Please feel free to contact any of the authors directly to comment on the manuscript.

November 25th, 2020

1 **Reconstructing the morphologies and hydrodynamics of ancient rivers from source to sink:**
2 **Cretaceous Western Interior Basin, Utah, USA**

3 **Sinéad J. Lyster^{1*}**, Alexander C. Whittaker¹, Gary J. Hampson¹, Elizabeth A. Hajek², Peter A. Allison¹
4 and Bailey A. Lathrop¹

5 ¹ *Department of Earth Science and Engineering, Imperial College London, London, UK.*

6 ² *Department of Geosciences, The Pennsylvania State University, Pennsylvania, USA.*

7 **s.lyster17@imperial.ac.uk*

8 **(A) Abstract**

9 Quantitative reconstruction of palaeohydrology from fluvial stratigraphy provides sophisticated
10 insights into the response, and relative impact, of tectonic and climatic drivers on ancient fluvial
11 landscapes. Here, field measurements and a suite of quantitative approaches are used to develop a
12 four-dimensional (space and time) reconstruction of palaeohydrology in Late Cretaceous palaeorivers
13 of central Utah, USA — these rivers drained the Sevier mountains to the Western Interior Seaway.
14 Field data include grain-size and cross-set measurements and span 5 parallel fluvial systems, 2 of
15 which include up-dip to down-dip transects, across 7 stratigraphic intervals through the Blackhawk
16 Formation, Castlegate Sandstone and Price River Formation. Reconstructed palaeohydrological
17 parameters include fluvial morphologies (flow depths, palaeoslopes, palaeorelief, and planform
18 morphologies) and various hydrodynamic properties (flow velocities, water discharges, and sediment
19 transport modes). Results suggest that fluvial morphologies were similar in space and time; median
20 flow depths spanned 2–4 m with marginally greater flow depths in southerly systems. Meanwhile
21 palaeoslopes spanned 10^{-3} to 10^{-4} , decreasing downstream by an order of magnitude. The most
22 prominent spatio-temporal change is an up to 4-fold increase in palaeoslope at the Blackhawk–
23 Castlegate transition; associated alluvial palaeorelief is 10s of metres during Blackhawk deposition and
24 >100 m during Castlegate Sandstone deposition. Unit water discharges do not change at the
25 Blackhawk–Castlegate transition, which argues against a climatically driven increase in palaeoslope
26 and channel steepness. These findings instead point to a tectonically driven palaeoslope increase,
27 although one limitation in this study is uncertainty in palaeochannel widths, which directly influences
28 total water discharges. These reconstructions complement and expand on extensive previous work in
29 this region, which enables us to test the efficacy of quantitative reconstruction tools. Comparison of
30 results with facies-based interpretations indicates that quantitative tools work well, but
31 inconsistencies in more complex reconstructions (e.g. planform morphologies) highlight the need for
32 further work.

33 **(A) Introduction**

34 The stratigraphic record is a fundamental physical archive of Earth surface processes in space and time
35 (Wobus et al., 2006; Allen, 2008a, 2008b; Armitage et al., 2011; Whittaker, 2012). A key research
36 challenge is to decode this archive to reconstruct the movement of water and sediment across Earth's
37 surface in the geological past (Castelltort & Van Den Driessche, 2003; Jerolmack & Paola, 2010; Ganti
38 et al., 2014; Romans et al., 2016; Straub et al., 2020) — effective quantification of palaeohydrology

39 from fluvial stratigraphy is crucial to achieve this goal. Constraints on the morphologies and
40 hydrodynamics of palaeorivers can be used to: resolve the size and scale of ancient catchments
41 (Bhattacharya & Tye, 2004; Bhattacharya et al., 2016; Eide et al., 2018; Lyster et al., 2020); quantify
42 sediment transport capacities and the magnitudes of sediment exported to oceans (Allen et al., 2013;
43 Holbrook & Wanas, 2014; Lin & Bhattacharya, 2017; Sharma et al., 2017); decipher fluvial response to
44 perturbation (Foreman et al., 2012; Foreman, 2014; Colombera et al., 2017; Chen et al., 2018); and
45 reconstruct local palaeogeographies (Li et al., 2018). Importantly, these constraints can be used to
46 investigate hydrological response to long-period forcing ($>10^6$ yrs) as river behaviour is intrinsically
47 linked to tectono-climatic boundary conditions over geological timescales (Duller et al., 2010;
48 Whitchurch et al., 2011; Whittaker et al., 2011; Castelltort et al., 2012; Hampson et al., 2013).

49 However, palaeohydrology is limited by incomplete (or absent) records of palaeorivers (Sadler, 1981;
50 Jerolmack & Sadler, 2007), uncertainty as to what information fluvial stratigraphy actually preserves
51 (Castelltort & Van Den Driessche, 2003; Jerolmack & Paola, 2010; Romans et al., 2016; Straub et al.,
52 2020), and uncertainties associated with data type, data measurement, and reconstruction tools (e.g.
53 Bridge & Tye, 2000). Where it is possible to overcome these challenges, the ability to decipher
54 palaeohydrological information with high fidelity can enable sophisticated insights to be drawn about
55 the sensitivity and response of ancient fluvial systems to tectonic and climatic drivers.

56 Here, a quantitative framework is used to reconstruct the palaeohydrological evolution of well-known
57 source-to-sink systems of Late Cretaceous central Utah, USA. The focus of this study is the Blackhawk
58 Formation–Castlegate Sandstone–Price River Formation fluvial succession as outcrops are extensive
59 and well-documented (Kauffman, 1977; Kauffman & Caldwell, 1993; Cobban et al., 2006). These strata
60 represent eastward flowing palaeorivers that drained the Sevier orogenic fold-and-thrust belt to the
61 Western Interior Seaway (WIS). Previous work has primarily focused on *qualitative* inferences of
62 palaeohydrology in these systems (Miall, 1994; Miall & Arush, 2001; Adams & Bhattacharya, 2005;
63 McLaurin & Steel, 2007; Hampson et al., 2012; Flood & Hampson, 2014), which are sometimes
64 complimented by simple quantitative reconstructions (e.g. Hampson et al., 2013). Meanwhile,
65 *quantitative* work has mostly focused on architectural-scale elements in these systems, including
66 preservation of channelized bodies and bars and associated autogenic processes, such as avulsion and
67 backwater dynamics (Hajek et al., 2010; Hajek & Wolinsky, 2012; Flood & Hampson, 2015; Trower et
68 al., 2018; Chamberlin & Hajek, 2019; Ganti et al., 2019a). The palaeohydrological evolution of these
69 rivers at the system scale has not been comprehensively addressed using quantitative tools — this
70 study addresses this outstanding research challenge to shed new light on these ancient systems.

71 Palaeohydrological field data were collected for 5 parallel transverse fluvial systems (spaced ~20–25
72 km apart) across 7 stratigraphic intervals within the Campanian stage (83.6 ± 0.2 to 72.1 ± 0.2 Ma) of the
73 Late Cretaceous, which spanned 11.5 Myr (Figs 1, 2). These data allow for high resolution spatio-
74 temporal reconstructions of these systems, both up-dip to down-dip and along depositional strike (Fig.
75 1). Reconstructed palaeohydrologic parameters include: flow depths; palaeoslopes and palaeorelief
76 (specific to the alluvial domain); hydrodynamic properties, including flow velocities, water discharges
77 and sediment transport modes; and planform morphologies. First and foremost, results show how the
78 morphologies and hydrodynamic properties of these palaeorivers varied in space and time. Moreover,
79 reconstruction of palaeoslopes and palaeorelief in the alluvial domain enable evaluation of the
80 competing roles of tectonic and climatic drivers on the evolution of these ancient rivers. Finally, the

81 results provide new insights regarding the extent to which quantitative palaeohydrologic methods
82 (which are increasingly borrowed from the field of engineering) can be reconciled with
83 sedimentological observables.

84 **(A) Research background**

85 **(B) Palaeohydrology**

86 Palaeohydrological interpretations traditionally derive from analysis of facies associations in fluvial
87 strata, particularly of architectural-scale elements (Miall, 1994; Miall & Arush, 2001; Adams &
88 Bhattacharya, 2005; McLaurin & Steel, 2007; Hampson et al., 2012; Hampson et al., 2013; Flood &
89 Hampson, 2014), and increasingly take advantage of high-resolution remote imagery and three-
90 dimensional outcrop models (Hajek & Heller, 2012; Rittersbacher et al., 2014; Chamberlin & Hajek,
91 2019). However, a combination of empirical, theoretical and experimental work has led to the
92 development of fluid and sediment transport models that are applicable to geologic questions (e.g.
93 van Rijn, 1984b; Ferguson & Church, 2004; Parker, 2004; Wright & Parker, 2004; Mahon & McElroy,
94 2018), enabling more sophisticated inferences of palaeohydrology from the rock record.

95 Recent quantitative research has focused on maximising the ability to accurately reconstruct the
96 evolution of fluvial landscapes in the geologic past. Some efforts have centred on connecting
97 landscape surface kinematics to stratal preservation (Paola & Borgman, 1991; Castelltort & Van Den
98 Driessche, 2003; Jerolmack & Mohrig, 2005; Jerolmack & Paola, 2010; Hajek & Wolinsky, 2012; Ganti
99 et al., 2013; Ganti et al., 2014; Reesink et al., 2015; Romans et al., 2016; Ganti et al., 2020; Leary &
100 Ganti, 2020; Straub et al., 2020) and a number of these studies have focused on Late Cretaceous fluvial
101 strata in central Utah (Flood & Hampson, 2015; Trower et al., 2018; Chamberlin & Hajek, 2019; Ganti
102 et al., 2019a). Meanwhile, other quantitative work has applied fluid and sediment transport models
103 to stratigraphic field data, with an overarching goal of constraining the characteristics of catchments,
104 regional systems or entire fluvial landscapes in the geological past (Ganti et al., 2019b; Lapôtre et al.,
105 2019), or even on other planetary bodies (Lamb et al., 2012; Buhler et al., 2014; Hayden et al., 2019;
106 Lapôtre et al., 2019). This includes using quantitative palaeohydrological tools to reconstruct water
107 and sediment discharges within mass balance frameworks (Holbrook & Wanas, 2014; Lin &
108 Bhattacharya, 2017; Sharma et al., 2017), decipher local palaeogeographies (Bhattacharyya et al.,
109 2015; Li et al., 2018), characterise pre-vegetation rivers (Ganti et al., 2019b), and reconstruct fluvial
110 response to climatic perturbations for well-preserved fluvial strata straddling events such as the
111 Paleocene–Eocene Thermal Maximum (PETM) (Foreman et al., 2012; Foreman, 2014; Colombera et
112 al., 2017; Chen et al., 2018; Duller et al., 2019).

113 Despite the breadth of quantitative palaeohydrological tools available, previous applications to fluvial
114 stratigraphic field data have typically centred on individual catchments and instantaneous or short-
115 period intervals (i.e. individual discharge events and mean annual discharges) (Holbrook & Wanas,
116 2014; Lin & Bhattacharya, 2017; Sharma et al., 2017), or reconstructions across stratigraphic
117 boundaries and short-period tectono-climatic events, such as the PETM (Foreman et al., 2012;
118 Foreman, 2014; Colombera et al., 2017; Chen et al., 2018; Duller et al., 2019). Far fewer studies have
119 focused on long-period intervals, such as the evolution of source-to-sink systems across geologic
120 timescales ($>10^6$ yrs). This outstanding opportunity can be exploited in Late Cretaceous fluvial systems

121 of central Utah, where outcrop availability supports a four-dimensional (space and time) study in a
122 region subject to active tectonics, spanning both Sevier and Laramide deformation.

123 **(B) Tectono-geographic setting and palaeodrainage**

124 Input of sediment to the Late Cretaceous WIS was dominated by the western margin, where rivers
125 draining the active Sevier fold-and-thrust belt eroded and transported huge volumes of clastic
126 sediments eastwards into the foreland basin (Spieker, 1946; Armstrong, 1968; Kauffman, 1977; Hay
127 et al., 1993; Kauffman & Caldwell, 1993) (Fig. 1b,c). This led to the deposition and progradation of a
128 large, asymmetric clastic wedge on the western WIS margin. This study focuses on Campanian non-
129 marine clastic sediments of this wedge in central Utah, USA (Figs 1–3), where palaeodrainage is
130 relatively well-constrained (Bartschi et al., 2018; Pettit et al., 2019). Multiple transverse fluvial systems
131 drained the Sevier thrust belt in this area (Fig. 1b). Several studies have additionally interpreted an
132 axial, or longitudinal, fluvial system that drained north–northeast from the Mogollon Highlands
133 (present day central Arizona) and Cordilleran magmatic arc, which interacted with transverse systems
134 of the Sevier thrust belt (Lawton et al., 2003; Jinnah et al., 2009; Szwarc et al., 2015) (Fig. 1b) and led
135 to downsystem sediment mixing (Bartschi et al., 2018; Pettit et al., 2019). Detrital zircon (DZ) data
136 (Bartschi et al. (2018) indicate that these fluvial systems were dominated by a thrust-belt source in
137 close proximity to the Sevier thrust front, but that more southerly transverse systems may have
138 additionally featured a longitudinal component of drainage (Bartschi et al., 2018; Pettit et al., 2019).
139 Herein, focus is on transverse fluvial systems that predominantly drained the Sevier mountains (Fig.
140 1).

141 Tectonic forcing in this region is well studied (DeCelles, 1994, 2004; DeCelles & Coogan, 2006) and
142 palaeoclimate has been reconstructed from a variety of palaeontological, geochemical-proxy and
143 modelling studies (e.g. Wolfe & Upchurch Jr., 1987; Fricke et al., 2010; Miller et al., 2013; Sewall &
144 Fricke, 2013; Foreman et al., 2015). In central Utah, eastward propagation of the Sevier thrust belt
145 (due to eastward subduction of the Farallon plate) resulted in thin-skinned deformation and
146 movement on the north–south trending Canyon (~145–110 Ma), Pahvant (~110–86 Ma), Paxton
147 (86–75 Ma) and Gunnison (75–65 Ma) thrust systems (DeCelles, 1994, 2004; DeCelles & Coogan,
148 2006). Associated exhumation created substantial topographic relief in the Sevier mountains, which
149 has been described as “Andean” in scale with mean elevations approaching near 4000 m (Sewall &
150 Fricke, 2013; Foreman et al., 2015). Modelling results and stable isotope evidence suggest a strong
151 monsoonal precipitation along the eastern flank of the Sevier mountains and seasonal flooding across
152 low-relief regions (Roberts, 2007; Roberts et al., 2008; Fricke et al., 2010; Sewall & Fricke, 2013). The
153 tectono-geographic set-up of the Western Interior was particularly conducive to a monsoonal climate
154 — the proximity of a warm sea to high elevation mountains commonly results in strong seasonal
155 precipitation and convective circulation (e.g. Zhisheng et al., 2001). A seasonal temperate-to-
156 subtropical climate therefore prevailed throughout Campanian deposition (L. R. Parker, 1976;
157 Kauffman & Caldwell, 1993; Roberts & Kirschbaum, 1995). The Campanian onset of thick-skinned
158 deformation as the subducting Farallon plate transitioned to lower-angle, or flat-slab, subduction
159 (DeCelles, 2004) began to manifest as basement-cored Laramide uplifts (e.g. San Rafael Swell, central
160 Utah, and Uinta Mountains, northern Utah), which partitioned the Sevier foreland basin and disrupted
161 patterns of both regional subsidence and drainage (Bartschi et al., 2018; Pettit et al., 2019).

162 **(B) Stratigraphic framework**

163 Establishing a consistent stratigraphic framework in space and time is crucial for system scale
164 palaeohydrological reconstructions. Here, focus is on the Upper Cretaceous Mesaverde Group and up-
165 dip equivalents (Figs 1, 2) in central Utah, USA, specifically fluvial sediments situated less than ~100
166 km from the Sevier orogenic front (DeCelles & Coogan, 2006) in the flexurally subsiding foredeep (Fig.
167 3). These sediments include the Blackhawk Formation, Castlegate Sandstone and Price River
168 Formation along the eastern front of the Wasatch Plateau (Figs 1–3). Up-dip, on the western Wasatch
169 Plateau, the Blackhawk–Castlegate–Price River succession is correlated with the Sixmile Canyon
170 Formation (Indianola Group) and the Price River Conglomerate (following Robinson and Slingerland
171 (1998); Horton et al. (2004); Aschoff and Steel (2011b, 2011a)) (Figs 1–3). Up-dip to down-dip, these
172 sediments encompass the entire alluvial domain of these palaeorivers draining the Sevier highlands.
173 A broad summary of field sites and the stratigraphic framework (Figs 1, 2) is given below — extended
174 information regarding regional stratigraphy and correlations is provided in the Supplementary
175 Material.

176 Down-dip field sites were grouped spatially into 5 field areas that represent 5 parallel transverse fluvial
177 systems draining the Sevier thrust front: Price Canyon, Wattis Road, Straight Canyon (including Joe’s
178 Valley Reservoir), Link Canyon and Salina Canyon (Figs 1, 3). These 5 field areas are approximately ~50
179 km from up-dip alluvial fan lobes (Figs 1, 3). Assuming typical outlet spacings of rivers draining
180 orogenic fronts (~25 km) (Hovius, 1996), it is likely that these field areas represent 5 distinct
181 palaeorivers and form a ~125 km transect along depositional strike. For the 2 up-dip to down-dip
182 transects (Fig. 1), the northern transect included 4 field areas: Dry Hollow, Lake Fork, Bear Canyon,
183 and terminating at Price Canyon (Fig. 3c–e), and the southern transect included 3 field areas: Mellor
184 Canyon, Sixmile Canyon, and terminating at Straight Canyon (Fig. 3d–f). These transects follow those
185 widely implemented in previous work, both along-strike (Hampson et al., 2012; Hampson et al., 2013;
186 Flood & Hampson, 2014, 2015; Chamberlin & Hajek, 2019) and up-dip to down-dip (Robinson &
187 Slingerland, 1998; Horton et al., 2004; Aschoff & Steel, 2011b, 2011a).

188 In addition to grouping field sites in space, they were also grouped in time. In this study 7 stratigraphic
189 intervals were defined: 1 = lower Blackhawk Formation; 2 = middle Blackhawk Formation; 3 = upper
190 Blackhawk Formation; 4 = lower Castlegate Sandstone; 5 = middle Castlegate Sandstone; 6 = upper
191 Castlegate Sandstone (Bluecastle Tongue); 7 = (lowermost) Price River Formation (Fig. 2).

192 Down-dip, on the eastern front of the Wasatch Plateau, it is straightforward to assign sediments of
193 the Blackhawk–Castlegate–Price River succession to the appropriate “space–time” interval by facies
194 associations, following extensive work that has been undertaken in this region (Lawton, 1983, 1986b;
195 Miall, 1994; van Wagoner, 1995; Yoshida et al., 1996; Miall & Arush, 2001; Lawton et al., 2003; Adams
196 & Bhattacharya, 2005; Hampson et al., 2012; Hampson et al., 2013; Flood & Hampson, 2014; Hampson
197 et al., 2014; Flood & Hampson, 2015). The lower–middle Campanian Blackhawk Formation represents
198 deposition on coastal plains behind wave-dominated deltaic shorelines which, up-section, pass
199 landward into alluvial and fluvial plains (Hampson, 2010; Hampson et al., 2012; Hampson et al., 2013).
200 The size and abundance of channelized fluvial sand bodies (deposited by both single- and multi-thread
201 rivers) increase from base to top of the Blackhawk Formation (Adams & Bhattacharya, 2005; Hampson
202 et al., 2012; Hampson et al., 2013; Flood & Hampson, 2015). The middle–upper Campanian Castlegate
203 Sandstone is situated atop the Blackhawk Formation and is an extensive, cliff-forming river-dominated
204 deposit. The lower Castlegate Sandstone and upper Castlegate Sandstone (Bluecastle Tongue)
205 comprise amalgamated braided fluvial channel-belt deposits, whereas the middle Castlegate

206 Sandstone comprises less amalgamated, more meandering, fluvial channel-belt deposits with
207 interbedded mudstones (Fouch et al., 1983; Lawton, 1986b; Miall, 1994; van Wagoner, 1995; Yoshida
208 et al., 1996; Miall & Arush, 2001). The ledge-forming upper Campanian Price River Formation sits
209 conformably atop the Castlegate Sandstone and comprises large channelized sand bodies with
210 interbedded siltstones and mudstones — channelized sand bodies form ~75% of the formation
211 (Lawton, 1983, 1986b). Fluvial sediments of the Price River Formation represent the end of Sevier
212 thrusting; the late Maastrichtian–Eocene North Horn Formation unconformably overlies the Price
213 River Formation.

214 Up-dip, on the western Wasatch Plateau, correlative strata include more proximal sediments of the
215 Indianola Group and Price River Formation, which is now known to not be time-equivalent with the
216 down-dip Price River Formation exposed near Price, Utah (Robinson & Slingerland, 1998; Horton et
217 al., 2004; Aschoff & Steel, 2011b, 2011a). To avoid confusion, these up-dip strata are here referred to
218 as the Price River Conglomerate, following Aschoff and Steel (2011b, 2011a). Up-dip to down-dip
219 correlations are limited by incomplete exposure on the western Wasatch Plateau and difficulty in
220 dating conglomerates (see Supplement). Nevertheless, Robinson and Slingerland (1998) used
221 palynology to correlate these strata across a variety of localities on the Wasatch Plateau (Fig. 2), which
222 can be traced in seismic reflection data (Horton et al., 2004). The up-dip Price River Conglomerate is
223 time-correlative with the down-dip lower, middle, and upper Castlegate Sandstone, and Price River
224 Formation (Robinson & Slingerland, 1998; Horton et al., 2004; Aschoff & Steel, 2011b, 2011a), and is
225 characterised by quartzite-dominated synorogenic conglomerates and few gravel–sand fluvial bodies
226 (Robinson & Slingerland, 1998; Aschoff & Steel, 2011b, 2011a). Of the Indianola Group, the upper
227 Sixmile Canyon Formation is time-correlative with the Blackhawk Formation (Lawton, 1982; Fouch et
228 al., 1983; Lawton, 1986b) and is predominantly characterised by synorogenic gravel–sand fluvial
229 facies, spanning polymictic fluvial conglomerates to medium–coarse-grained sandstones (Lawton,
230 1982, 1986a, 1986b). Here a conservative approach is taken to up-dip to down-dip correlations; the
231 upper Sixmile Canyon Formation of the Indianola Group (intervals 1–3) is time-averaged, and the Price
232 River Conglomerate (intervals 4–7) is also time-averaged, but exceptions were made where field sites
233 were known to be situated at either the top of the upper Sixmile Canyon Formation or at the top/base
234 of the Price River Conglomerate. A full description of these correlations, including new logging in
235 Mellor Canyon, is presented in the Supplement.

236 Each depositional-dip transect is pinned at the most downstream location, i.e. it is assumed that the
237 most down-dip sites in each transect (Price Canyon and Straight Canyon) are approximately parallel
238 and at the same downstream distance. Transects then work upstream, such that the most up-dip field
239 site (Dry Hollow; northern transect) is at a downstream distance of 0 km. Downstream distances follow
240 Robinson and Slingerland (1998) —post-depositional extension is not corrected for. Alternatively,
241 when reconstructing along-depositional-strike transects, transects are pinned at the most northern
242 location (Price Canyon) with an along-strike distance of 0 km, meanwhile southern locations have
243 along-depositional-strike distances up to 125 km.

244 **(A) Methods**

245 Data were collected from channel-fill stratigraphy (cross-stratified sandstone and gravel deposits are
246 interpreted as channel floor deposits) and were time-averaged across each stratigraphic space–time
247 interval (field sites are listed in Supplementary Table S2). These field data, including uncertainties,

248 were propagated through a quantitative framework to reconstruct the morphologies and
249 hydrodynamics (flow depths, palaeoslopes, river long profiles, flow velocities and discharges,
250 sediment transport modes and likely planform morphologies) of palaeorivers in both space and time.

251 **(B) Field observations**

252 **(C) Grain size**

253 At each field site the coarse-fraction (>2 mm in diameter) and sand-fraction (<2 mm in diameter) grain-
254 sizes of channel-fill deposits were established (Fig. 4a,b). For coarse-fractions, grain-size distributions
255 were measured via Wolman point counts (Wolman, 1954) (Fig. 4a); this technique has been
256 successfully used to decode spatio-temporal trends in grain-size (e.g. Whittaker et al., 2011; D'Arcy et
257 al., 2017; Brooke et al., 2018). For sand-fractions, scaled photographs were processed in *ImageJ*
258 software and, similarly, the long axis of a minimum of 50 randomly selected grains was measured to
259 recover grain-size distributions (Fig. 4b). From each measured grain-size distribution, the median
260 grain-size, D_{50} , and 84th percentile, D_{84} , were extracted. Where grain-size facies were disparate, e.g.
261 gravel topped with sand, data were collected for each grain-size facies and the proportions of each
262 were estimated (Fig. 4c).

263 In order to achieve representative sampling for spatio-temporal grain-size trends, multiple grain-size
264 observations were collected at each field site. Not only were data collected for each grain-size facies
265 (Fig. 4a–c), but depending on overall outcrop extent Wolman point counts were repeated and/or
266 additional scaled photographs were taken for *ImageJ* processing at intermittent stratigraphic intervals
267 (e.g. one count per 5–10 m of strata or per channelized body). The extent of each field site can be
268 approximated as the extent of outcrop apparent in Fig. 3c–h. From these data an average grain-size
269 was produced for both the sand-fraction and gravel-fraction at each field site. As each space–time
270 interval includes multiple field sites, this results in multiple average sand- and gravel-fraction grain-
271 sizes, capturing channel-fill deposits from several channelized bodies. Finally, a bulk-grain-size was
272 produced for each space–time interval using the gravel-to-sand proportions at each field site — each
273 site within a space–time interval was assigned equal weighting. Further information regarding grain-
274 size data collection, including axis selection, sample size sufficiency and weighting, is presented in the
275 Supplement.

276 **(C) Cross-sets**

277 Cross-set heights were measured as these data can be used to reconstruct original bedform heights
278 and formative flow depths. Trough- and planar-cross bedding, which are inherently indicative of
279 bedload transport, were present at nearly all field sites. They occurred predominantly in sand-grade
280 deposits, but also in granule- to pebble-grade deposits (Fig. 4d–f). To establish mean cross-set heights,
281 the sampling strategy of Ganti et al. (2019b) was followed. Cross-set boundaries (i.e. the lower,
282 asymptotic bounding surface and the upper, erosional bounding surface) were delineated and then
283 heights were measured at regular intervals along the entire width of the cross-set dip-section (Fig. 4g–
284 i). Measurements were made to a precision of ± 5 mm. This protocol was repeated for individual cross-
285 sets within co-sets to establish a mean cross-set height for each individual cross-set. Subsequently,
286 maximum cross-set heights (i.e. the maximum distance between lower and upper bounding surfaces)
287 were measured for a representative sample across the exposed outcrop (usually $n=25-50$).

288 Cross-set distributions (n=470) were used to establish the mean, 84th percentile (P_{84}) and maximum
289 height for each individual cross-set, and relationships between each were established for the field
290 area. These new relationships were then used to estimate mean cross-set heights from all measured
291 maximum cross-set heights (n=4053), and these estimates of mean cross-set heights were propagated
292 through subsequent calculations.

293 **(C) Channel geometry and architectural element data**

294 Above grain- and bedform-scales, channel geometries and major architectural elements were also
295 measured, where possible, using a Haglof Laser Geo laser range finder to a precision of ± 5 cm. This
296 included maximum channel body/story thicknesses and bar-scale clinof orm heights. Previous work in
297 this region has documented the dimensions and distributions of fluvial architectural elements using
298 high-resolution imagery and 3D outcrop models (Hajek & Heller, 2012; Rittersbacher et al., 2014; Flood
299 & Hampson, 2015; Chamberlin & Hajek, 2019). Field data collection therefore focused on grain-size
300 and cross-set measurements, with compilation of published secondary data (alongside new data from
301 this study) to augment field data and evaluate our palaeohydrological reconstructions (see
302 Supplementary Tables S4, S5).

303 **(B) Quantitative palaeohydrology**

304 **(C) Channel geometries**

305 To calculate original bedform heights from cross-set measurements, the relation of Leclair and Bridge
306 (2001) was used, which is based on theoretical work by Paola and Borgman (1991). Leclair and Bridge
307 (2001) showed that mean bedform (i.e. dune) height, h_d , can be approximated as a function of mean
308 cross-set height, h_{xs} , where

$$310 \quad h_d = 2.9(\pm 0.7) h_{xs}. \quad \text{Eq. 1}$$

311 While bedform height generally scales with flow depth, the mechanistic explanation for this is not fully
312 resolved. As such, many scaling relations simply relate bedform height and flow depth (e.g. Yalin,
313 1964), whereas some incorporate additional parameters such as Froude number, D_{50} , and transport
314 stage (e.g. Gill, 1971; van Rijn, 1984a), however their incorporation does not improve predictive
315 power. Bradley and Venditti (2017) revisited previous bedform height–flow-depth scaling relations
316 and derived a new relation between h_d and median formative flow depth, H , based on >380 field
317 observations:

$$318 \quad H = 6.7h_d, \quad \text{Eq. 2}$$

320 with the 1st and 3rd quartiles estimated by $H=4.4h_d$ and $H=10.1h_d$, respectively. Bradley and Venditti
321 (2017) proposed that their relations for the 1st and 3rd quartiles of H offer useful probability bounds
322 on palaeoflow depths. As such, the 1st and 3rd quartiles of H (carrying forward the error on Equation
323 1) were also calculated, and these values were carried throughout subsequent calculations to offer

324 reasonable bounds for the likely spread of values for each parameter. Where cross-bedding was
325 absent (i.e. the most up-dip field sites), channel-body thicknesses were used as a proxy for flow depth.

326 Similar to H , channel width, W , can be estimated using scaling relations as direct measurement is not
327 normally possible from outcrop. Bridge and Mackey (1993) proposed the relation $W=8.8H^{1.82}$ for
328 single-thread channels. Alternatively, widths of fully-braided channel systems can be approximated
329 as, for example, $W=42H^{1.11}$ (Leopold & Maddock Jr, 1953). However, estimates of W from outcrop data
330 and scaling relations are particularly tentative and, where systems are braided, subject to further
331 uncertainty pertaining to the number of threads. As such, results in this study are reported per unit
332 width.

333 (C) Palaeoslopes and palaeorelief

334 Palaeoslopes were estimated using 2 independent methodologies, adapted from Ganti et al. (2019a).
335 First, Shields stress, τ^* , was estimated using the bedform stability diagram of Carling (1999), which
336 expresses bedform stability in terms of τ^* and D_{50} (for $D_{50} < 33$ mm). Minimum and maximum bounds
337 of τ^* for the stable existence of dunes were then identified for a range of D_{50} values. Where D_{50}
338 exceeded 33 mm, and in the absence of bedforms, a range of possible τ^* values of 0.04–0.06 were
339 assigned. Then, 10^6 uniformly distributed random samples of τ^* were generated between these
340 bounds, as well as 10^6 uniformly distributed random samples of H (between the 1st and 3rd quartile).
341 To reconstruct palaeoslope, S , bed shear stress, τ_b , was approximated as the depth–slope product
342 ($\tau_b = \rho g H S$) and then S can be given as

$$344 \quad S = \frac{R D_{50} \tau^*}{H},$$

343 Eq. 3

345 where R is the dimensionless submerged specific gravity of sediment in water (1.65 for quartz) and H
346 is the flow depth (ρ is density and g is acceleration due to gravity). Similarly, 10^6 values of S were
347 recovered and the median S , as well as the 1st and 3rd quartile of S , were extracted.

348 For the second approach, the method of Trampush et al. (2014) was used, which is based on Bayesian
349 regression analysis of bankfull measurements in modern alluvial rivers ($n=541$); here slope is
350 expressed as

$$352 \quad \log S = \alpha_0 + \alpha_1 \log D_{50} + \alpha_2 \log H,$$

351 Eq. 4

353 where the constants are given by $\alpha_0 = -2.08 \pm 0.036$, $\alpha_1 = 0.254 \pm 0.016$, and $\alpha_3 = -1.09 \pm 0.044$. Using 10^6
354 values of H , and 10^6 values of α_0 , α_1 , and α_3 (uniformly distributed random samples between the
355 bounds of the standard errors), 10^6 values of S were similarly recovered, and the 1st, 2nd, and 3rd
356 quartiles were extracted. Using Equation 3, estimates of S derived from Equation 4 can be
357 corroborated.

358 Along up-dip to down-dip transects, palaeoslope estimates can be used to infer the shape of the river
359 long profile, and therefore palaeorelief, in the alluvial domain. Palaeorelief was reconstructed using

360 median estimates of S from Equations 3 and 4. The local slope at downstream position x , S_x , can be
 361 related to its upstream contributing catchment area, A_x , (Hack, 1973; Flint, 1974; Whipple, 2004) as

$$363 \quad S_x = k_s A_x^{-\theta},$$

362 Eq. 5

364 where k_s is the steepness index and θ is the concavity, typically between 0.4 and 0.7 (Tucker &
 365 Whipple, 2002). Given that the palaeo-concavity is unknown, a range of plausible concavities (0.4, 0.5,
 366 and 0.6) were tested to gauge the spread of possible results. Following Hack's law, local catchment
 367 length, L_x , is related to A_x by $L_x = c_H A_x^h$, where c_H is the Hack coefficient, commonly taken as near 2 when
 368 L_x and A_x are in units of km^2 (Castelltort et al., 2009), and h is the Hack exponent, commonly taken as
 369 0.5 (Hack, 1957). Using Hack's law, local slope can instead be estimated as a function of downstream
 370 distance, where

$$372 \quad S_x = k_s L_x^{-\theta/h}.$$

371 Eq. 6

373 k_s is calculated from field data using downsystem palaeoslope estimates and knowledge of catchment
 374 lengths at each downstream location. As this study solely focuses on the alluvial domain, this means
 375 that up-dip fan apexes would have a catchment length of 0 km. Here, the most up-dip field sites are
 376 set as having a catchment length of 5 km to allow for additional up-dip fan length. Knowledge of
 377 distance to the coeval palaeoshoreline from our most down-dip sites (Price Canyon and Straight
 378 Canyon) is also required. Based on previous studies, approximate distances to the palaeoshoreline are
 379 set as ~10 km for the lower Blackhawk Formation, ~35 km for the middle Blackhawk Formation, ~50
 380 km for the upper Blackhawk Formation, ~110 km for the Castlegate Sandstone (Hampson et al., 2012;
 381 Hampson et al., 2013), and ~200 km for the Price River Formation (Hettinger & Kirschbaum, 2002;
 382 Aschoff & Steel, 2011a). A nonlinear least squares regression was used to find best fit palaeoslope
 383 profiles (Equation 6) for both the northern and southern transects at each time interval. Palaeoslope
 384 profiles were then transformed into river long profiles by summing elevation increments along the
 385 downstream length to the palaeoshoreline. This elevation decrease is indicative of the likely relief in
 386 the alluvial domain of these palaeorivers.

387 (C) Hydrodynamics

388 Flow velocities, U , were calculated following Manning's Equation, where

$$390 \quad U = \frac{1}{n} H^{\frac{2}{3}} S^{\frac{1}{2}}$$

389 Eq. 7

391 and n is Manning's constant, set as 0.03. In reconstructing hydrodynamics, palaeoslope estimates
 392 derived from the Shields stress inversion (Equation 3) were carried forward. Water discharges were
 393 then estimated by multiplying flow velocity by flow depth, to obtain discharge per unit width ($Q=UH$).

394 To determine dominant mode of sediment transport, the Rouse number, Z , was calculated as

396
395

$$Z = \frac{w_s}{\beta \kappa u_*}$$

Eq.8

397 where β is a constant that correlates eddy viscosity to eddy diffusivity, typically taken as 1, and κ is the
398 von Karman constant, taken as 0.4. Sediment settling velocity, w_s , was calculated as a function of grain
399 size following Ferguson and Church (2004),

401
400

$$w_s = \frac{RgD_{50}^2}{C_1\nu + (0.75C_2RgD_{50}^3)^{0.5}},$$

Eq. 9

402 where ν is the kinematic viscosity of water (1×10^{-6} m²/s for water at 20°C) and $C_1=18$ and $C_2=1$ are
403 constants associated with grain sphericity and roundness. With Z , dominant mode of sediment
404 transport is typically wash load for $Z < 0.8$, 100% suspended load for $0.8 < Z < 1.2$, 50% suspended load
405 (i.e. mixed load) for $1.2 < Z < 2.5$, and bedload for $Z > 2.5$. To corroborate inferred sediment transport
406 modes, the particle Reynolds number, Re_p , was additionally calculated in line with previous work (cf.
407 Parker, 2004) as

409
408

$$Re_p = \frac{\sqrt{RgD_{50}}D_{50}}{\nu}$$

Eq. 10

410 and plotted Re_p as a function of τ^* , following Dade and Friend (1998). This enables field results to be
411 contrasted with data that are typical of either suspended, mixed, or bedload sediments (Leopold &
412 Wolman, 1957; Schumm, 1968; Chitale, 1970; Church & Rood, 1983; Andrews, 1984), and to identify
413 where these data are positioned among characteristic flow regimes (no sediment transport; ripples
414 and dunes; upper plane beds) following Allen (1982a, 1982b).

415 (C) Fluvial style

416 Fluvial style (i.e. planform morphology) of Blackhawk–Castlegate rivers has been described
417 qualitatively from outcrop architecture (Miall, 1994; Miall & Arush, 2001; Adams & Bhattacharya,
418 2005; Hampson et al., 2013). Here, a quantitative approach is implemented to decipher fluvial style to
419 complement these works, check for consistency, and interpret the interplay between different
420 planform morphologies and the tectono-geographic setting. This is carried out for field areas along
421 the eastern Wasatch Plateau. First, Froude number, Fr , is calculated as

423
422

$$Fr = \frac{U}{\sqrt{gH}}$$

Eq. 11

424 and, then, depth/width ratios were plotted against palaeoslope/Froude ratios (G. Parker, 1976).
425 Various flow widths were assigned to determine what depth/width ratios are required such that the
426 data fall within the theoretical stability fields for single-thread and multi-thread fluvial planform
427 morphologies. These flow widths are then contrasted with estimates of apparent maximum flow width

428 from architectural analysis of channelized sandstone bodies (e.g. Flood & Hampson, 2015) and field
429 interpretations of fluvial style (Miall, 1994; Miall & Arush, 2001; Adams & Bhattacharya, 2005;
430 Hampson et al., 2013).

431 For all palaeohydrological parameters the median result is presented. In instances where results
432 additionally include the 1st and 3rd quartiles, these are the results when the 1st and 3rd quartiles of
433 palaeoflow depth (and therefore palaeoslope, Shields stress, etc.) were propagated through the
434 methodology.

435 **(A) Results**

436 **(B) Channel geometries**

437 Linear relationships between maximum cross-set height and both the mean and the P_{84} cross-set
438 height were established from measured cross-set distributions (n=470) for our field area (Fig. 5a,b).
439 Maximum and mean cross-set heights are very well-correlated ($R^2=0.88$) and 95% of observed mean
440 cross-set heights fall within ~3 cm of the predicted mean cross-set height. Using these new
441 relationships, mean cross-set heights were estimated for all (n=4053) measured maximum cross-set
442 heights (Fig. 5c–e; Supplementary Table S3).

443 Maximum cross-set heights typically span 0.1–0.35 m — these field data are comparable to the results
444 of previous work (e.g. Adams & Bhattacharya, 2005). From maximum cross-set heights, mean cross-
445 set heights spanning 0.07–0.25 m are estimated, which correspond with original bedform heights of
446 0.2–0.75 m. Flow depths for the along-depositional-strike transect suggest that, in both space and
447 time, these 5 transverse fluvial systems maintained median flow depths of 2–4 m, with 1st–3rd
448 interquartile ranges spanning 1–7 m (Fig. 6). Overall, flow depths do not change across the Blackhawk–
449 Castlegate transition but exhibit a marginal decrease during middle Castlegate Sandstone deposition
450 of <0.5 m. Flow depths are also projected to be overall <1 m greater in southern fluvial systems (Fig.
451 6). However, these observed differences all lie within the interquartile range of calculations,
452 suggesting these systems were similar to each other.

453 Reconstructed palaeoflow depths are consistent with independent palaeoflow depth proxies
454 (Supplementary Table S4), which demonstrates applicability of cross-set scaling relations in the
455 absence of well-preserved macroforms. Bar heights, where available, are consistent with projected
456 flow depths of 2–4 m across field sites. For instance, Chamberlin and Hajek (2019) reported mean bar
457 heights of 2.6 m, 3.6 m and 3.9 m for the entire Castlegate Sandstone at Price Canyon, Straight Canyon
458 and Salina Canyon, respectively. At Price Canyon, both Lynds and Hajek (2006) and Hajek and Heller
459 (2012) reported greater mean bar heights of 4.1 m specifically for the lower Castlegate Sandstone,
460 with a typical span of 1–8 m (Lynds & Hajek, 2006; McLaurin & Steel, 2007) — we note that the 1st–3rd
461 interquartile range of our reconstructed palaeoflow depths is typically 1–7 m and therefore agrees
462 with this range. Meanwhile, channelized fluvial sandstone bodies are more extensively documented
463 for the Blackhawk Formation and their heights offer a maximum limit on palaeoflow depths. Flood
464 and Hampson (2015) recovered mean apparent heights for channelized sandstone bodies of 6–8 m
465 across the entire Blackhawk Formation between Straight Canyon and Salina Canyon. As maximum
466 bounds on palaeoflow depth, these values are also in good agreement with the upper bounds (3rd
467 quartile) of estimated palaeoflow depths.

468 (B) Palaeoslopes and river long profiles

469 Palaeoslope estimates for our northern (Fig. 7a–f) and southern (Fig. 7g–m) transects and results from
470 each method (Equations 3 and 4) were compared (Fig. 7). Palaeoslopes are presented as y/x — a
471 palaeoslope of 0.001 results in an elevation decrease of 1 m per 1000 m and is equivalent to 0.057° .
472 Maximum (up-dip) palaeoslopes of 5×10^{-3} are equivalent to slopes of $\sim 0.3^\circ$; these magnitudes of
473 palaeoslope are comparable with the slopes of modern rivers, including the Savannah and North Loup
474 (USA) (Carlston, 1969; Crowley, 1983; Mohrig & Smith, 1996; Fotherby, 2009). Minimum (down-dip)
475 palaeoslopes of $\sim 5 \times 10^{-5}$ are equivalent to slopes of $\sim 0.003^\circ$; palaeoslopes in the range 10^{-5} to 10^{-4}
476 are characteristic of lowland/low-slope rivers, such as the Niobrara, Platte and Mississippi (USA)
477 (Carlston, 1969).

478 Up-dip, palaeoslopes are consistently of order 10^{-3} (Fig. 7), with the exception of the Blackhawk
479 Formation in the southern transect where 1st–3rd interquartile ranges extend down to palaeoslopes of
480 7×10^{-4} (Fig. 7k–m). Importantly, an order of magnitude decrease in palaeoslope is reconstructed
481 between a down-system distance of 10 and 25 km; this occurs in all stratigraphic intervals, at the same
482 downstream distance, for both the northern and southern transects (Fig. 7). Down-dip, from ~ 25 km
483 onwards, palaeoslopes are flatter and typically span 5×10^{-5} to 5×10^{-4} . In these lower gradient regions,
484 there is an apparent down-dip increase in palaeoslope in Fig. 7b,c,i–m. However, this apparent
485 increase is within the 1st–3rd interquartile range. Up-dip to down-dip palaeoslope estimates derived
486 from Equations 3 and 4 are broadly consistent with one another — they are the same order of
487 magnitude and the 1st–3rd interquartile ranges either overlap with, or are within a factor of 2–3 of,
488 one another. However, Equation 3 overpredicts and underpredicts palaeoslope relative to Equation 4,
489 such that palaeoslope estimates derived from Equation 3 imply higher topographic relief and
490 estimates derived from Equation 4 imply lower topographic relief (Fig. 7).

491 To constrain temporal changes in palaeoslope, the evolution of the the most up-dip locations of both
492 the northern and southern transects can be compared (Fig. 8). Palaeoslopes increase at the onset of
493 Castlegate Sandstone deposition (intervals 4–6) and the magnitude of this increase differs between
494 the north and the south (Fig. 8). In the north, the initial palaeoslope is higher ($\sim 2 \times 10^{-3}$) and increases
495 by a factor of 1.5 to $\sim 3 \times 10^{-3}$ (Fig. 8a), whereas, in the south, the initial palaeoslope is lower ($\sim 1 \times 10^{-3}$)
496 and increases by a factor of up to 4, to $\sim 4 \times 10^{-3}$ (Fig. 8b). This implies a coeval increase in palaeoslope
497 at the onset of Castlegate Sandstone deposition which was more pronounced in the south. Again,
498 estimates derived from Equation 4 dampen this increase relative to estimates derived from Equation
499 3.

500 With up-dip to down-dip palaeoslope estimates for both the northern and southern transects, best-
501 fit palaeoslope profiles were derived as a function of downstream distance (Equation 7;
502 Supplementary Table S6). Palaeoslope profiles generally fit reconstructed palaeoslopes well, with
503 typical R^2 values >0.85 , and it is noted that of 3 reference concavities, θ , used, the higher value of
504 $\theta=0.6$ typically recovered the best fits (Supplementary Table S6). A notable exception to this is
505 palaeoslope profiles reconstructed from Shields stress palaeoslope estimates for the Castlegate
506 Sandstone in the northern depositional-dip transect — the lower $\theta=0.4$ value generates the best fit
507 and this fit is relatively poor (R^2 of 0.35–0.6). However, palaeoslope profiles for these same space-
508 time intervals derived from alternative palaeoslope estimates (Equation 4) fit well ($R^2 >0.9$;
509 Supplementary Table S6).

510 In reconstructing palaeoslope profiles steepness index, k_s , values were recovered for each
511 stratigraphic interval (for $\theta=0.5$), which were mostly between ~ 5 and 35 m (Supplementary Table S6).
512 There is an increase in reconstructed k_s values across the Blackhawk–Castlegate transition for both
513 methods of palaeoslope estimation. For estimates derived from Equation 3, k_s values increase across
514 the Blackhawk–Castlegate transition by a factor of ~ 2 –3 in the northern transect, and by a factor of
515 ~ 4 –5 in the southern transect. In contrast, for estimates derived Equation 4, k_s values increase across
516 the Blackhawk–Castlegate transition by a factor of <1.5 in the northern transect, and by a factor of ~ 2
517 in the southern transect (Supplementary Table S6).

518 Palaeoslope profiles were transformed into river long profiles, which are indicative of the palaeorelief
519 in the alluvial domain, or depositional reaches, of Blackhawk–Castlegate–Price River fluvial systems
520 only (Fig. 9). Given that the concavities of these ancient rivers are not known, implementing plausible
521 concavities of 0.4, 0.5 and 0.6 enabled a likely spread of values for palaeorelief to be constrained (Fig.
522 9). Results indicate that different concavities recover similar values for palaeorelief; total estimates
523 vary within a factor of ~ 2 , between a concavity of 0.4 and 0.6 (Fig. 9).

524 Using palaeoslope estimates derived from Equation 3, palaeorelief during Blackhawk deposition was
525 estimated as ~ 40 –60 m in the northern transect (Fig. 9e,f) and 15–25 m in the southern transect (Fig.
526 9k–m). During Castlegate Sandstone deposition, palaeorelief increased by a factor of 1.5–2.5 in the
527 northern transect, to an estimated 65–145 m of palaeorelief, whereas it increased by a factor of 5–6
528 in the southern transect, to an estimated 90–130 m of palaeorelief. Alternatively, using palaeoslope
529 estimates derived from Equation 4, palaeorelief during Blackhawk Formation deposition was
530 estimated as ~ 30 –50 m in the northern transect (Fig. 9e,f) and 15–25 m in the southern transect (Fig.
531 9k–m). During Castlegate Sandstone deposition, palaeorelief increased by a factor of ~ 1.8 in the
532 northern transect, to an estimated 55–90 m of palaeorelief, whereas it increases by a factor of 2 in
533 the southern transect, to an estimated 30–50 m of palaeorelief. In detail, palaeorelief implied by
534 Equation 3 (Shields) is up to a factor of 2 greater than the palaeorelief implied by Equation 4
535 (Trampush). This higher palaeorelief during Castlegate Sandstone deposition is sustained into Price
536 River Formation times. It is stressed that these estimates refer to the alluvial domain only.

537 ***(B) Hydrodynamics and sediment transport***

538 Median flow velocities of 0.8 m/s, with an interquartile range of 0.4–1.6 m/s are deduced across all
539 field data (Fig. 10a), as well as median unit discharges of 2.5 m²/s with an interquartile range of 1–10
540 m²/s (Fig. 10b). Using plausible single-thread channel widths of 100–500 m at down-dip locations (see
541 Planform morphologies), this would imply median total discharges between 250–1250 m³/s, which is
542 comparable with total discharges of well-known North American rivers such as the Platte, Hudson,
543 Colorado, Arkansas and Susquehanna. However, if multi-thread rivers are assumed to possess >1
544 branch/braid, total discharges would have been several times greater. With a reconstructed increase
545 in palaeoslope at the Blackhawk–Castlegate transition, a coeval increase in flow velocities and unit
546 water discharges is expected analytically. Here, across all up-dip field areas, flow velocities are overall
547 greater during Castlegate Sandstone deposition, up to a factor of 2 to 3 (Fig. 10c), relative to Blackhawk
548 Formation deposition, whereas down-dip flow velocities are broadly the same through time (Fig. 10d).
549 Both up-dip and down-dip, unit water discharges overall do not change at the Blackhawk–Castlegate
550 transition (Fig. 10e,f). To offer a specific example for the Blackhawk–Castlegate transition (intervals 3

551 and 4), at Mellor Canyon, median flow velocity, U , increased from 1.9 to 3.0 m/s, and median unit
552 water discharge, Q , only increased marginally from 4.4 to 4.6 m²/s.

553 Reconstructed Rouse numbers, Z , indicate that dominant transport modes of bed-material varied in
554 space and time (Fig. 11). Up-dip field sites consistently exhibit high Z values for both the median and
555 1st–3rd interquartile range, indicating predominant bedload transport (Fig. 11). Median Z values then
556 decrease by a downstream distance of 30 km, indicating local transition to predominantly mixed load
557 systems, however the likely spread of values indicated by the interquartile range implies that
558 dominant transport modes at this downstream distance may have spanned both mixed load and a
559 near entirely suspended load (Fig. 11). A crucial exception to this observation is for Castlegate
560 Sandstone deposition in the southern transect (intervals 4–6) where, at a downstream distance of 30
561 km, median Z values suggest bedload remains the most important transport mode (Fig. 11g–i). At
562 downstream distances associated with the most down-dip field sites, median Z values have further
563 decreased, however 1st–3rd interquartile ranges mostly still span both the mixed load and entirely
564 suspended load domains.

565 The inferred dominant sediment transport modes are corroborated with results in Fig. 12, in which
566 Shields stress, τ^* , is plotted as a function of particle Reynolds number, Re_p , for each field site. These
567 data are plotted alongside observed data that are characteristic of suspended load, mixed load and
568 bedload regimes (Leopold & Wolman, 1957; Schumm, 1968; Chitale, 1970; Church & Rood, 1983;
569 Andrews, 1984). Up-dip field sites (Dry Canyon, Lake Fork, Mellor Canyon) plot among secondary data
570 that are typical for bedload rivers, meanwhile all other field sites plot in the mixed-load realm (Fig.
571 12). Of field sites dominated by a mixed load, data from Sixmile Canyon and Straight Canyon plot
572 closest to the bedload realm, which is consistent with observations in Fig. 11, whereresults suggest
573 that bedload transport remained important in the southern transect during Castlegate Sandstone
574 deposition (intervals 4–6). Overall, results in Fig. 12 suggest that, down-dip, field sites are firmly in the
575 mixed load range — it is unlikely that bed-material loads were predominantly suspended. In contrast,
576 the 1st–3rd interquartile ranges in Fig. 11 suggest that dominant sediment transport modes may have
577 spanned the mixed load/predominantly suspended domain. Down-dip, all field sites straddle the
578 bounds between the stability fields for ripples and dunes and upper-stage plane beds (Fig. 12), which
579 implies unidirectional flow and high sediment transport rates (both suspended transport and bedload
580 transport).

581 **(B) Planform morphologies**

582 Finally, these data provide insights into the implied planform morphology of these ancient fluvial
583 systems. However, to do this effectively estimates of palaeochannel widths are needed. Widths are
584 difficult to constrain with confidence from field observations, and estimates from empirical scaling
585 relations are tentative. Assuming single-thread channels, reconstructed median flow depths of 2–4 m
586 might suggest channel widths of order 30–110 m and, using the upper bound of the 1–7 m
587 interquartile range, widths up to ~300 m (following Bridge and Mackey (1993)). In contrast, if multi-
588 thread channel belts are assumed, then channel belt widths of order 90–200 m, and up to ~400 m,
589 might be expected (following Leopold and Maddock Jr (1953)).

590 For a range of possible widths, palaeoslope/Froude ratios were plotted against channel depth/width
591 ratios (cf. G. Parker, 1976; Ganti et al., 2019b) (Fig. 13). Results imply that, for Blackhawk–Castlegate–

592 Price River fluvial systems, single-thread planforms would be stable at channel widths <1 km; channel
593 and channel-belt widths >1 km would have been required to instigate formation of bars and support
594 transition to multi-thread systems, forming vast channel-belt complexes (Fig. 13a–d). However,
595 planform reconstructions are very dependent on grain-size, a factor which is often not evaluated
596 systematically. Bulk grain-sizes were used in initial calculations (Fig. 13a–d; see Methods). However,
597 when using gravel-fraction grain-sizes, which can be associated with tectonic or climatic perturbations
598 (e.g. increased palaeoslope or high-magnitude low-frequency discharge events), the results show that
599 multi-thread planforms were more likely (Fig. 13e–h). For gravel-fraction grain-sizes, results imply that
600 single-thread planforms were likely stable at channel widths <500 m, and that channel and channel-
601 belt widths >500 m would have supported transition to multi-thread systems (Fig. 13b).

602 Further, of Blackhawk–Castlegate–Price River fluvial systems, field results for the Castlegate
603 Sandstone plot closest to the single-thread–multi-thread transition, whereas field results for the Price
604 River Formation plot furthest from this transition (Fig. 13). This indicates higher propensity of
605 Castlegate fluvial systems to braiding, relative to Blackhawk and Price River systems.

606 (A) Discussion

607 (B) What did Campanian palaeorivers look like?

608 These analyses provide new insights that build on previous work characterising ancient rivers in the
609 Campanian of central Utah as a series of distinct parallel transverse systems draining the Sevier front
610 (Robinson & Slingerland, 1998; Bartschi et al., 2018; Chamberlin & Hajek, 2019; Pettit et al., 2019).
611 These rivers traversed a low-gradient landscape; alluvial relief was 10s of metres to c. 100 m, and the
612 length scale of the alluvial domain (i.e. the distance from fan apexes to the palaeoshoreline) varied
613 from as little as ~70 km during lower Blackhawk Formation deposition, up to and in excess of 250 km
614 during Price River Formation deposition (Hettinger & Kirschbaum, 2002; Aschoff & Steel, 2011a;
615 Hampson et al., 2012; Hampson et al., 2013). Relief was 10s of metres during Blackhawk deposition,
616 when the length scale of the alluvial domain was at its narrowest. At the onset of Castlegate Sandstone
617 deposition an increase in palaeoslope is documented, with palaeorelief increasing to c. 100 metres,
618 which persisted into Price River deposition (Figs 7–9). For comparative purposes, such values of
619 palaeoslope and palaeorelief are characteristic of the Mississippi river and downstream reaches of its
620 principal tributaries e.g. the Missouri, Tennessee, Arkansas and Red rivers (Carlston, 1969).

621 Results imply that palaeoriver morphologies were similar in space and time, with palaeoflow depths
622 of order 2–4 m (Fig. 6). Previous DZ results suggest that northerly field sites (Price Canyon and Wattis
623 Road) represent smaller transverse systems and that southerly field sites (Straight Canyon, Link
624 Canyon and Salina Canyon) represent larger systems that include a longitudinal drainage component
625 (Bartschi et al., 2018; Pettit et al., 2019). These results indicate that size disparities between these 5
626 systems were not statistically significant — reconstructed variations in palaeoflow depths are within
627 the interquartile range. However, palaeoflow depths appear to have been marginally greater in
628 southerly systems (Fig. 6). If true, this may be attributed to the possible longitudinal drainage
629 component (Bartschi et al., 2018; Pettit et al., 2019).

630 Comparisons with modern rivers suggest that these 5 parallel palaeorivers (being ~25 km apart) were
631 substantial systems. Reconstructed hydrodynamic properties, such as flow velocities and unit water
632 discharges, are consistent with the ranges of values of modern systems with similar outlet spacings

633 and similar distances to range fronts (Perry et al., 1996; Schulze et al., 2005; Milliman & Farnsworth,
634 2013; Global Runoff Data Centre). Notably, unit discharges are overall constant in time — there is no
635 apparent increase in unit discharge at the Blackhawk–Castlegate transition (coeval with palaeoslope
636 increase). This raises questions as to the nature of down-system width evolution and has implications
637 for total discharge — plausible single-thread river widths of 100–500 m at down-dip locations would
638 imply median total discharges of 250–1250 m³/s.

639 Bedload transport was dominant at gravel-dominated up-dip localities, as expected, and suspended-
640 and mixed-load systems prevailed further down-dip, with some localised variations (Figs 11, 12). For
641 example, results highlight the importance of bedload transport during Castlegate Sandstone
642 deposition in the southern transect (Figs 11, 12). With this information it is possible to map out how
643 river behaviour varied spatially within catchments, and this informs best practices when it comes to
644 reconstructing sediment discharges. This is especially important where interested in reconstructing
645 the entire sediment load of an ancient system. For instance, channel palaeohydrologic approaches are
646 often used to reconstruct sediment discharges in ancient source-to-sink systems (Holbrook & Wanas,
647 2014; Lin & Bhattacharya, 2017; Sharma et al., 2017), however these reconstruction tools solely
648 reconstruct the bedload fraction and the suspended fraction of the bed material load (van Rijn, 1984b;
649 Wright & Parker, 2004), i.e. the portion of the suspended load that interacts with the bed. As such,
650 these reconstruction tools are not appropriate, by themselves, for reconstructing the total sediment
651 load of a wash load-dominated system, for example. Knowledge of prevailing sediment transport
652 modes is important for evaluating whether different sediment discharge reconstruction methods are
653 consistent with one another, as studies that reconstruct sediment discharges often corroborate
654 results with an independent approach (Lin & Bhattacharya, 2017; Watkins et al., 2018; Zhang et al.,
655 2018; Brewer et al., 2020; Lyster et al., 2020).

656 Here, reconstructions of planform morphology, following G. Parker (1976), and assuming channel
657 widths <1 km, imply that single-thread rivers would have prevailed throughout Blackhawk–
658 Castlegate–Price River deposition. Localized or intermittent transitions to braided planforms may have
659 been associated with tectonic or climatic perturbations, such as increased palaeoslope or high-
660 magnitude, low-frequency discharge events (Fig. 13). In detail, these perturbations (which can be
661 associated with the gravel-fraction grain-size) can support braiding at narrower channel/channel-belt
662 widths of order 500 m. Of these fluvial systems, Castlegate systems had a higher propensity to
663 braiding. At this point, it is important to flag that traditional bipartite classification of fluvial systems
664 aims to define fluvial systems as either straight/meandering or braided/anabranching end members
665 (Leopold & Wolman, 1957). However, these are not mutually exclusive; both straight/meandering and
666 braided/anabranching planforms can co-exist at reach scales. These reconstructions can be
667 contextualised by field evidence; however, field observations point to a discrepancy and this topic is
668 returned to later.

669 To create a holistic view as to the nature of these ancient fluvial landscapes, various modern analogues
670 can be considered. In the Amazon basin, several of the most up-system tributaries axially drain the
671 central and eastern Andean cordillera. For example, the Huallaga river, Peru, is an axial river fed by
672 transverse systems draining the eastern Andean range front. These transverse rivers have regular
673 outlet spacings, channel-belt widths of order 100s of metres (up to 1 km), and combine both single-
674 and multi-thread planforms which vary at reach-scales. In the eastern Himalayas, transverse systems

675 draining the range front into the axial Brahmaputra (Assam Valley) provide another modern analogue
676 for the pattern and style of these ancient fluvial systems, despite the larger scale of this system.

677 **(B) What drove spatio-temporal changes in morphologic properties?**

678 A key result in this study is quantification of an increase in palaeoslope at the Blackhawk–Castlegate
679 transition by a factor of 1.5–4, as well as the associated increase in palaeorelief (Figs 7–9). Increased
680 palaeoslopes have implications for the morphologic and hydrodynamic properties of these
681 palaeorivers, including their flow velocities and unit discharges. In this study, the increase in
682 palaeoslope and palaeorelief implies that rivers were actively responding to changes in uplift rate in
683 the hinterland region.

684 At the Blackhawk–Castlegate transition, palaeorelief increased from 10s of metres to c. 100 m (Fig. 9).
685 An important point to remember is that these estimates are specific to the alluvial domain only.
686 Behind the Sevier front, existence of a high-elevation plateau known as “Nevadaplano” is inferred
687 (Allmendinger, 1992; DeCelles, 1994, 2004; DeCelles & Coogan, 2006), which has been likened to the
688 modern high-elevation plateau, Altiplano, of the central Andes. Palaeo-elevations in the Sevier
689 highlands and Nevadaplano are argued to be 3 to >4 km — these values have been deduced from a
690 combination of climate modelling studies (Sewall & Fricke, 2013; Foreman et al., 2015), kinematic
691 reconstructions (DeCelles, 1994, 2004; DeCelles & Coogan, 2006) and other data, including palaeoflora
692 (Chase et al., 1998). Here, alluvial palaeorelief of order 100 m is reconstructed. Given that the low-
693 lying alluvial domain of these palaeorivers has a length scale of order 70–250 km, and given proximity
694 to high-elevation Sevier highlands, the entire river long profile is inferred to have likely been highly
695 concave. This is supported in part by the fact that, in reconstructing palaeoslope profiles, the best fits
696 were recovered when using a higher reference concavity of 0.6 (Supplementary Table S6). If best-fit
697 palaeoslope profiles were projected up-dip into the Sevier hinterland, palaeoslopes of 10^{-1} might be
698 reached within as little as 10 km of the most up-dip field area, and therefore elevations in excess of 1
699 km might be reached within a further 10 km. To again offer the modern Andes as an analogue, if one
700 were to plot an elevation profile from Peruvian shorelines, through the alluvial domain, and into the
701 western Andean cordillera and Altiplano, one would traverse an alluvial domain of order 50–150 km,
702 with 500 m to 1 km of relief, before crossing into the >3 km elevations of the western cordillera and
703 Altiplano. With a similar tectono-geographic setting in Late Cretaceous Utah, this comparison can also
704 be used to highlight the potential high concavity of these ancient river profiles.

705 In reconstructing palaeorelief, steepness indexes, k_s , were also recovered for northern and southern
706 transects (Equations 5 and 6) (Supplementary Table S6). While k_s was solved for using field data and a
707 nonlinear least squares regression, k_s values are often estimated (albeit tenuously) as a function of
708 known uplift rate and erodibility in bedrock channels, but additionally (although less frequently) in
709 downstream alluvial reaches (Kirby & Whipple, 2012; Pederson & Tressler, 2012; Stucky de Quay et
710 al., 2019). Inversely, where k_s can be measured, and where erodibility is known, first-order estimates
711 of uplift rate can be made. Steepness indexes recovered in this study were typically ~5–35 m (for a
712 reference concavity, θ , of 0.5) and, despite unknown erodibility, global data compilations indicate that
713 low uplift rates of order 0.01–0.1 mm/yr are generally associated with these kinds of values (Kirby &
714 Whipple, 2012). Despite overall low k_s values, it is important to note the relative increase in k_s by a
715 factor of <1.5 to 5 at the Blackhawk–Castlegate transition. While these are first-order estimates, and
716 are derived solely for the alluvial domain, an increase in k_s (and palaeorelief) can be attributed to a

717 relative increase in uplift rate in the hinterland region. Here, this increase might be attributed to
718 frontal thrust migration, or thrust initiation in the Sevier highlands (DeCelles, 2004; DeCelles &
719 Coogan, 2006). This includes Sevier shortening in the Charleston–Nebo Salient (CNS), an eastward
720 convex portion of the Sevier thrust front in north-central Utah (Fig. 1b) (Bruhn et al., 1986; Bryant &
721 Nichols, 1988; Constenius et al., 2003; Bartschi et al., 2018), which is commonly attributed to the influx
722 of quartzite-dominated coarse-grained detritus associated with Castlegate Sandstone progradation
723 (Robinson & Slingerland, 1998; Horton et al., 2004). For Castlegate Sandstone deposition in the
724 northern transect, results show that palaeoslope profiles did not fit reconstructed palaeoslopes well
725 and favoured lower concavities (which also did not fit well). Our interpretation is that shortening in
726 the CNS, which has been structurally linked with coeval basement Laramide uplifts in northern Utah
727 (Bruhn et al., 1986; Bryant & Nichols, 1988; Constenius et al., 2003; Bartschi et al., 2018), may have
728 significantly influenced river long profiles associated with northerly Castlegate fluvial systems near
729 Price, and locally lowered their concavities. Whereas ~60 km south in the southern transect, higher
730 concavity values of 0.6 deliver best fitting palaeoslope profiles through all 7 stratigraphic intervals
731 (Supplementary Table S6).

732 While tectonic drivers are commonly attributed to variations in channel steepness (Kirby & Whipple,
733 2001; Kirby et al., 2003; Wobus et al., 2006; Boulton & Whittaker, 2009; DiBiase et al., 2010), climatic
734 drivers, especially precipitation rates, also play a crucial role but are notoriously difficult to disentangle
735 from their tectonic counterpart (Wobus et al., 2010; DiBiase & Whipple, 2011; Champagnac et al.,
736 2012; Whittaker, 2012; D'Arcy & Whittaker, 2014). The role of climate is important to consider here,
737 given the assumed monsoonal climate and, therefore, highly seasonal discharge variability (Roberts,
738 2007; Roberts et al., 2008; Fricke et al., 2010; Sewall & Fricke, 2013). Previous work shows that
739 precipitation rates have a discernible role on steepness indexes (Champagnac et al., 2012; D'Arcy &
740 Whittaker, 2014); analytically, an increase in channel steepness and palaeoslope can be attributed to
741 a decrease in precipitation rate (to maintain similar total water discharge) (D'Arcy & Whittaker, 2014).
742 To reduce palaeoslopes by a factor of 2 precipitation rate must typically be quadrupled (D'Arcy &
743 Whittaker, 2014). Despite the supposed warm and wet climate (L. R. Parker, 1976; Kauffman &
744 Caldwell, 1993; Roberts & Kirschbaum, 1995), few workers have argued for, or investigated, the
745 possibility of increased aridity at the Blackhawk–Castlegate transition (van Wagoner, 1995; Adams &
746 Bhattacharya, 2005). In theory, increased palaeoslopes can be explained by decreased precipitation
747 (D'Arcy & Whittaker, 2014), however, here, no decrease in either flow velocities or unit discharges is
748 reconstructed at the Blackhawk–Castlegate transition (Fig. 10). Generally, in down-dip locations, flow
749 velocities and unit discharges are constant across this interval (Fig. 10d,f). At up-dip field sites,
750 however, flow velocities are overall slightly greater during Castlegate Sandstone deposition relative
751 to Blackhawk Formation deposition, but unit discharges remain similar for both.

752 With unit discharges constant in space and time, the crucial unknown is palaeochannel width. At
753 minimum, channel widths can be considered as broadly the same across the Blackhawk–Castlegate
754 transition. During Blackhawk Formation deposition, channelized sandbody widths of order 350–420
755 m offer a maximum limit on palaeochannel widths (Hampson et al., 2013; Flood & Hampson, 2015).
756 Meanwhile, during Castlegate Sandstone deposition, bar package widths are between ~60–180 m
757 (Chamberlin & Hajek, 2019); assuming 2–3 threads, these bar widths might imply channel belt widths
758 of order half a kilometre. However, planform stability estimates based on G. Parker (1976) indicate
759 that these rivers could have possessed anywhere between 1–10 threads (Fig. 13), which could result

760 in channel-belt widths up to and in excess of 1 km. At maximum, this implies increased channel widths
761 at the Blackhawk–Castlegate transition. Unless a significant decline in river widths is projected, then
762 field results do not directly support a climatic driver. Consequently, our interpretation is that increased
763 channel steepness and palaeoslope at the Blackhawk–Castlegate transition is due to tectonically
764 driven uplift in hinterland regions.

765 **(B) Effectiveness of palaeohydrological and palaeomorphological reconstructions**

766 While quantitative reconstructions have led to significant advances in both the quantity and level of
767 detailed information that can be extracted from fluvial strata (e.g. Ganti et al., 2019a), it is unclear
768 how accurately these tools characterise ancient systems. Addressing this question is particularly
769 important as sedimentology becomes increasingly numerical and it becomes easier to apply
770 quantitative tools to stratigraphy (Duller et al., 2010; Whittaker et al., 2011; Holbrook & Wanas, 2014;
771 Ganti et al., 2019b). With extensive existing work on Late Cretaceous fluvial systems of central Utah,
772 results in this study offer a unique opportunity to highlight consistencies and discrepancies between
773 quantitative interpretations of fluvial palaeohydrology and more qualitative field-based facies and
774 architectural interpretations.

775 To first-order, whether or not point reconstructions of various morphologic and hydrodynamic
776 parameters agree with qualitative interpretations can be evaluated using independent proxies
777 (derived from field measurements or facies interpretations). As previously mentioned, reconstructed
778 flow depths agree with several secondary observations of bar heights (Adams & Bhattacharya, 2005;
779 Lynds & Hajek, 2006; McLaurin & Steel, 2007; Hajek & Heller, 2012; Chamberlin & Hajek, 2019)
780 (Supplementary Table S4), which can be used as a direct proxy for flow depth (Bridge & Tye, 2000;
781 Hajek & Heller, 2012). This agreement indicates that cross-set heights can be used to reconstruct
782 reasonable flow-depth constraints and are useful as a bedform-scale approach. Such an approach is
783 particularly useful in core data, locations with limited outcrop exposure, or deposits where the degree
784 of bar preservation is poor. It is noted that scaling relations that relate cross-set heights with original
785 bedform heights (and subsequently formative flow depths) are derived from theory and experiments
786 that assume statistical steady state, in which flow is constant (Paola & Borgman, 1991; Leclair, 2002;
787 Jerolmack & Mohrig, 2005). As such, agreement of flow depth reconstructions with bar heights might
788 therefore imply that these dunes were formed in steady flow conditions (Ganti et al., 2020). This
789 contrasts with literature that alludes to the preferential preservation of dunes in unsteady flow
790 conditions (Reesink & Bridge, 2007; Reesink & Bridge, 2009; Reesink et al., 2015; Leary & Ganti, 2020),
791 and merits further work regarding the kinematic controls on dune preservation in this region.

792 For more complex palaeohydrologic reconstructions, such as palaeoslopes and palaeorelief (Figs 7–9),
793 it is not possible to directly corroborate estimates with independent proxies derived from field data.
794 Nevertheless, it is still possible to evaluate reconstruction tools by contrasting commonly used
795 methods. In this study the first approach used a theoretically-based Shields stress inversion (Equation
796 3), whereas the second approach used the empirically-derived model (Equation 4) of Trampus et al.
797 (2014). Palaeoslope estimates derived from each approach are in broad agreement with one another.
798 Each method typically recovers estimates of the same order of magnitude — in many cases the
799 interquartile ranges of estimates overlap and in all cases the extent of the extremes overlap (i.e. the
800 whiskers). These point comparisons between the 2 methods are promising, and in line with
801 comparisons made elsewhere (e.g. Ganti et al., 2019a). However, there are implications when larger

802 spatial scales are concerned, imparting uncertainty that must be carried forward in interpretation of
803 palaeorelief in the depositional reaches of these systems. Along the northern and southern transects,
804 Shields stress inversion estimates consistently show higher differences in palaeoslope (i.e. higher
805 slopes up-dip and lower slopes down-dip) relative to palaeoslopes derived from the Trampush et al.
806 (2014). This difference is likely an outcome of the Trampush et al. (2014) method using a continuous
807 function to estimate slope, whereas the Shields stress inversion relies on a step-change empirical
808 estimate for gravel or sand-bed rivers. Regardless of the method used, palaeoslope reconstructions
809 are dependent on grain-size and flow-depth estimates. Because flow depths did not appreciably
810 change in Blackhawk and Castlegate palaeorivers, variations in reconstructed slopes and derivative
811 estimates (e.g. water and sediment discharge) are largely driven by observed differences in grain-size.

812 Despite the differences of the 2 methodologies on palaeorelief, estimates of palaeorelief can be
813 compared with relief in modern systems possessing similar tectono-geographic set-ups. Palaeorelief
814 estimates between 50 and 100 m in depositional reaches of these ancient fluvial systems are
815 reasonable when compared with relief in modern systems with a similar tectono-geographic setting.
816 For example, one can return to the Andean analogue, but cross over to the eastern Andean cordillera
817 and into the foreland basin and low-lying plains of the Amazon river. For most of its course, the
818 Amazon long profile has a relief of less than 100 m (Milliman & Farnsworth, 2013) — relief only
819 exceeds 100 m in proximity to the range front (Milliman & Farnsworth, 2013).

820 Finally, these results complement field evaluation of the nature of Blackhawk Formation and
821 Castlegate Sandstone planforms, but also raise new questions. Channelized sandstone bodies of the
822 Blackhawk Formation are typically 350–420 m wide (Adams & Bhattacharya, 2005; Hampson et al.,
823 2013; Flood & Hampson, 2015), although a small proportion are much larger and some exceed 1 km
824 (Flood & Hampson, 2015). These sandstone bodies offer a maximum cap on palaeoflow width. The
825 Blackhawk Formation is considered to mostly represent single-thread systems, which results in this
826 study agree with. However there is significant field evidence that many channelized sandstone bodies
827 of the Blackhawk Formation represent multi-thread systems with mid-channel bars, based on bar
828 facies observations (Adams & Bhattacharya, 2005; Hampson et al., 2013; Flood & Hampson, 2015).
829 Field observations of multi-thread Blackhawk fluvial systems of order 100s of metres are inconsistent
830 with our results, which suggest multi-thread systems would not have been stable (Fig. 13). Meanwhile,
831 the Castlegate Sandstone is interpreted to be fully-braided from facies observations (Miall, 1993,
832 1994; Miall & Arush, 2001; McLaurin & Steel, 2007). Reported mean bar package widths of order 60–
833 180 m for the Castlegate Sandstone (Chamberlin & Hajek, 2019) would imply total channel widths <1
834 km (assuming a few braids); our reconstructed planform stability estimates, which indicate that
835 Castlegate systems should have been single-threaded, are again inconsistent with sedimentological
836 facies and architectural interpretations. Other quantitative reconstructions of planform have
837 contradicted traditional field-based facies observations (Ganti et al., 2019a), and these inconsistencies
838 must be treated carefully. The main limitation to reconstructing ancient channel planforms is a lack of
839 reliable methods for estimating palaeochannel widths. Interpreting palaeochannel planforms from
840 facies associations and stratigraphic-architectural data is not trivial, particularly where outcrop is
841 limited or where observations are equivocal. But, in this case, a number of workers have concluded
842 that braided conditions prevailed at the time of Castlegate Sandstone deposition (Lawton, 1986b;
843 Miall, 1994; van Wagoner, 1995; Miall & Arush, 2001) and occurred at times during Blackhawk
844 Formation deposition (Adams & Bhattacharya, 2005; Hampson et al., 2013; Flood & Hampson, 2014,

845 2015). As such, it can be argued that further detailed work to test and reconcile facies-based and
846 hydraulically derived interpretations of channel planforms is a pressing research goal.

847 **(A) Conclusions**

848 Here a four-dimensional reconstruction of palaeohydrology in Late Cretaceous palaeorivers of central
849 Utah, USA, is presented, using field data and a well-established quantitative framework. Overall, fluvial
850 morphologies were similar in space and time, although marginally greater reconstructions of flow
851 depths in southerly systems likely reflect the contribution of a longitudinal drainage component. The
852 most prominent spatio-temporal change is an increase in palaeoslope at the Blackhawk–Castlegate
853 transition by a factor of 1.5–4; this reflects an increase in palaeorelief (for the alluvial domain) from
854 10s of metres during Blackhawk Formation deposition up to, and in excess of, 100 m during Castlegate
855 Sandstone deposition, which persisted into Price River Formation times. The observation that unit
856 water discharges do not change at the Blackhawk–Castlegate transition does not support a climatically
857 driven increase in palaeoslope and channel steepness. Results therefore point to a tectonically driven
858 palaeoslope increase. In deciphering the relative role of tectonic and climatic drivers, the main
859 limitation in this study is uncertainty in palaeochannel widths, which directly affect total water
860 discharges. Palaeochannel width reconstructions therefore remain a prominent research challenge.

861 Results complement and expand on extensive facies-based interpretations of these systems, which
862 offers unique opportunity to evaluate the efficacy of quantitative palaeohydrological reconstruction
863 tools. Bedform-scale palaeoflow depth reconstructions are in good agreement with observations of
864 preserved barforms. Moreover, while different palaeoslope reconstruction methods produce results
865 that broadly agree, the results show that at larger spatial scales they over- and under-predict relief
866 relative to one another, which has implications for quantifying alluvial palaeorelief and, therefore, the
867 magnitude of change in relief at the Blackhawk–Castlegate transition. Finally, quantitative hydraulic
868 reconstructions of planform somewhat disagree with facies-based interpretations. While this
869 discrepancy ties back to uncertainty in palaeochannel widths, these results highlight that further work
870 is required to reconcile hydraulically- and facies-based approaches in order to facilitate their
871 application in the geological past.

872 **Acknowledgements**

873 This research was primarily funded by the Natural Environment Research Council (NERC) Science and
874 Solutions for a Changing Planet Doctoral Training Partnership (DTP), with additional funding by The
875 Geological Society of London and The British Sedimentological Research Group. We thank Christopher
876 Dean for support with planning fieldwork, George Hedley for support with field data collection, and
877 Stephen Watkins for useful discussions.

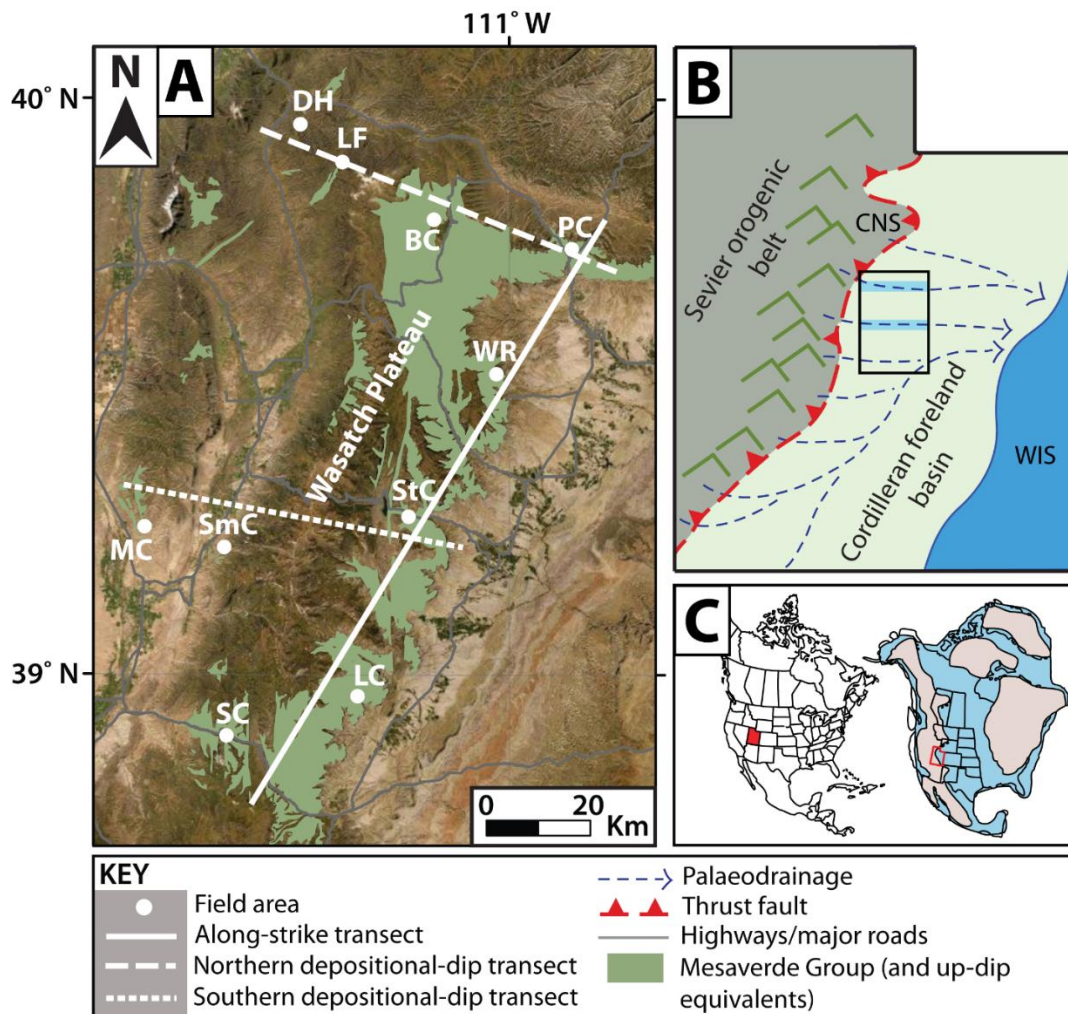
878 **Author Contributions**

879 SJL and ACW designed the study. SJL, ACW and BAL conducted field data collection. SJL processed field
880 data and results. SJL, ACW, GJH and EAH analysed and interpreted results. SJL wrote the manuscript.
881 ACW, GJH, EAH and PAA all contributed significantly to the manuscript.

882 **Data Availability**

883 Field data available in article supplementary material.

884



886

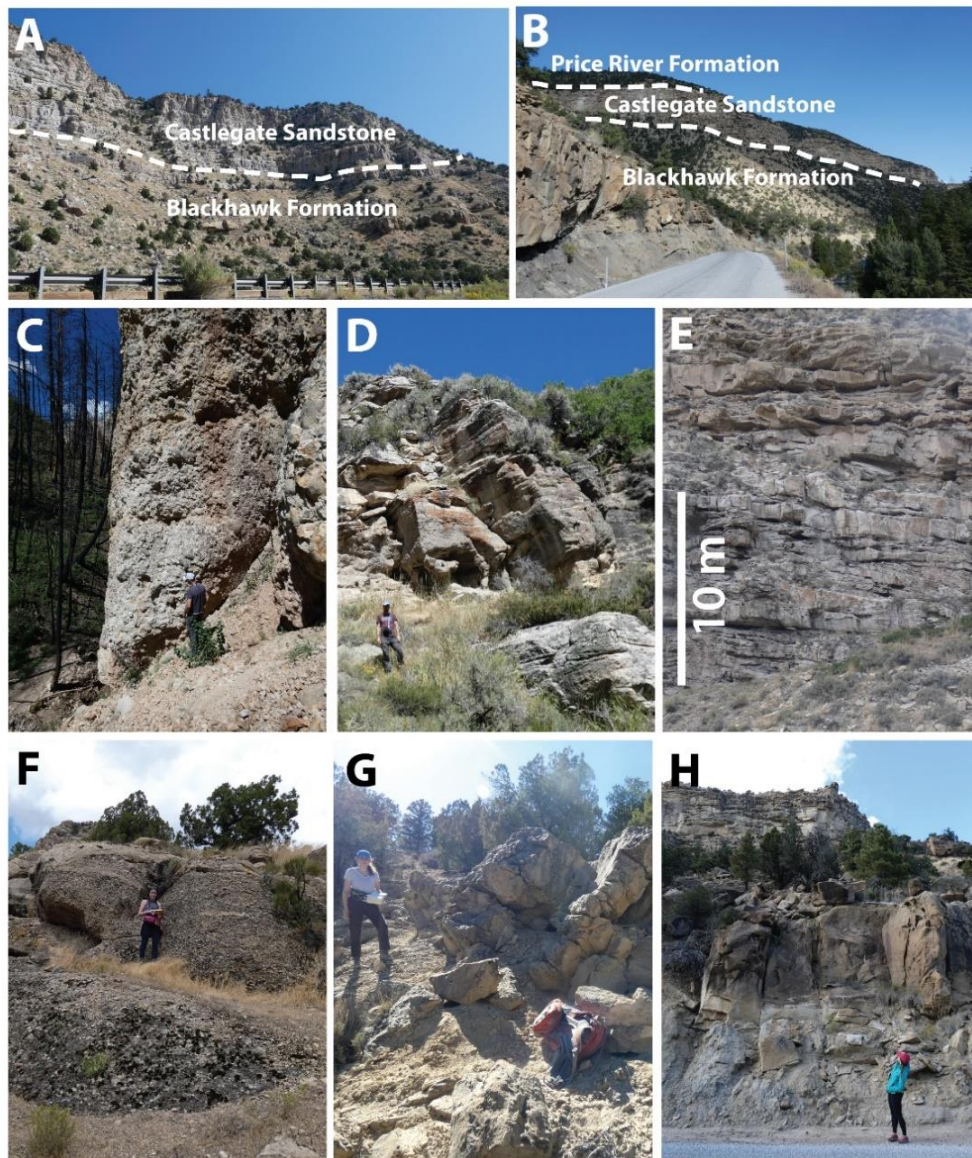
887 **Figure 1:** Study area. Part A) Field areas in central Utah, USA, which include Bear Canyon (BC), Dry
 888 Hollow (DH), Lake Fork (LF), Link Canyon (LC), Mellor Canyon (MC), Price Canyon (PC), Salina Canyon
 889 (SC), Sixmile Canyon (SmC), Straight Canyon (StC) and Wattis Road (WR). The solid white line indicates
 890 the along-depositional-strike transect defined in this study, the dashed white line indicates the
 891 northern depositional-dip transect defined in this study, and the dotted white line indicates the
 892 southern depositional-dip transect defined in this study. Part B) A conceptual diagram of Utah
 893 palaeogeography and palaeodrainage in the Campanian (Late Cretaceous). Likely configurations of
 894 drainage toward the Western Interior Seaway (WIS) are indicated by dashed blue lines. CNS =
 895 Charleston–Nebo Salient. The black outlined box indicates the study area (i.e. part A), and the two
 896 highlighted drainage routes (shaded blue) represent the northern and southern depositional-dip
 897 transects defined in this study (see part A). Part C) The location of Utah relative to the modern North
 898 American continent (left) and the Late Cretaceous North American continent (right), which features
 899 the Western Interior Seaway (blue). Utah is highlighted as a red box.

900

Stage		Stratigraphic unit		Interval
		W. Wasatch	E. Wasatch	
Campanian	Upper	Price River Conglomerate	Price River Formation	7
			Upper Castlegate Sandstone	6
			Middle Castlegate Sandstone	5
	Middle		Lower Castlegate Sandstone	4
			Indianola Group	Blackhawk Formation
	2			
	1			
Lower	Star Point Sandstone			

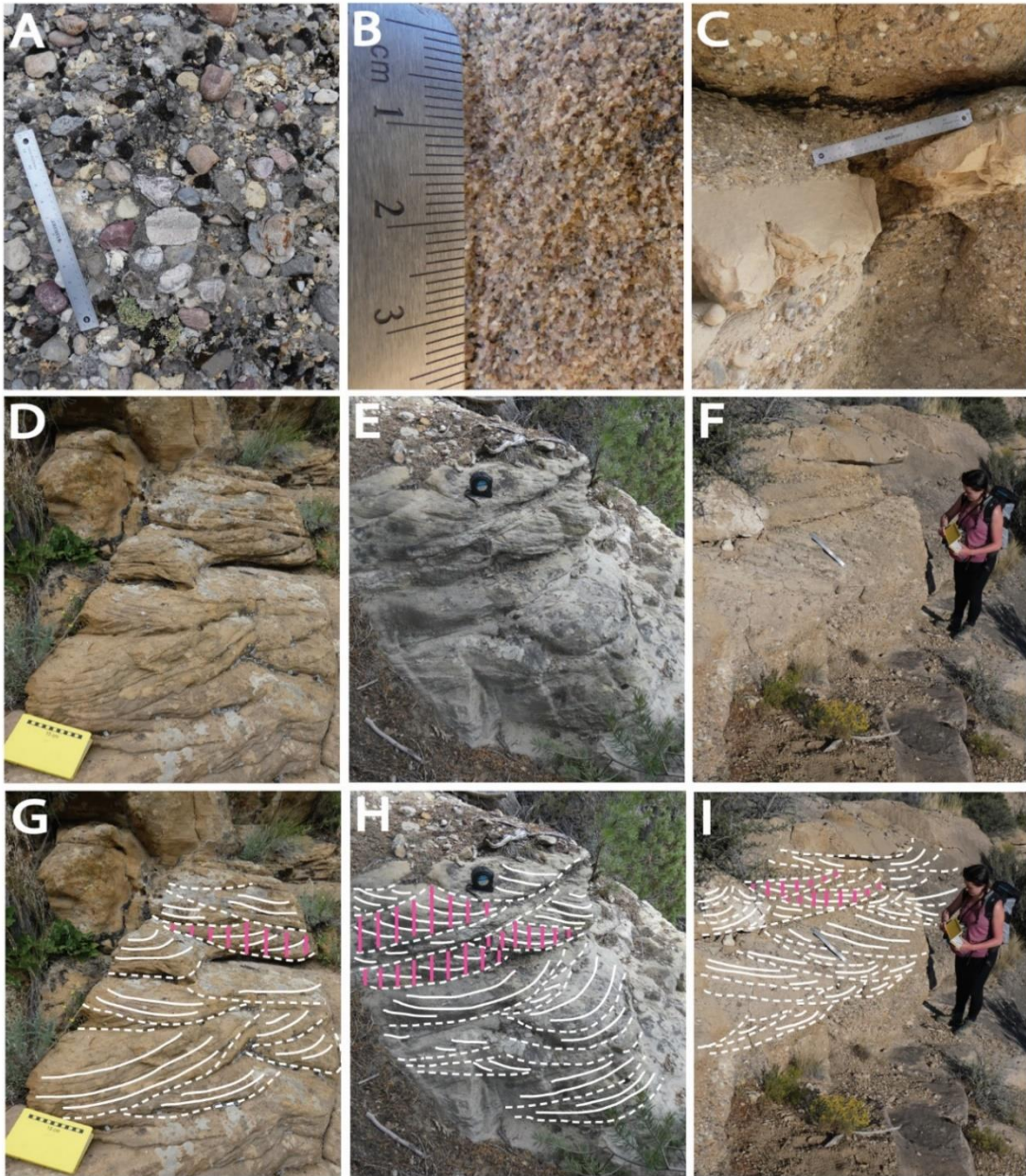
901

902 **Figure 2:** Regional stratigraphy and up-dip (western Wasatch Plateau) to down-dip (eastern Wasatch
903 Plateau) stratigraphic correlation followed in this study. Shaded intervals indicate the stratigraphic
904 intervals used in this study (note that they are not of equal duration). 1 = lower Blackhawk Formation;
905 2 = middle Blackhawk Formation; 3 = upper Blackhawk Formation; 4 = lower Castlegate Sandstone; 5
906 = middle Castlegate Sandstone; 6 = upper Castlegate Sandstone (Bluecastle Tongue); 7 = (lowermost)
907 Price River Formation. Dashed lines indicate an approximate interval boundary. Modified and
908 compiled using data from Fouch et al. (1983); Robinson and Slingerland (1998); Miall and Arush (2001);
909 Horton et al. (2004); Cobban et al. (2006); Aschoff and Steel (2011a, 2011b); Bartschi et al. (2018).
910 Price River Conglomerate nomenclature follows Aschoff and Steel (2011a, 2011b).



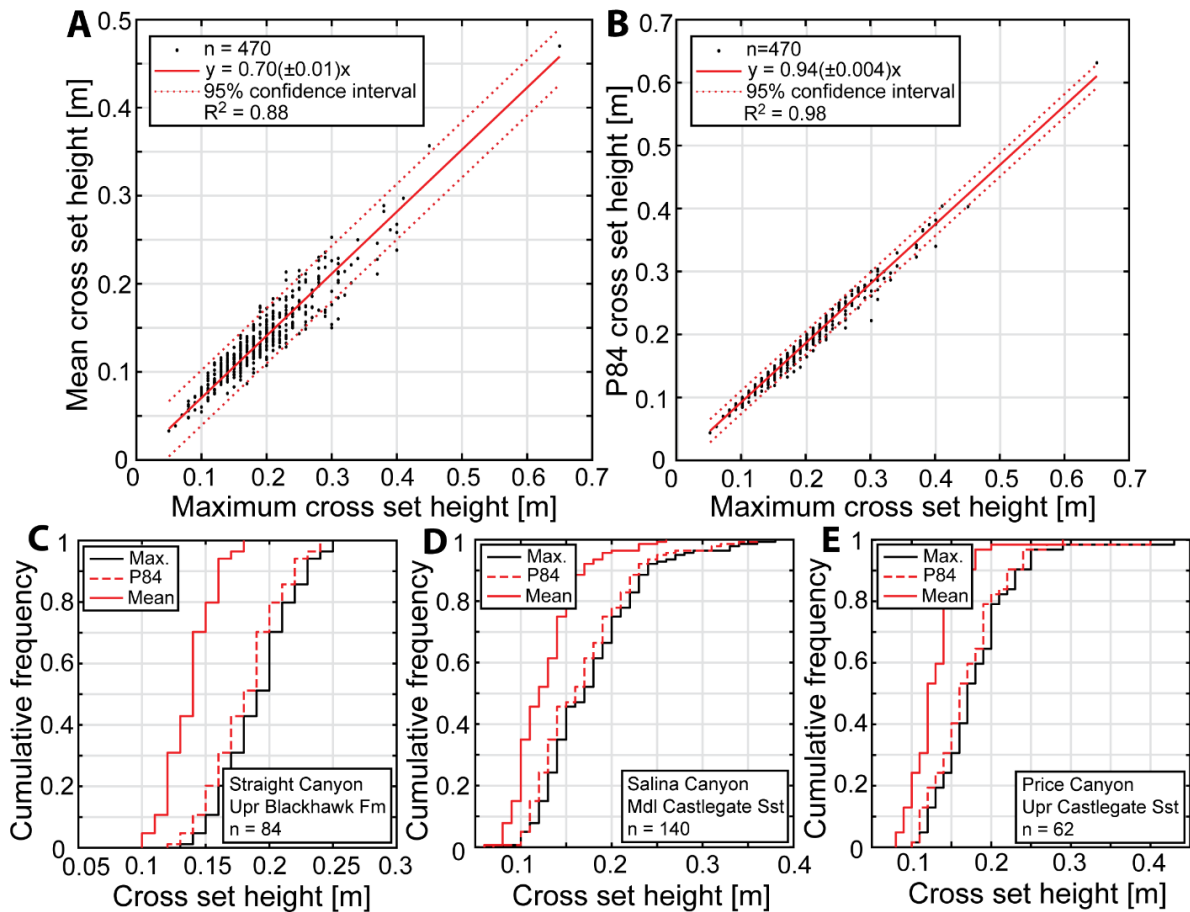
911

912 **Figure 3:** An overview of fluvial strata from which palaeohydrological field data were collected. Data
 913 were collected for 5 parallel palaeorivers in Late Cretaceous central Utah, USA. These 5 palaeorivers
 914 cropped out in canyons on the eastern front of the Wasatch Plateau — parts A and B show typical
 915 exposure of the Blackhawk Formation, Castlegate Sandstone, and Price River Formation in these
 916 canyons. Specifically, part A shows strata in Salina Canyon and part B shows strata in Straight Canyon
 917 (see Fig. 1), and dashed white lines indicate lithostratigraphic boundaries. For two of these 5
 918 palaeorivers, data were additionally collected upstream to downstream along defined depositional-
 919 dip transects (see Fig. 1). Parts C–E show deposits on the northern depositional-dip transect. From up-
 920 dip to down-dip, part C shows debris flow facies of the Price River Conglomerate, part D shows
 921 amalgamated fluvial gravels and sands of the Castlegate Sandstone near Bear Canyon, and part E
 922 shows amalgamated fluvial sands of the Castlegate Sandstone in Price Canyon. Parts F–H show
 923 deposits on the southern depositional-dip transect, for older sediments. From up-dip to down-dip,
 924 part F shows channelized fluvial gravel–sand bodies of the upper Sixmile Canyon Formation in Mellor
 925 Canyon, part G shows a small channelized sandstone body of the upper Sixmile Canyon Formation in
 926 Sixmile Canyon, and part H shows a large channelized sand body of the Blackhawk Formation in
 927 Straight Canyon (in the background the Castlegate Sandstone is visible).



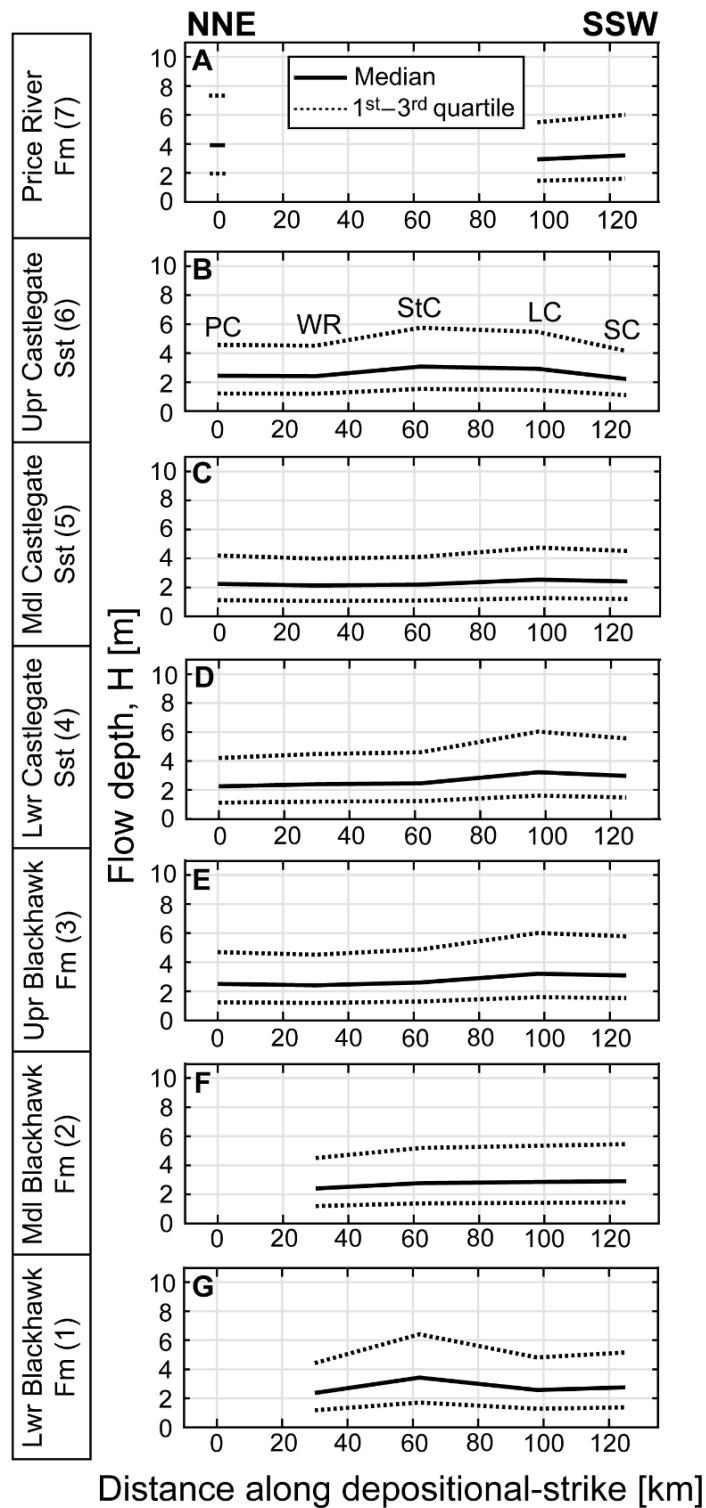
928

929 **Figure 4:** Field data collection included grain-size measurements for (part A) gravel and (part B) sand
 930 fractions, as well as (part C) estimates of the proportions of different grain-size facies. Parts D–F depict
 931 cross-bedding, and parts G–I depict interpreted versions of the same images. Dashed white lines
 932 indicate bounding surfaces of individual cross-sets and solid white lines indicate selected foresets
 933 within individual cross-sets. To exemplify sampling procedure when determining mean cross-set
 934 height, solid pink lines demonstrate how heights are measured for selected cross-set dip sections.
 935 Field notebook with 15 cm scale, tape measure, and 30 cm rule for scale.



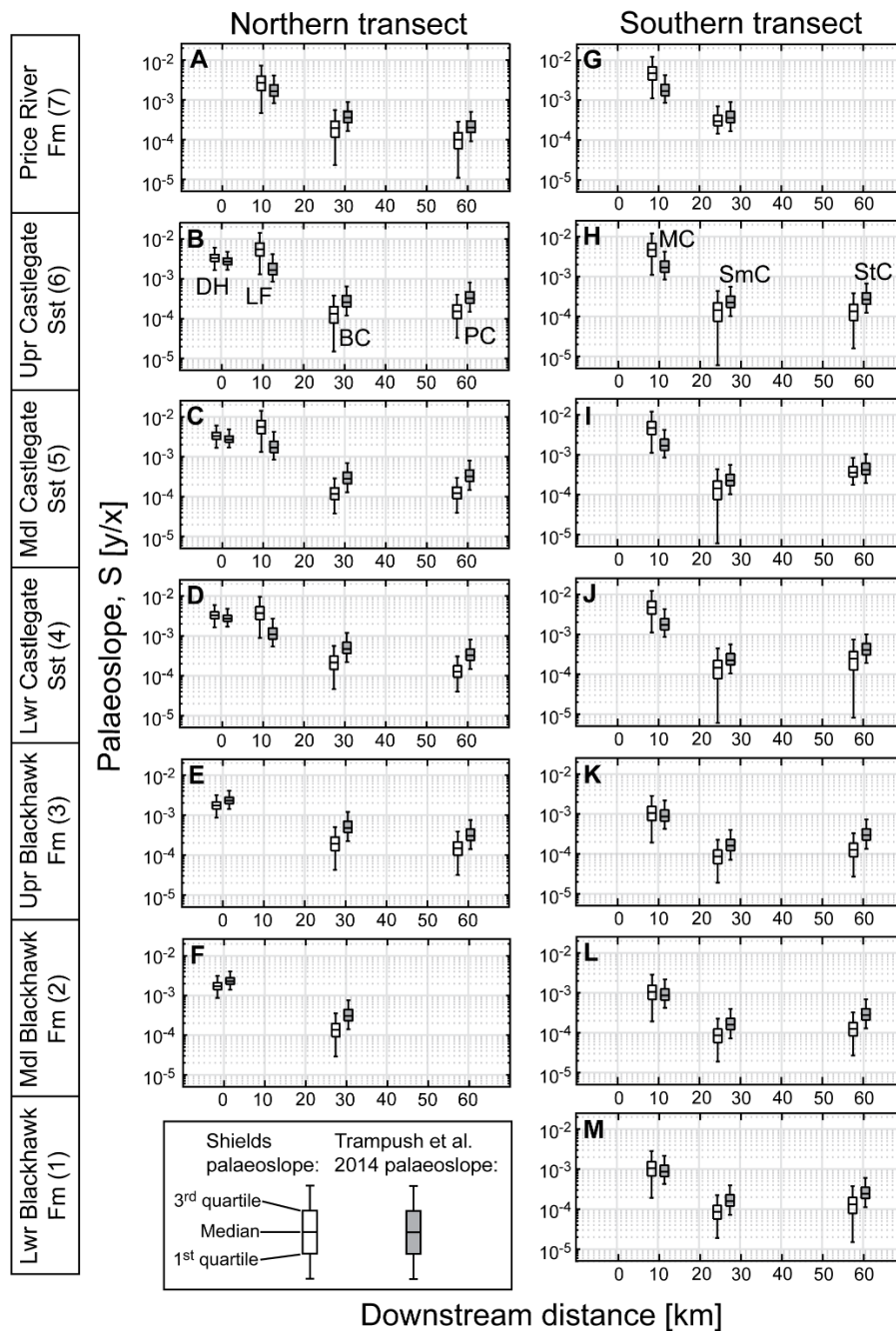
936

937 **Figure 5:** Part A) Relationship between maximum cross-set height and mean cross-set height. Part B)
 938 Relationship between maximum cross-set height and the 84th percentile (P_{84}) of cross-set height. Data
 939 are based on 470 measured cross-set distributions. Errors reported in the fits are 95% confidence
 940 intervals. Parts C–E) Examples of the use of these new relations (parts A and B) to predict the mean
 941 and P_{84} cross-set height from maximum cross-set heights. Examples are for the upper Blackhawk
 942 Formation in Straight Canyon (part C), the middle Castlegate Sandstone in Salina Canyon (part D), and
 943 the upper Castlegate Sandstone in Price Canyon (part E). In parts C–E, n indicates the number of
 944 maximum cross-set heights used to predict mean and P_{84} cross-set heights. Full cross set data for each
 945 field site, through each stratigraphic interval, are located in Supplementary Table S3.



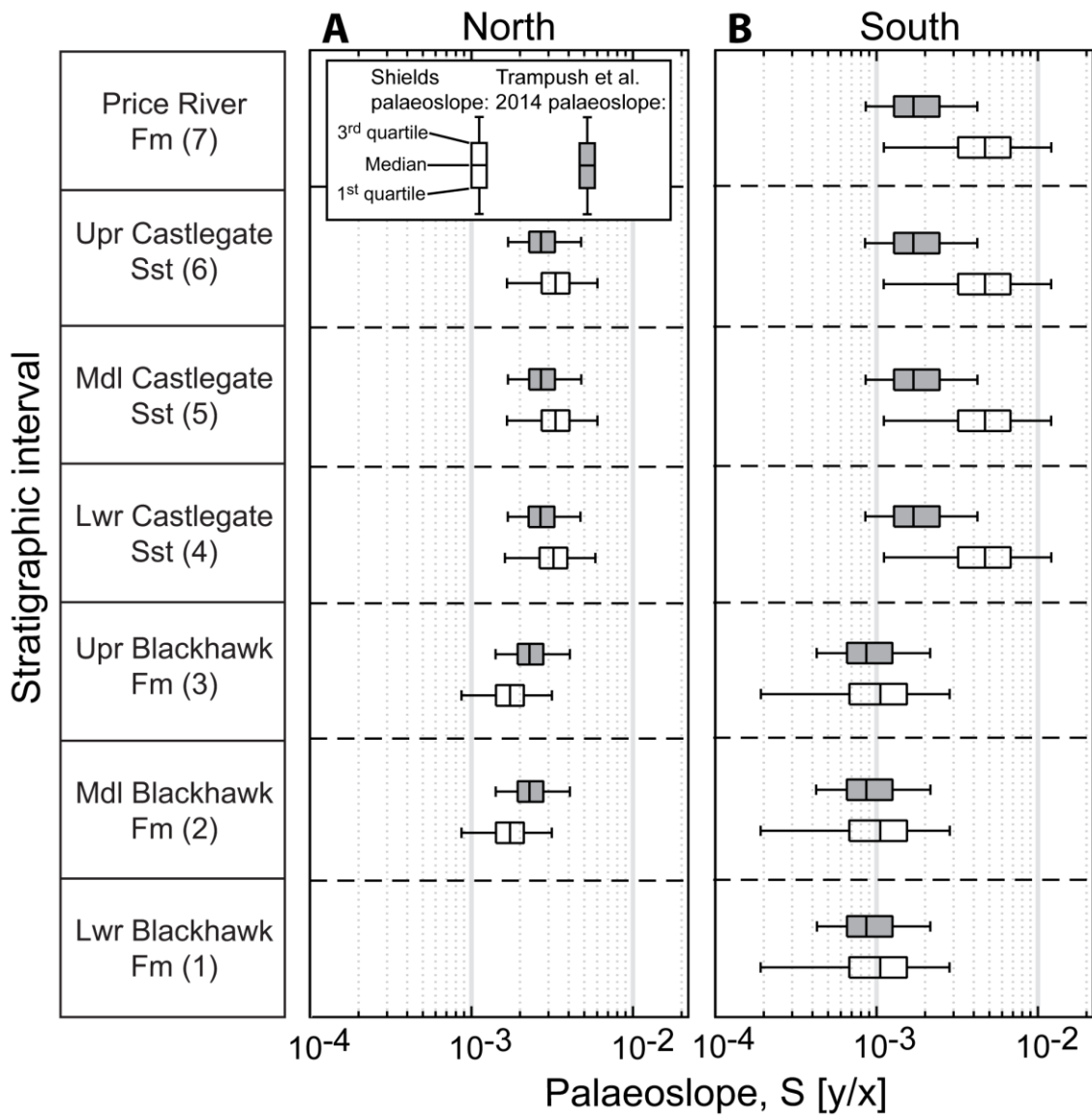
946

947 **Figure 6:** Reconstructed palaeoflow depths for the 5 parallel fluvial systems, for each stratigraphic
 948 interval (parts A–G), where possible, using mean cross-set heights. Results are presented as along-
 949 depositional strike transects from NNE (left; 0 km) to SSW (right; 125 km). Field sites span Price Canyon
 950 (PC), Wattis Road (WR), Straight Canyon (StC), Link Canyon (LC) and Salina Canyon (SC). Solid lines
 951 indicate median palaeoflow depths and dashed lines indicated the 1st and 3rd quartiles of palaeoflow
 952 depths. This figure is replicated in the Supplement alongside palaeoflow depths reconstructed from
 953 maximum cross-set heights (Supplementary Fig. S5).



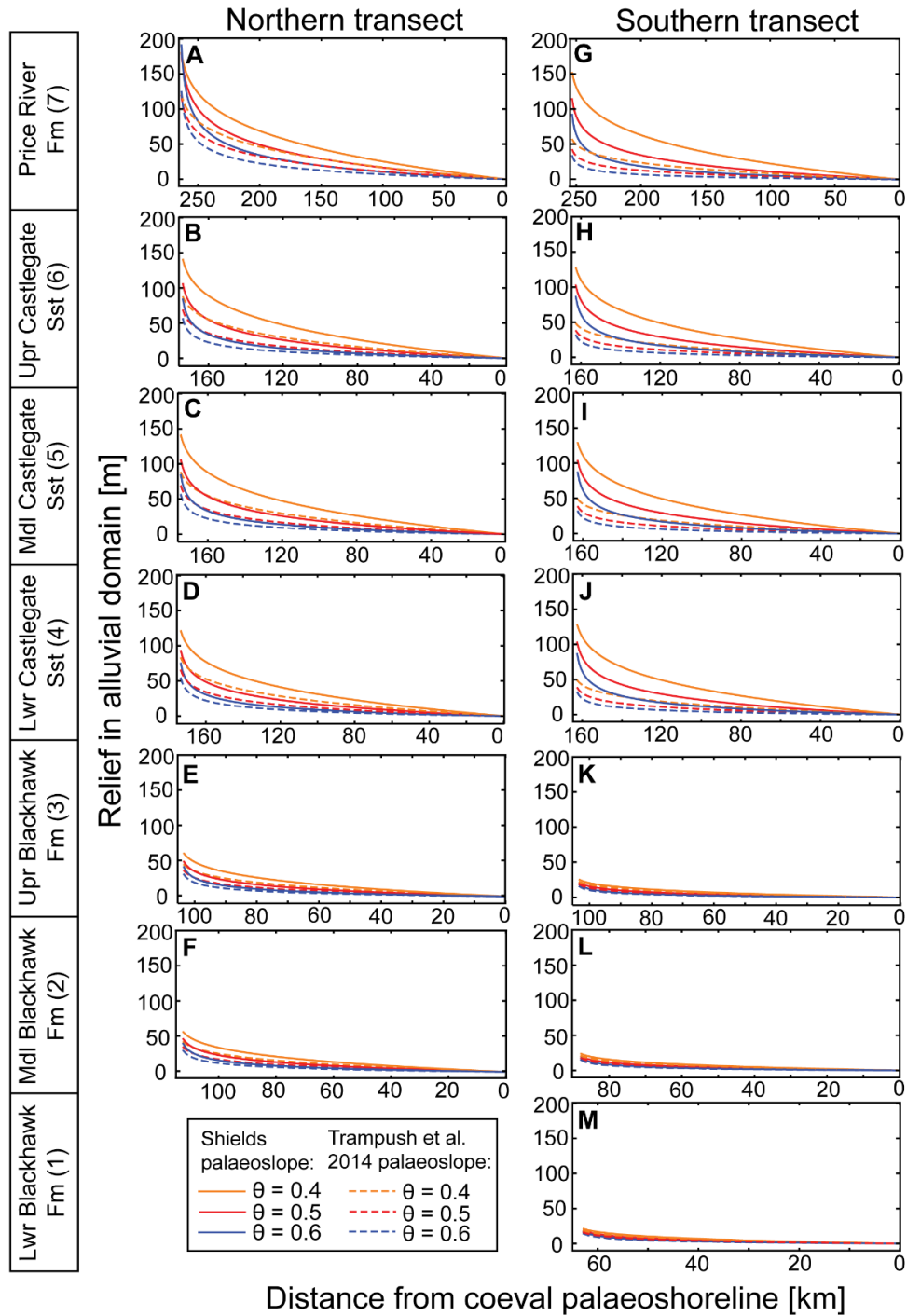
954

955 **Figure 7:** Up-dip to down-dip palaeoslope estimates for the defined northern and southern transects,
 956 using bulk grain-size data, for each stratigraphic interval (1–7), where possible. Parts A–F represent
 957 up-dip to down-dip palaeoslopes for the northern transect, from the middle Blackhawk Formation to
 958 the Price River Formation. Parts G–M represent up-dip to down-dip palaeoslopes for the southern
 959 transect, from the lower Blackhawk Formation to the Price River Formation. The central mark of each
 960 box indicates the median estimate, and the bottom and top edges of each box indicate the 1st and 3rd
 961 quartiles (or 25th and 75th percentiles), respectively. The whiskers extend to the most extreme
 962 estimates that are not considered to be outliers. Palaeoslope estimates are derived from 2
 963 independent approaches; boxes with no fill indicate estimates of palaeoslope derived using a Shields
 964 stress inversion (Equation 3) and boxes with grey fill indicate estimates derived from the method of
 965 Trampush et al. (2014) (Equation 4). BC = Bear Canyon; DH = Dry Hollow; LF = Lake Fork; MC = Mellor
 966 Canyon; PC = Price Canyon; SmC = Sixmile Canyon; StC = Straight Canyon.



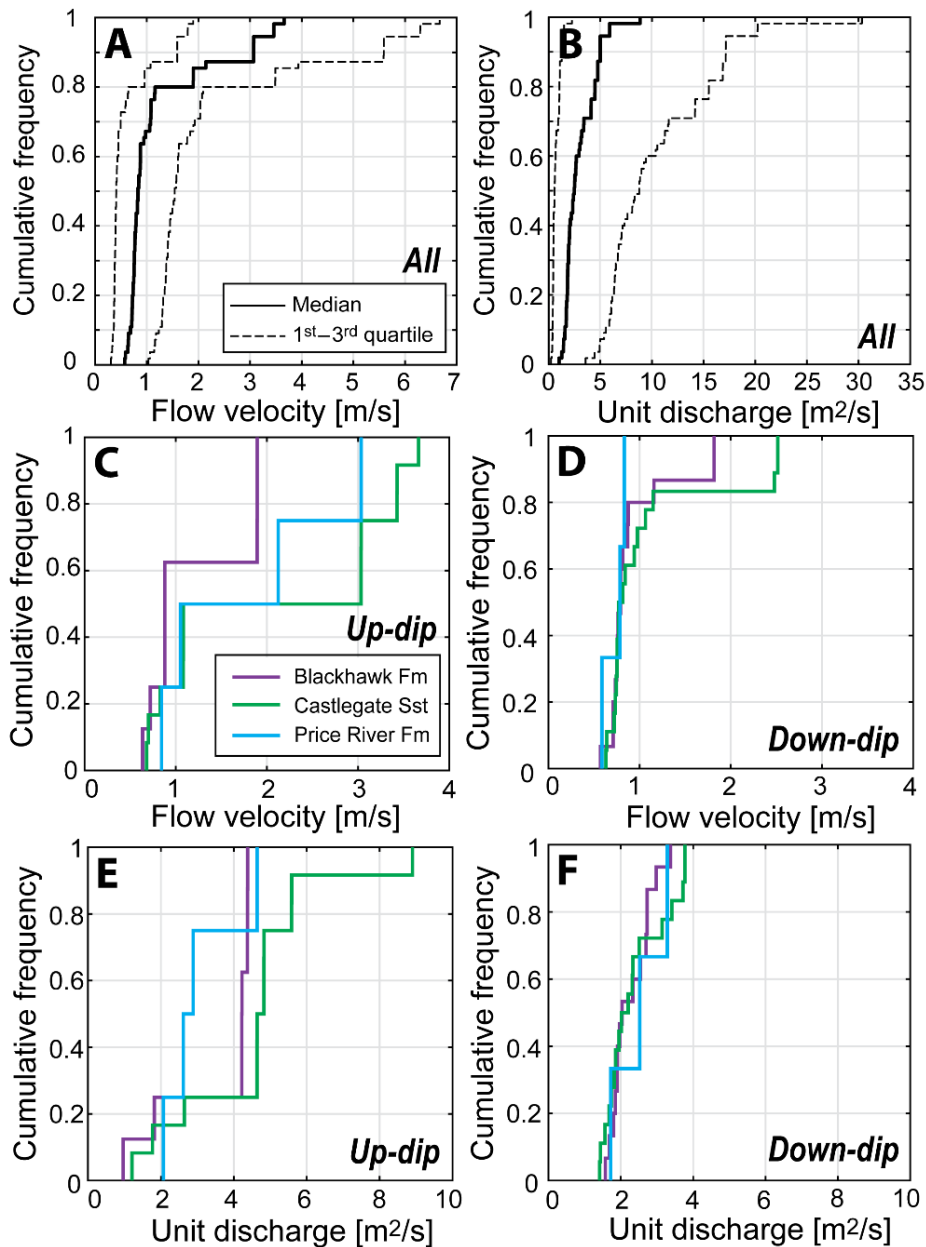
967

968 **Figure 8:** Palaeoslope estimates for the most up-dip location of the defined northern (part A) and
 969 southern (part B) depositional-dip transects, for each stratigraphic interval (1–7), where possible,
 970 using bulk grain-size data. The central mark of each box indicates the median estimate, and the edges
 971 of each box indicate the 1st and 3rd quartiles (or 25th and 75th percentiles) of estimates. The whiskers
 972 extend to the most extreme estimates that are not considered to be outliers. Palaeoslope estimates
 973 are derived from 2 independent approaches; boxes with no fill indicate estimates of palaeoslope
 974 derived using a Shields stress inversion (Equation 3) and boxes with grey fill indicate estimates derived
 975 from the method of Trampush et al. (2014) (Equation 4).



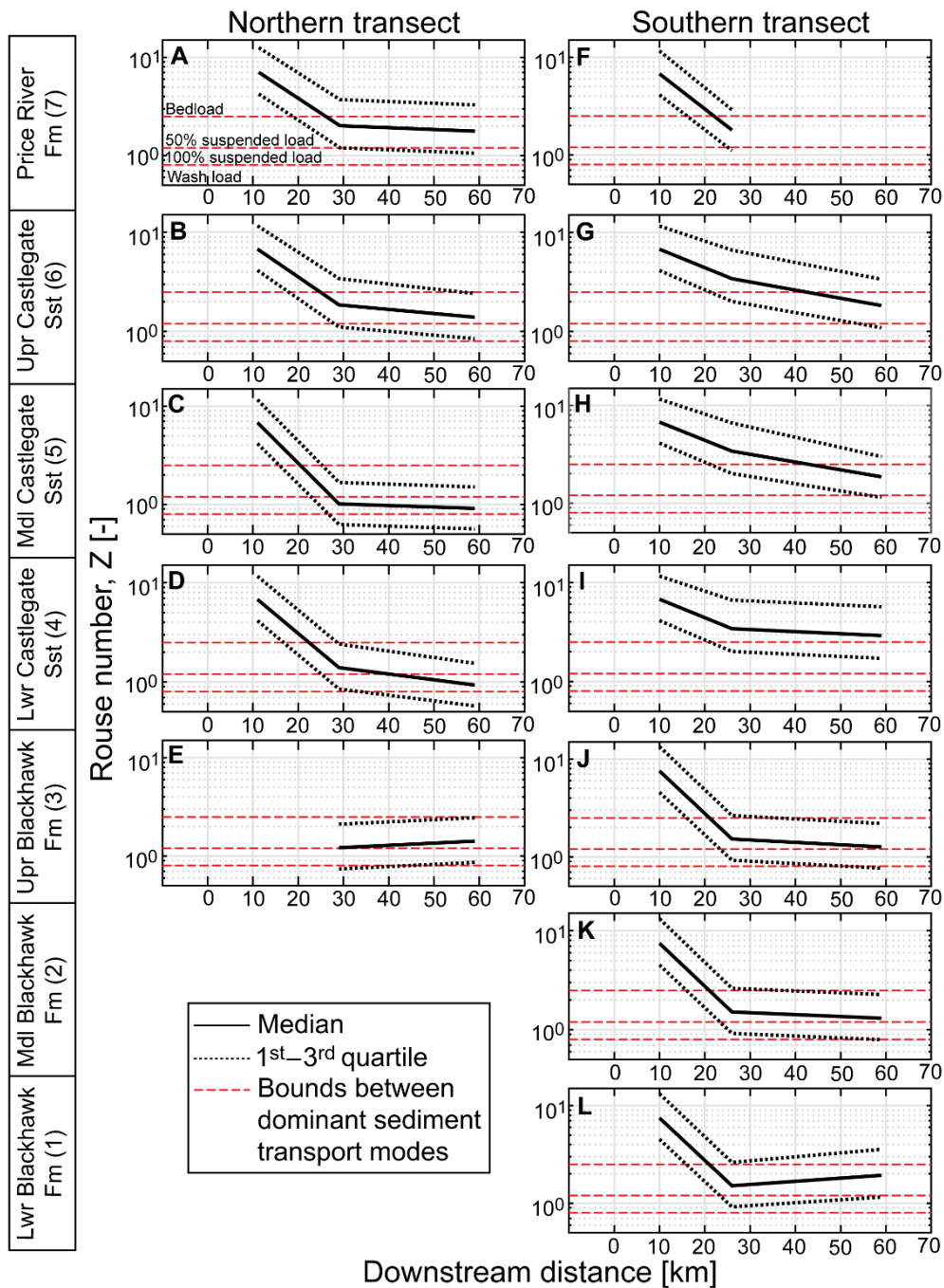
976

977 **Figure 9:** Estimated palaeorelief in the alluvial domain for the defined northern and southern
 978 transects, using bulk grain-size data, for each stratigraphic interval (1–7), where possible. Parts A–F
 979 depict estimated palaeorelief for the northern transect, from the middle Blackhawk Formation to the
 980 Price River Formation. Parts G–M depict estimated palaeorelief for the lower Blackhawk Formation to
 981 the Price River Formation. Palaeorelief estimates are derived using palaeoslope estimates from 2
 982 independent approaches; palaeoslopes from a Shields stress inversion (Equation 3) and palaeoslopes
 983 from the method of Trampush et al. (2014) (Equation 4). In addition, palaeorelief is estimated using a
 984 plausible range of values for the concavity index, θ . Unlike other depositional-dip transects in this
 985 study, the x axis instead depicts distance from the coeval palaeoshoreline (following Hettinger and
 986 Kirschbaum (2002); Hampson et al. (2012); Hampson et al. (2013)).



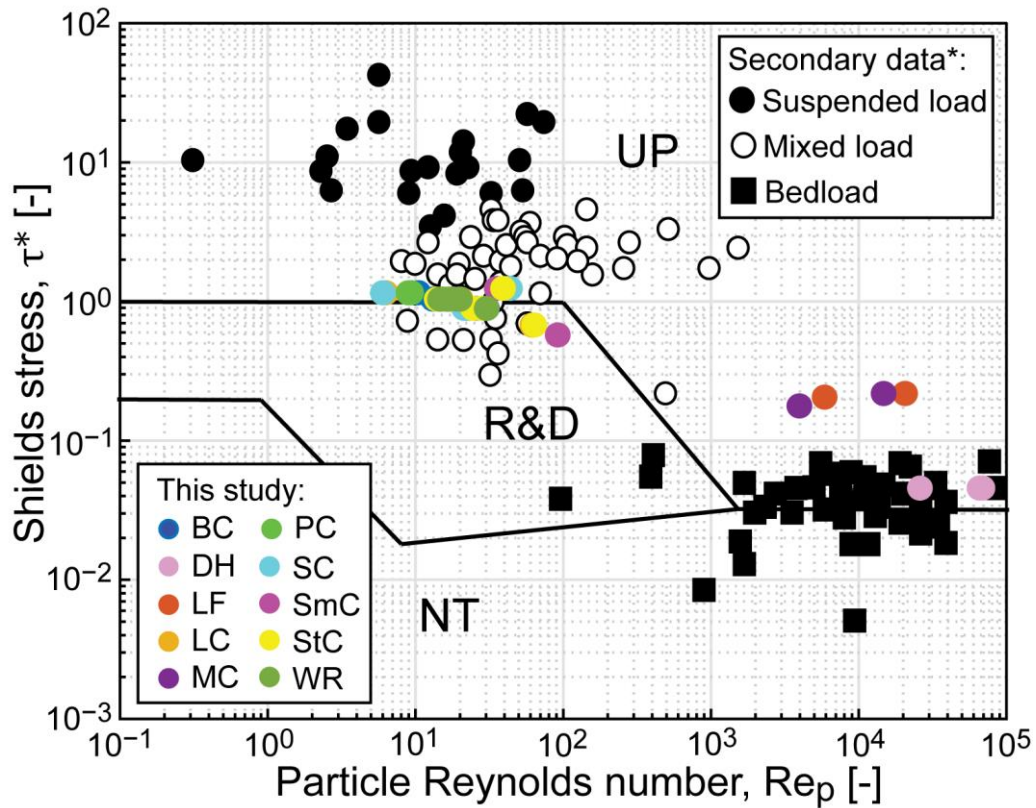
987

988 **Figure 10:** Cumulative frequency distributions of (part A) reconstructed flow velocities across all field
 989 areas and (part B) reconstructed water discharges, per unit width, across all field areas. Solid lines
 990 indicate median values and dashed lines indicates the 1st–3rd interquartile range. Flow velocities are
 991 derived using Manning’s formula (Equation 7), as described in the Methods section. Parts C–F depict
 992 flow velocities and unit water discharges split into up-dip and down-dip field sites. Down-dip field
 993 areas include field areas on the along-strike depositional transect (Price Canyon, Wattis Road, Straight
 994 Canyon, Link Canyon and Salina Canyon), meanwhile up-dip field areas include all those that are
 995 relatively up-dip (Dry Hollow, Lake Fork, Bear Canyon, Mellor Canyon, Sixmile Canyon). Field areas
 996 were also split into the Blackhawk Formation (and up-dip equivalents, i.e. intervals 1–3), Castlegate
 997 Sandstone (and up-dip equivalents, i.e. intervals 4–6) and Price River Formation (and up-dip
 998 equivalents, i.e. interval 7). Parts C and D depict cumulative frequency distributions of reconstructed
 999 flow velocities for up-dip (part C) and down-dip (part D) field areas, respectively. Parts E and F depict
 1000 cumulative frequency distributions of reconstructed unit water discharges for up-dip (part E) and
 1001 down-dip (part F) field areas, respectively.



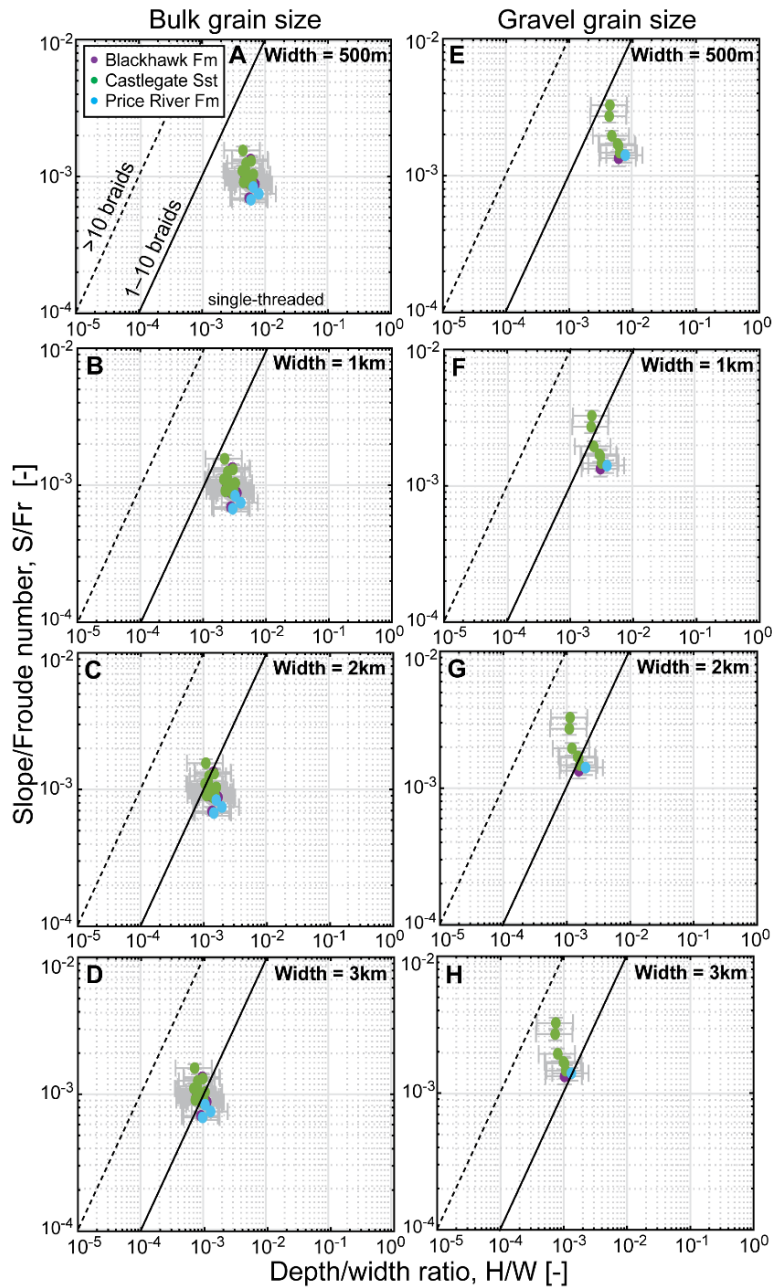
1002

1003 **Figure 11:** Estimated Rouse numbers, Z , for the defined northern and southern transects, using bulk
 1004 grain-size data, for each stratigraphic interval (1–7), where possible. Dominant mode of sediment
 1005 transport is typically wash load for $Z < 0.8$, 100% suspended load for $0.8 < Z < 1.2$, 50% suspended load
 1006 (i.e. mixed load) for $1.2 < Z < 2.5$, and bedload for $Z > 2.5$. Parts A–E represent up-dip to down-dip
 1007 Rouse numbers for the northern transect, from the upper Blackhawk Formation to the Price River
 1008 Formation. Parts F–L represent up-dip to down-dip Rouse numbers for the southern transect, from
 1009 the lower Blackhawk Formation to the Price River Formation. Solid black lines indicate the median
 1010 estimate and dashed black lines indicate the 1st and 3rd quartiles. Dashed red lines indicate the bounds
 1011 between differing dominant sediment transport modes, as labelled in part A.



1012

1013 **Figure 12:** Shields stress, τ^* , plotted as a function of particle Reynold's number, Re_p , for all field sites
 1014 and for each stratigraphic interval (1–7), where possible, using bulk grain size data. Colour-filled circles
 1015 indicate field results from this study for Bear Canyon (BC), Dry Hollow (DH), Lake Fork (LF), Link Canyon
 1016 (LC), Mellor Canyon (MC), Price Canyon (PC), Salina Canyon (SC), Sixmile Canyon (SmC), Straight
 1017 Canyon (StC) and Wattis Road (WR). *For comparison, this plot includes secondary data, originally
 1018 compiled by Dade and Friend (1998), from Leopold and Wolman (1957); Schumm (1968); Chitale
 1019 (1970); Church and Rood (1983); Andrews (1984), for characteristic dominant transport modes. Black
 1020 squares indicate bedload, white circles indicate mixed load, and black circles indicate suspended load.
 1021 Solid black lines indicate stability fields of different flow regimes: no sediment transport (NT), ripples
 1022 and dunes (R&D) and upper-stage plane beds (UP), in line with Allen (1982a, 1982b).



1023

1024 **Figure 13:** Theoretical stability fields of fluvial planform morphologies, i.e. single-thread and multi-
 1025 thread planforms, for both bulk grain-sizes (parts A–D) and gravel fraction grain-sizes (parts E–H),
 1026 where present (not all field localities possessed a gravel fraction). For both bulk and gravel grain-size
 1027 fractions, a range of river widths are assumed (500 m, 1 km, 2 km and 3 km) and used to calculate the
 1028 depth/width ratio. Data points are for all localities, in space and time, along the defined along-
 1029 depositional strike transect, i.e. these data points represent the five parallel fluvial systems and do not
 1030 consider up-dip localities. Data are further subdivided into the Blackhawk Formation (intervals 1–3),
 1031 Castlegate Sandstone (intervals 4–6) and Price River Formation (interval 7). Coloured markers and
 1032 error bars represent the median and the 1st–3rd interquartile range, respectively. Solid black lines
 1033 indicate the bounds of each stability field, and therefore the predicted transition from single-thread
 1034 (straight/meandering) to multi-thread (anabranching/braided) planform morphology. Dashed black
 1035 lines indicate a potential transition from 1–10 threads to >10 threads, based on modern data (G.
 1036 Parker, 1976).

1037 **References**

- 1038 Adams, M. M., & Bhattacharya, J. P. (2005). No change in fluvial style across a sequence boundary, Cretaceous
 1039 Blackhawk and Castlegate formations of central Utah, U.S.A. *Journal of Sedimentary Research*, 75(6),
 1040 1038-1051. doi:10.2110/jsr.2005.080
- 1041 Allen, J. R. L. (1982a). *Sedimentary Structures; Their Character and Physical Basis. Volume I* (Vol. 30).
 1042 Amsterdam: Elsevier.
- 1043 Allen, J. R. L. (1982b). *Sedimentary Structures; Their Character and Physical Basis. Volume II* (Vol. 30).
 1044 Amsterdam: Elsevier.
- 1045 Allen, P. A. (2008a). From landscapes into geological history. *Nature*, 451, 274-276. doi:10.1038/nature06586
- 1046 Allen, P. A. (2008b). Time scales of tectonic landscapes and their sediment routing systems. *Geological Society,
 1047 London, Special Publications*, 296(1), 7-28. doi:10.1144/sp296.2
- 1048 Allen, P. A., Armitage, J. J., Carter, A., Duller, R. A., Michael, N. A., Sinclair, H. D., . . . Whittaker, A. C. (2013).
 1049 The Qs problem: Sediment volumetric balance of proximal foreland basin systems. *Sedimentology*,
 1050 60(1), 102-130. doi:10.1111/sed.12015
- 1051 Allmendinger, R. W. (1992). Fold and thrust tectonics of the western United States exclusive of the accreted
 1052 terranes. In B. C. Burchfiel, P. W. Lipman, & M. L. Zoback (Eds.), *The Cordilleran Orogen: Geological
 1053 Society of America*.
- 1054 Andrews, E. D. (1984). Bed-material entrainment and hydraulic geometry of gravel-bed rivers in Colorado. *GSA
 1055 Bulletin*, 95(3), 371-378. doi:10.1130/0016-7606(1984)95<371:BEAHGO>2.0.CO;2
- 1056 Armitage, J. J., Duller, R. A., Whittaker, A. C., & Allen, P. A. (2011). Transformation of tectonic and climatic
 1057 signals from source to sedimentary archive. *Nature Geoscience*, 4(4), 231-235. doi:10.1038/ngeo1087
- 1058 Armstrong, R. L. (1968). Sevier Orogenic Belt in Nevada and Utah. *GSA Bulletin*, 79(4), 429-458.
 1059 doi:10.1130/0016-7606(1968)79[429:SOBINA]2.0.CO;2
- 1060 Aschoff, J., & Steel, R. (2011a). Anatomy and development of a low-accommodation clastic wedge, upper
 1061 Cretaceous, Cordilleran Foreland Basin, USA. *Sedimentary Geology*, 236(1), 1-24.
 1062 doi:10.1016/j.sedgeo.2010.10.006
- 1063 Aschoff, J., & Steel, R. (2011b). Anomalous clastic wedge development during the Sevier-Laramide transition,
 1064 North American Cordilleran foreland basin, USA. *GSA Bulletin*, 123(9-10), 1822-1835.
 1065 doi:10.1130/B30248.1
- 1066 Bartschi, N. C., Saylor, J. E., Lapen, T. J., Blum, M. D., Pettit, B. S., & Andrea, R. A. (2018). Tectonic controls on
 1067 Late Cretaceous sediment provenance and stratigraphic architecture in the Book Cliffs, Utah. *GSA
 1068 Bulletin*, 130(11-12), 1763-1781. doi:10.1130/B31927.1
- 1069 Bhattacharya, J., & Tye, B. (2004). Searching for modern Ferron analogs and application to subsurface
 1070 interpretation. In T. C. Chidsey Jr., R. D. Adams, & T. H. Morris (Eds.), *Regional to Wellbore Analog for
 1071 Fluvial-Deltaic Reservoir Modeling: The Ferron Sandstone of Utah* (Vol. 50, pp. 39-57): AAPG Studies in
 1072 Geology.
- 1073 Bhattacharya, J. P., Copeland, P., Lawton, T. F., & Holbrook, J. (2016). Estimation of source area, river paleo-
 1074 discharge, paleoslope, and sediment budgets of linked deep-time depositional systems and
 1075 implications for hydrocarbon potential. *Earth-Science Reviews*, 153, 77-110.
 1076 doi:10.1016/j.earscirev.2015.10.013
- 1077 Bhattacharyya, P., Bhattacharya, J. P., & Khan, S. D. (2015). Paleo-channel reconstruction and grain size
 1078 variability in fluvial deposits, Ferron Sandstone, Notom Delta, Hanksville, Utah. *Sedimentary Geology*,
 1079 325, 17-25. doi:10.1016/j.sedgeo.2015.05.001
- 1080 Boulton, S. J., & Whittaker, A. C. (2009). Quantifying the slip rates, spatial distribution and evolution of active
 1081 normal faults from geomorphic analysis: Field examples from an oblique-extensional graben,
 1082 southern Turkey. *Geomorphology*, 104(3), 299-316. doi:10.1016/j.geomorph.2008.09.007
- 1083 Bradley, R. W., & Venditti, J. G. (2017). Reevaluating dune scaling relations. *Earth-Science Reviews*, 165, 356-
 1084 376. doi:10.1016/j.earscirev.2016.11.004

- 1085 Brewer, C. J., Hampson, G. J., Whittaker, A. C., Roberts, G. G., & Watkins, S. E. (2020). Comparison of methods
 1086 to estimate sediment flux in ancient sediment routing systems. *Earth-Science Reviews*, 207, 103217.
 1087 doi:10.1016/j.earscirev.2020.103217
- 1088 Bridge, J. S., & Mackey, S. D. (1993). A revised alluvial stratigraphy model. In M. Marzo & C. Puigdefábregas
 1089 (Eds.), *Alluvial Sedimentation* (pp. 317-336): Wiley-Blackwell.
- 1090 Bridge, J. S., & Tye, B. (2000). Interpreting the dimensions of ancient fluvial channel bars, channels, and
 1091 channel belts from wireline-logs and cores. *AAPG Bulletin*, 84(8), 1205-1228. doi:10.1306/A9673C84-
 1092 1738-11D7-8645000102C1865D
- 1093 Brooke, S. A. S., Whittaker, A., Armitage, J. J., D'Arcy, M., & Watkins, S. E. (2018). Quantifying sediment
 1094 transport dynamics on alluvial fans from spatial and temporal changes in grain size, Death Valley,
 1095 California. *Journal of Geophysical Research: Earth Surface*, 123, 2039-2067.
- 1096 Bruhn, R. L., Picard, M. D., & Isby, J. S. (1986). Tectonics and Sedimentology of Uinta Arch, Western Uinta
 1097 Mountains, and Uinta Basin. In J. A. Peterson (Ed.), *Paleotectonics and sedimentation in the Rocky
 1098 Mountain Region, United States* (Vol. 41): American Association of Petroleum Geologists.
- 1099 Bryant, B., & Nichols, D. J. (1988). Late Mesozoic and early Tertiary reactivation of an ancient crustal boundary
 1100 along the Uinta trend and its interaction with the Sevier orogenic belt. In C. J. Schmidt & W. J. Perry,
 1101 Jr. (Eds.), *Interaction of the Rocky Mountain Foreland and the Cordilleran Thrust Belt* (Vol. 171):
 1102 Geological Society of America.
- 1103 Buhler, P. B., Fassett, C. I., Head, J. W., & Lamb, M. P. (2014). Timescales of fluvial activity and intermittency in
 1104 Milna Crater, Mars. *Icarus*, 241, 130-147. doi:10.1016/j.icarus.2014.06.028
- 1105 Carling, P. A. (1999). Subaqueous gravel dunes. *Journal of Sedimentary Research*, 69(3), 534-545.
 1106 doi:10.2110/jsr.69.534
- 1107 Carlston, C. W. (1969). Longitudinal slope characteristics of rivers of the midcontinent and the Atlantic east gulf
 1108 slopes. *International Association of Scientific Hydrology - Bulletin*, 14(4), 21-31.
 1109 doi:10.1080/02626666909493751
- 1110 Castelltort, S., Goren, L., Willett, S. D., Champagnac, J.-D., Herman, F., & Braun, J. (2012). River drainage
 1111 patterns in the New Zealand Alps primarily controlled by plate tectonic strain. *Nature Geoscience*,
 1112 5(10), 744-748. doi:10.1038/ngeo1582
- 1113 Castelltort, S., Simpson, G., & Darrioulat, A. (2009). Slope-control on the aspect ratio of river basins. *Terra
 1114 Nova*, 21(4), 265-270. doi:10.1111/j.1365-3121.2009.00880.x
- 1115 Castelltort, S., & Van Den Driessche, J. (2003). How plausible are high-frequency sediment supply-driven cycles
 1116 in the stratigraphic record? *Sedimentary Geology*, 157(1), 3-13. doi:10.1016/S0037-0738(03)00066-6
- 1117 Chamberlin, E. P., & Hajek, E. A. (2019). Using bar preservation to constrain reworking in channel-dominated
 1118 fluvial stratigraphy. *Geology*, 47(6), 531-534. doi:10.1130/G46046.1
- 1119 Champagnac, J.-D., Molnar, P., Sue, C., & Herman, F. (2012). Tectonics, climate, and mountain topography.
 1120 *Journal of Geophysical Research: Solid Earth*, 117(B2). doi:10.1029/2011JB008348
- 1121 Chase, C. G., Gregory-Wodzicki, K. M., Parrish, J. T., & DeCelles, P. G. (1998). Topographic history of the
 1122 Western Cordillera of North America and controls on climate. In T. J. Crowley & K. Burke (Eds.),
 1123 *Tectonic Boundary Conditions for Climate Reconstructions* (Vol. 39, pp. 73-99): Oxford Monographs on
 1124 Geology and Geophysics.
- 1125 Chen, C., Guertl, L., Foreman, B. Z., Hassenruck-Gudipati, H. J., Adatte, T., Honegger, L., . . . Castelltort, S.
 1126 (2018). Estimating regional flood discharge during Palaeocene-Eocene global warming. *Scientific
 1127 Reports*, 8(1), 13391. doi:10.1038/s41598-018-31076-3
- 1128 Chitale, S. V. (1970). River Channel Patterns. *Journal of Hydraulic Division American Society Civil Engineering*,
 1129 96, 201-221.
- 1130 Church, M., & Rood, K. (1983). *Catalogue of Alluvial River Channel Regime Data* (Vol. 99). Vancouver:
 1131 University of British Columbia.
- 1132 Cobban, W. A., McKinney, K. C., Obradovich, J. D., & Walasczyk, I. (2006). A USGS zonal table for the Upper
 1133 Cretaceous Middle Cenomanian–Maastrichtian of the Western Interior of the United States based on

1134 Ammonites, Inoceramids, and radiometric ages: U.S. Geological Survey, Open-File Report 2006-1250.
1135 1-46.

1136 Colombera, L., Arévalo, O. J., & Mountney, N. P. (2017). Fluvial-system response to climate change: The
1137 Paleocene-Eocene Tresp Group, Pyrenees, Spain. *Global and Planetary Change*, *157*, 1-17.
1138 doi:10.1016/j.gloplacha.2017.08.011

1139 Constenius, K., Esser, R., & Layer, P. (2003). Extensional collapse of the Charleston-Nebo salient and its
1140 relationship to space-time variations in Cordilleran orogenic belt tectonism and continental
1141 stratigraphy. *Cenozoic systems of the Rocky Mountain region*, Reynolds, R.G. and Flores, R. M.,
1142 eds., *Rocky Mountain Section, Society of Economic Paleontologists and Mineralogists*, 303-353.

1143 Crowley, K. D. (1983). Large-scale bed configurations (macroforms), Platte River Basin, Colorado and Nebraska:
1144 Primary structures and formative processes. *GSA Bulletin*, *94*(1), 117-133. doi:10.1130/0016-
1145 7606(1983)94<117:LBCMPR>2.0.CO;2

1146 D'Arcy, M., & Whittaker, A. C. (2014). Geomorphic constraints on landscape sensitivity to climate in
1147 tectonically active areas. *Geomorphology*, *204*, 366-381. doi:10.1016/j.geomorph.2013.08.019

1148 D'Arcy, M., Whittaker, A. C., & Roda-Boluda, D. C. (2017). Measuring alluvial fan sensitivity to past climate
1149 changes using a self-similarity approach to grain-size fining, Death Valley, California. *Sedimentology*,
1150 *64*(2), 388-424. doi:10.1111/sed.12308

1151 Dade, W. B., & Friend, P. F. (1998). Grain size, sediment transport regime, and channel slope in alluvial rivers.
1152 *The Journal of Geology*, *106*(6), 661-676. doi:10.1086/516052

1153 DeCelles, P. G. (1994). Late Cretaceous–Paleocene synorogenic sedimentation and kinematic history of the
1154 Sevier thrust belt, northeast Utah and southwest Wyoming. *GSA Bulletin*, *106*, 32-56.
1155 doi:10.1130/0016-7606(1994)106<0032:LCPSSA>2.3.CO;2

1156 DeCelles, P. G. (2004). Late Jurassic to Eocene evolution of the Cordilleran thrust belt and foreland basin
1157 system, western U.S.A. *American Journal of Science*, *304*. doi:10.2475/ajs.304.2.105

1158 DeCelles, P. G., & Coogan, J. C. (2006). Regional structure and kinematic history of the Sevier fold-and-thrust
1159 belt, central Utah. *GSA Bulletin*, *118*(7/8), 841-864. doi:10.1130/B25759.1

1160 DiBiase, R. A., & Whipple, K. X. (2011). The influence of erosion thresholds and runoff variability on the
1161 relationships among topography, climate, and erosion rate. *Journal of Geophysical Research: Earth
1162 Surface*, *116*(F4). doi:10.1029/2011JF002095

1163 DiBiase, R. A., Whipple, K. X., Heimsath, A. M., & Ouimet, W. B. (2010). Landscape form and millennial erosion
1164 rates in the San Gabriel Mountains, CA. *Earth and Planetary Science Letters*, *289*(1), 134-144.
1165 doi:10.1016/j.epsl.2009.10.036

1166 Duller, R. A., Armitage, J. J., Manners, H. R., Grimes, S., & Jones, T. D. (2019). Delayed sedimentary response to
1167 abrupt climate change at the Paleocene-Eocene boundary, northern Spain. *Geology*, *47*(2), 159-162.
1168 doi:10.1130/G45631.1

1169 Duller, R. A., Whittaker, A. C., Fedele, J. J., Whitchurch, A. L., Springett, J., Smithells, R., . . . Allen, P. A. (2010).
1170 From grain size to tectonics. *Journal of Geophysical Research: Earth Surface*, *115*(F3), F03022.
1171 doi:10.1029/2009JF001495

1172 Eide, C. H., Müller, R., & Helland-Hansen, W. (2018). Using climate to relate water discharge and area in
1173 modern and ancient catchments. *Sedimentology*, *65*(4), 1378-1389. doi:10.1111/sed.12426

1174 Ferguson, R. I., & Church, M. (2004). A simple universal equation for grain settling velocity. *Journal of
1175 Sedimentary Research*, *74*(6), 933-937. doi:10.1306/051204740933

1176 Flint, J. J. (1974). Stream gradient as a function of order, magnitude, and discharge. *Water Resources Research*,
1177 *10*(5), 969-973. doi:10.1029/WR010i005p00969

1178 Flood, Y. S., & Hampson, G. J. (2014). Facies and architectural analysis to interpret avulsion style and variability:
1179 Upper Cretaceous Blackhawk Formation, Wasatch Plateau, central Utah, U.S.A. *Journal of
1180 Sedimentary Research*, *84*(9), 743-762. doi:10.2110/jsr.2014.59

1181 Flood, Y. S., & Hampson, G. J. (2015). Quantitative analysis of the dimensions and distribution of channelized
1182 fluvial sandbodies within a large outcrop dataset: Upper Cretaceous Blackhawk Formation, Wasatch

1183 Plateau, central Utah, U.S.A. *Journal of Sedimentary Research*, 85(4), 315-336.
1184 doi:10.2110/jsr.2015.25

1185 Foreman, B. Z. (2014). Climate-driven generation of a fluvial sheet sand body at the Paleocene–Eocene
1186 boundary in northwest Wyoming (USA). *Basin Research*, 26, 225-241. doi:10.1111/bre.12027

1187 Foreman, B. Z., Heller, P. L., & Clementz, M. T. (2012). Fluvial response to abrupt global warming at the
1188 Palaeocene/Eocene boundary. *Nature*, 491, 92-95. doi:10.1038/nature11513

1189 Foreman, B. Z., Roberts, E. M., Tapanila, L., Ratigan, D., & Sullivan, P. (2015). Stable isotopic insights into
1190 paleoclimatic conditions and alluvial depositional processes in the Kaiparowits Formation
1191 (Campanian, south-central Utah, U.S.A.). *Cretaceous Research*, 56, 180-192.
1192 doi:10.1016/j.cretres.2015.05.001

1193 Fotherby, L. M. (2009). Valley confinement as a factor of braided river pattern for the Platte River.
1194 *Geomorphology*, 103(4), 562-576. doi:10.1016/j.geomorph.2008.08.001

1195 Fouch, T. D., Lawton, T. F., Nichols, D. J., Cashion, W. B., & Cobban, W. A. (1983). Patterns and timing of
1196 synorogenic sedimentation in Upper Cretaceous rocks of central and northeast Utah. In M. W.
1197 Reynolds & E. D. Dolly (Eds.), *Mesozoic Paleogeography of West-Central United States* (pp. 305-336):
1198 SEPM Rocky Mountain Section.

1199 Fricke, H. C., Foreman, B. Z., & Sewall, J. O. (2010). Integrated climate model-oxygen isotope evidence for a
1200 North American monsoon during the Late Cretaceous. *Earth and Planetary Science Letters*, 289(1-2),
1201 11-21. doi:10.1016/j.epsl.2009.10.018

1202 Ganti, V., Hajek, E. A., Leary, K., Straub, K. M., & Paola, C. (2020). Morphodynamic hierarchy and the fabric of
1203 the sedimentary record. *Geophysical Research Letters*, 47(14), e2020GL087921.
1204 doi:10.1029/2020GL087921

1205 Ganti, V., Lamb, M. P., & Chadwick, A. J. (2019a). Autogenic erosional surfaces in fluvio-deltaic stratigraphy
1206 from floods, avulsions, and backwater hydrodynamics. *Journal of Sedimentary Research*, 89(8), 815-
1207 832. doi:10.2110/jsr.2019.40

1208 Ganti, V., Lamb, M. P., & McElroy, B. (2014). Quantitative bounds on morphodynamics and implications for
1209 reading the sedimentary record. *Nature Communications*, 5(1), 3298. doi:10.1038/ncomms4298

1210 Ganti, V., Paola, C., & Fofoula-Georgiou, E. (2013). Kinematic controls on the geometry of the preserved cross
1211 sets. *Journal of Geophysical Research: Earth Surface*, 118(3), 1296-1307. doi:10.1002/jgrf.20094

1212 Ganti, V., Whittaker, A., Lamb, M. P., & Fischer, W. W. (2019b). Low-gradient, single-threaded rivers prior to
1213 greening of the continents. *Proceedings of the National Academy of Sciences*, 116(4), 11652-11657.
1214 doi:10.1073/pnas.1901642116

1215 Gill, M. A. (1971). Height of sand dunes in open channel flows. *Journal of the Hydraulics Division*, 97(12), 2067-
1216 2074.

1217 Hack, J. T. (1957). Studies of longitudinal stream profiles in Virginia and Maryland. *U.S. Geological Survey*
1218 *Professional Paper*, 294-B, 45-97.

1219 Hack, J. T. (1973). Stream profile analysis and stream gradient index. *US Geological Survey Journal of Research*,
1220 1, 421-429.

1221 Hajek, E. A., & Heller, P. L. (2012). Flow-depth scaling in alluvial architecture and nonmarine sequence
1222 stratigraphy: Example from the Castlegate Sandstone, central Utah, U.S.A. *Journal of Sedimentary*
1223 *Research*, 82(2), 121-130. doi:10.2110/jsr.2012.8

1224 Hajek, E. A., Heller, P. L., & Sheets, B. A. (2010). Significance of channel-belt clustering in alluvial basins.
1225 *Geology*, 38(6), 535-538. doi:10.1130/G30783.1

1226 Hajek, E. A., & Wolinsky, M. A. (2012). Simplified process modeling of river avulsion and alluvial architecture:
1227 Connecting models and field data. *Sedimentary Geology*, 257-260, 1-30.
1228 doi:10.1016/j.sedgeo.2011.09.005

1229 Hampson, G. J. (2010). Sediment dispersal and quantitative stratigraphic architecture across an ancient shelf.
1230 *Sedimentology*, 57(1), 96-141. doi:10.1111/j.1365-3091.2009.01093.x

- 1231 Hampson, G. J., Duller, R. A., Petter, A. L., Robinson, R. A. J., & Allen, P. A. (2014). Mass-balance constraints on
1232 stratigraphic interpretation of linked alluvial-coastal-shelfal deposits from source to sink: example
1233 from Cretaceous Western Interior Basin, Utah and Colorado, U.S.A. *Journal of Sedimentary Research*,
1234 84(11), 935-960. doi:10.2110/jsr.2014.78
- 1235 Hampson, G. J., Jewell, T. O., Irfan, N., Gani, M. R., & Bracken, B. (2013). Modest change in fluvial style with
1236 varying accommodation in regressive alluvial-to-coastal-plain wedge: Upper Cretaceous Blackhawk
1237 Formation, Wasatch Plateau, central Utah, U.S.A. *Journal of Sedimentary Research*, 83(2), 145-169.
1238 doi:10.2110/jsr.2013.8
- 1239 Hampson, G. J., Royhan Gani, M., Sahoo, H., Rittersbacher, A., Irfan, N., Ranson, A., . . . Bracken, B. (2012).
1240 Controls on large-scale patterns of fluvial sandbody distribution in alluvial to coastal plain strata:
1241 Upper Cretaceous Blackhawk Formation, Wasatch Plateau, Central Utah, USA. *Sedimentology*, 59(7),
1242 2226-2258. doi:10.1111/j.1365-3091.2012.01342.x
- 1243 Hay, W., L. Eicher, D., & Diner, R. (1993). Physical oceanography and water masses of the Cretaceous Western
1244 Interior Seaway. In W. E. G. Caldwell & E. G. Kauffman (Eds.), *Evolution of the Western Interior Basin*
1245 (pp. 297-318): Geological Association of Canada.
- 1246 Hayden, A. T., Lamb, M. P., Fischer, W. W., Ewing, R. C., McElroy, B. J., & Williams, R. M. E. (2019). Formation of
1247 sinuous ridges by inversion of river-channel belts in Utah, USA, with implications for Mars. *Icarus*, 332,
1248 92-110. doi:10.1016/j.icarus.2019.04.019
- 1249 Hettinger, R. D., & Kirschbaum, M. A. (2002). Stratigraphy of the Upper Cretaceous Mancos Shale (upper part)
1250 and Mesaverde Group in the southern part of the Uinta and Piceance basins, Utah and Colorado.
1251 *USGS Geologic Investigation Series: IMAP*, 2764, 21. doi:10.3133/i2764
- 1252 Holbrook, J., & Wanas, H. (2014). A fulcrum approach to assessing source-to-sink mass balance using channel
1253 paleohydrologic parameters derivable from common fluvial data sets with an example from the
1254 Cretaceous of Egypt. *Journal of Sedimentary Research*, 84(5), 349-372. doi:10.2110/jsr.2014.29
- 1255 Horton, B. K., Constenius, K. N., & DeCelles, P. G. (2004). Tectonic control on coarse-grained foreland-basin
1256 sequences: An example from the Cordilleran foreland basin, Utah. *Geology*, 32(7), 637-640.
1257 doi:10.1130/G20407.1
- 1258 Hovius, N. (1996). Regular spacing of drainage outlets from linear mountain belts. *Basin Research*, 8(1), 29-44.
1259 doi:10.1111/j.1365-2117.1996.tb00113.x
- 1260 Jerolmack, D. J., & Mohrig, D. (2005). Frozen dynamics of migrating bedforms. *Geology*, 33(1), 57-60.
1261 doi:10.1130/G20897.1
- 1262 Jerolmack, D. J., & Paola, C. (2010). Shredding of environmental signals by sediment transport. *Geophysical*
1263 *Research Letters*, 37(19), 1-5. doi:10.1029/2010gl044638
- 1264 Jerolmack, D. J., & Sadler, P. (2007). Transience and persistence in the depositional record of continental
1265 margins. *Journal of Geophysical Research: Earth Surface*, 112(F3). doi:10.1029/2006JF000555
- 1266 Jinnah, Z. A., Roberts, E. M., Deino, A. L., Larsen, J. S., Link, P. K., & Fanning, C. M. (2009). New ⁴⁰Ar-³⁹Ar and
1267 detrital zircon U-Pb ages for the Upper Cretaceous Wahweap and Kaiparowits formations on the
1268 Kaiparowits Plateau, Utah: Implications for regional correlation, provenance, and biostratigraphy.
1269 *Cretaceous Research*, 30(2), 287-299. doi:10.1016/j.cretres.2008.07.012
- 1270 Kauffman, E. G. (1977). Geological and biological overview: Western Interior Basin In E. G. Kauffman (Ed.),
1271 *Cretaceous facies, faunas, and paleoenvironments across the Western Interior Basin* (pp. 75-99):
1272 Rocky Mountain Association of Geologists.
- 1273 Kauffman, E. G., & Caldwell, W. (1993). The Western Interior Basin in space and time. In E. G. Kauffman & W.
1274 Caldwell (Eds.), *Evolution of the Western Interior Basin: Geological Association of Canada, Special*
1275 *Paper 39* (pp. 1-30).
- 1276 Kirby, E., & Whipple, K. (2001). Quantifying differential rock-uplift rates via stream profile analysis. *Geology*,
1277 29(5), 415-418. doi:10.1130/0091-7613(2001)029<0415:QDRURV>2.0.CO;2
- 1278 Kirby, E., & Whipple, K. X. (2012). Expression of active tectonics in erosional landscapes. *Journal of Structural*
1279 *Geology*, 44, 54-75. doi:10.1016/j.jsg.2012.07.009

1280 Kirby, E., Whipple, K. X., Tang, W., & Chen, Z. (2003). Distribution of active rock uplift along the eastern margin
1281 of the Tibetan Plateau: Inferences from bedrock channel longitudinal profiles. *Journal of Geophysical*
1282 *Research: Solid Earth*, 108(B4). doi:10.1029/2001JB000861

1283 Lamb, M. P., Grotzinger, J. P., Southard, J. B., & Tosca, N. J. (2012). Were aqueous ripples on Mars formed by
1284 flowing brines? In J. P. Grotzinger & R. E. Milliken (Eds.), *Sedimentary Geology of Mars* (Vol. 102):
1285 SEPM Society for Sedimentary Geology.

1286 Lapôtre, M. G. A., Ielpi, A., Lamb, M. P., Williams, R. M. E., & Knoll, A. H. (2019). Model for the formation of
1287 single-thread rivers in barren landscapes and implications for pre-Silurian and Martian fluvial
1288 deposits. *Journal of Geophysical Research: Earth Surface*, 124(12), 2757-2777.
1289 doi:10.1029/2019JF005156

1290 Lawton, T. F. (1982). Lithofacies correlations within the Upper Cretaceous Indianola Group, central Utah. *Utah*
1291 *Geological Association Publication*, 10, 199-213.

1292 Lawton, T. F. (1983). Late Cretaceous fluvial systems and the age of foreland uplifts in central Utah. In J. D.
1293 Lowell (Ed.), *Rocky Mountain Foreland Basins and Uplifts* (pp. 181-199). Denver: Rocky Mountain
1294 Association of Geologists.

1295 Lawton, T. F. (1986a). Compositional trends within a clastic wedge adjacent to a fold-thrust belt: Indianola
1296 Group, central Utah, USA. In P. A. Allen & P. Homewood (Eds.), *Foreland Basins* (pp. 411-423).
1297 London: Blackwell.

1298 Lawton, T. F. (1986b). Fluvial Systems of the Upper Cretaceous Mesaverde Group and Paleocene North Horn
1299 Formation, Central Utah: A Record of Transition from Thin-Skinned to Thick-Skinned Deformation in
1300 the Foreland Region. In J. A. Peterson (Ed.), *Paleotectonics and sedimentation in the Rocky Mountain*
1301 *Region, United States* (Vol. 41): American Association of Petroleum Geologists.
1302 doi:10.1306/M41456C20

1303 Lawton, T. F., Pollock, S. L., & Robinson, R. A. J. (2003). Integrating sandstone petrology and nonmarine
1304 sequence stratigraphy: application to the Late Cretaceous fluvial systems of southwestern Utah, USA.
1305 *Journal of Sedimentary Research*, 73, 398-406.

1306 Leary, K. C. P., & Ganti, V. (2020). Preserved fluvial cross strata record bedform disequilibrium dynamics.
1307 *Geophysical Research Letters*, 47(2), e2019GL085910. doi:10.1029/2019GL085910

1308 Leclair, S. F. (2002). Preservation of cross-strata due to the migration of subaqueous dunes: an experimental
1309 investigation. *Sedimentology*, 49(6), 1157-1180. doi:10.1046/j.1365-3091.2002.00482.x

1310 Leclair, S. F., & Bridge, J. S. (2001). Quantitative interpretation of sedimentary structures formed by river
1311 dunes. *Journal of Sedimentary Research*, 71(5), 713-716. doi:1527-1404/01/071-713/\$03.00

1312 Leopold, L. B., & Maddock Jr, T. (1953). The hydraulic geometry of stream channels and some physiographic
1313 implications. *USGS Professional Paper*, 252, 64. doi:10.3133/pp252

1314 Leopold, L. B., & Wolman, M. G. (1957). River channel patterns: Braided, meandering, and straight. *USGS*
1315 *Professional Paper*, 282B, 50. doi:10.3133/pp282B

1316 Li, Y., Bhattacharya, J. P., Ahmed, S., & Garza, D. (2018). Re-evaluating the paleogeography of the river-
1317 dominated and wave-influenced Ferron Notom Delta, Southern Central Utah: an integration of
1318 detailed facies-architecture and paleocurrent analysis. *Journal of Sedimentary Research*, 88(2), 214-
1319 240. doi:10.2110/jsr.2018.9

1320 Lin, W., & Bhattacharya, J. P. (2017). Estimation of source-to-sink mass balance by a fulcrum approach using
1321 channel paleohydrologic parameters of the Cretaceous Dunvegan Formation, Canada. *Journal of*
1322 *Sedimentary Research*, 87(1), 97-116. doi:10.2110/jsr.2017.1

1323 Lynds, R., & Hajek, E. (2006). Conceptual model for predicting mudstone dimensions in sandy braided-river
1324 reservoirs. *AAPG Bulletin*, 90(8), 1273-1288. doi:10.1306/03080605051

1325 Lyster, S. J., Whittaker, A. C., Allison, P. A., Lunt, D. J., & Farnsworth, A. (2020). Predicting sediment discharges
1326 and erosion rates in deep time—examples from the late Cretaceous North American continent. *Basin*
1327 *Research*, 1-27. doi:10.1111/bre.12442

- 1328 Mahon, R. C., & McElroy, B. (2018). Indirect estimation of bedload flux from modern sand-bed rivers and
 1329 ancient fluvial strata. *Geology*, 46(7), 579-582. doi:10.1130/G40161.1
- 1330 McLaurin, B. T., & Steel, R. J. (2007). Architecture and origin of an amalgamated fluvial sheet sand, lower
 1331 Castlegate Formation, Book Cliffs, Utah. *Sedimentary Geology*, 197(3), 291-311.
 1332 doi:10.1016/j.sedgeo.2006.10.005
- 1333 Miall, A. D. (1993). The architecture of fluvial-deltaic sequences in the Upper Mesaverde Group (Upper
 1334 Cretaceous), Book Cliffs, Utah. *Geological Society, London, Special Publications*, 75(1), 305.
 1335 doi:10.1144/GSL.SP.1993.075.01.19
- 1336 Miall, A. D. (1994). Reconstructing fluvial macroform architecture from two-dimensional outcrops; examples
 1337 from the Castlegate Sandstone, Book Cliffs, Utah. *Journal of Sedimentary Research*, 64(2b), 146-158.
 1338 doi:10.1306/D4267F78-2B26-11D7-8648000102C1865D
- 1339 Miall, A. D., & Arush, M. (2001). The Castlegate Sandstone of the Book Cliffs, Utah: Sequence stratigraphy,
 1340 paleogeography, and tectonic controls. *Journal of Sedimentary Research*, 71(4), 537-548.
 1341 doi:10.1306/103000710537
- 1342 Miller, I. M., Johnson, K., Kline, D. E., Nichols, D. J., & Barclay, R. (2013). A Late Campanian Flora from the
 1343 Kaiparowits Formation, southern Utah, and a brief overview of the widely sampled but little-known
 1344 Campanian vegetation of the Western Interior of North America. *At the Top of the Grand Staircase:
 1345 The Late Cretaceous of southern Utah*, 107-131.
- 1346 Milliman, J. D., & Farnsworth, K. L. (2013). *River Discharge to the Coastal Ocean: A Global Synthesis*: Cambridge
 1347 University Press.
- 1348 Mohrig, D., & Smith, J. D. (1996). Predicting the migration rates of subaqueous dunes. *Water Resources
 1349 Research*, 32(10), 3207-3217. doi:10.1029/96WR01129
- 1350 Paola, C., & Borgman, L. (1991). Reconstructing random topography from preserved stratification.
 1351 *Sedimentology*, 38(4), 553-565. doi:10.1111/j.1365-3091.1991.tb01008.x
- 1352 Parker, G. (1976). On the cause and characteristic scales of meandering and braiding in rivers. *Journal of Fluid
 1353 Mechanics*, 76(3), 457-480. doi:10.1017/S0022112076000748
- 1354 Parker, G. (2004). *1D Sediment Transport Morphodynamics with Applications to Rivers and Turbidity Currents*.
- 1355 Parker, L. R. (1976). The paleoecology of the fluvial coal-forming swamps and associated floodplain
 1356 environments in the Blackhawk Formation (Upper Cretaceous) of central Utah. *Brigham Young
 1357 University, Geological Studies*, 22, 99-116.
- 1358 Pederson, J. L., & Tressler, C. (2012). Colorado River long-profile metrics, knickzones and their meaning. *Earth
 1359 and Planetary Science Letters*, 345-348, 171-179. doi:10.1016/j.epsl.2012.06.047
- 1360 Perry, G. D., Duffy, P. B., & Miller, N. L. (1996). An extended data set of river discharges for validation of
 1361 general circulation models. *Journal of Geophysical Research: Atmospheres*, 101(D16), 21339-21349.
 1362 doi:10.1029/96JD00932
- 1363 Pettit, B. S., Blum, M., Pecha, M., McLean, N., Bartschi, N. C., & Saylor, J. E. (2019). Detrital-zircon U-Pb
 1364 paleodrainage reconstruction and geochronology of the Campanian Blackhawk–Castlegate
 1365 succession, Wasatch Plateau and Book Cliffs, Utah, U.S.A. *Journal of Sedimentary Research*, 89(4),
 1366 273-292. doi:10.2110/jsr.2019.18
- 1367 Reesink, A. J. H., & Bridge, J. S. (2007). Influence of superimposed bedforms and flow unsteadiness on
 1368 formation of cross strata in dunes and unit bars. *Sedimentary Geology*, 202(1), 281-296.
 1369 doi:10.1016/j.sedgeo.2007.02.005
- 1370 Reesink, A. J. H., & Bridge, J. S. (2009). Influence of bedform superimposition and flow unsteadiness on the
 1371 formation of cross strata in dunes and unit bars — Part 2, further experiments. *Sedimentary Geology*,
 1372 222(3), 274-300. doi:10.1016/j.sedgeo.2009.09.014
- 1373 Reesink, A. J. H., Van den Berg, J. H., Parsons, D. R., Amsler, M. L., Best, J. L., Hardy, R. J., . . . Szupiany, R. N.
 1374 (2015). Extremes in dune preservation: Controls on the completeness of fluvial deposits. *Earth-
 1375 Science Reviews*, 150, 652-665. doi:10.1016/j.earscirev.2015.09.008

1376 Rittersbacher, A., Howell, J. A., & Buckley, S. J. (2014). Analysis of fluvial architecture in the Blackhawk
1377 Formation, Wasatch Plateau, Utah, U.S.A., using large 3D photorealistic models. *Journal of*
1378 *Sedimentary Research*, 84(2), 72-87. doi:10.2110/jsr.2014.12

1379 Roberts, E. M. (2007). Facies architecture and depositional environments of the Upper Cretaceous Kaiparowits
1380 Formation, southern Utah. *Sedimentary Geology*, 197(3), 207-233. doi:10.1016/j.sedgeo.2006.10.001

1381 Roberts, E. M., Tapanila, L., & Mijal, B. (2008). Taphonomy and sedimentology of storm-generated continental
1382 shell beds: A case example from the Cretaceous Western Interior Basin. *The Journal of Geology*,
1383 116(5), 462-479. doi:10.1086/590134

1384 Roberts, L. N. R., & Kirschbaum, M. A. (1995). Paleogeography and the Late Cretaceous of the Western Interior
1385 of middle North America: coal distribution and sediment accumulation. *U.S. Geological Survey*
1386 *Professional Paper*, 1561, 1-65. doi:10.3133/pp1561

1387 Robinson, R. A. J., & Slingerland, R. L. (1998). Grain-size trends, basin subsidence and sediment supply in the
1388 Campanian Castlegate Sandstone and equivalent conglomerates of Central Utah. *Basin Research*, 10,
1389 109-127.

1390 Romans, B. W., Castelltort, S., Covault, J. A., Fildani, A., & Walsh, J. P. (2016). Environmental signal propagation
1391 in sedimentary systems across timescales. *Earth-Science Reviews*, 153, 7-29.
1392 doi:10.1016/j.earscirev.2015.07.012

1393 Sadler, P. M. (1981). Sediment accumulation rates and the completeness of stratigraphic sections. *The Journal*
1394 *of Geology*, 89, 569-584. doi:10.1086/628623

1395 Schulze, K., Hunger, M., & Döll, P. (2005). Simulating river flow velocity on global scale. *Advances in*
1396 *Geosciences*, 5, 133-136.

1397 Schumm, S. A. (1968). River adjustment to altered hydrologic regimen - Murrumbidgee River and
1398 paleochannels, Australia. *U.S. Geological Survey Professional Paper*, 598, 65. doi:10.3133/pp598

1399 Sewall, J. O., & Fricke, H. C. (2013). Andean-scale highlands in the Late Cretaceous Cordillera of the North
1400 American western margin. *Earth and Planetary Science Letters*, 362, 88-98.
1401 doi:10.1016/j.epsl.2012.12.002

1402 Sharma, S., Bhattacharya, J. P., & Richards, B. (2017). Source-to-sink sediment budget analysis of the
1403 Cretaceous Ferron Sandstone, Utah, U.S.A., using the fulcrum approach. *Journal of Sedimentary*
1404 *Research*, 87(6), 594-608. doi:10.2110/jsr.2017.23

1405 Spieker, E. M. (1946). Late Mesozoic and early Cenozoic history of central Utah. *U.S. Geological Survey*
1406 *Professional Paper*, 205D. doi:10.3133/pp205D

1407 Straub, K. M., Duller, R. A., Foreman, B. Z., & Hajek, E. A. (2020). Buffered, incomplete, and shredded: The
1408 challenges of reading an imperfect stratigraphic record. *Journal of Geophysical Research: Earth*
1409 *Surface*, 125(3), e2019JF005079. doi:10.1029/2019JF005079

1410 Stucky de Quay, G., Kite, E. S., & Mayer, D. P. (2019). Prolonged fluvial activity from channel-fan systems
1411 on Mars. *Journal of Geophysical Research: Planets*, 124(11), 3119-3139. doi:10.1029/2019JE006167

1412 Szwarc, T. S., Johnson, C. L., Stright, L. E., & McFarlane, C. M. (2015). Interactions between axial and transverse
1413 drainage systems in the Late Cretaceous Cordilleran foreland basin: Evidence from detrital zircons in
1414 the Straight Cliffs Formation, southern Utah, USA. *GSA Bulletin*, 127(3-4), 372-392.
1415 doi:10.1130/B31039.1

1416 Trampush, S. M., Huzurbazar, S., & McElroy, B. (2014). Empirical assessment of theory for bankfull
1417 characteristics of alluvial channels. *Water Resources Research*, 50(12), 9211-9220.
1418 doi:10.1002/2014WR015597

1419 Trower, E. J., Ganti, V., Fischer, W. W., & Lamb, M. P. (2018). Erosional surfaces in the Upper Cretaceous
1420 Castlegate Sandstone (Utah, USA): Sequence boundaries or autogenic scour from backwater
1421 hydrodynamics? *Geology*, 46(8), 707-710. doi:10.1130/G40273.1

1422 Tucker, G. E., & Whipple, K. X. (2002). Topographic outcomes predicted by stream erosion models: Sensitivity
1423 analysis and intermodel comparison. *Journal of Geophysical Research: Solid Earth*, 107(B9), ETG 1-1-
1424 ETG 1-16. doi:10.1029/2001JB000162

1425 van Rijn, L. C. (1984a). Sediment transport III: bedforms and alluvial roughness. *Journal of Hydraulic*
1426 *Engineering*, 110(12), 1733-1754. doi:10.1061/(ASCE)0733-9429(1984)110:12(1733)

1427 van Rijn, L. C. (1984b). Sediment transport, part II: Suspended load transport. *Journal of Hydraulic Engineering*,
1428 110(11), 1613-1641. doi:10.1061/(ASCE)0733-9429(1984)110:11(1613)

1429 van Wagoner, J. C. (1995). Sequence Stratigraphy and Marine to Nonmarine Facies Architecture of Foreland
1430 Basin Strata, Book Cliffs, Utah, U.S.A. In J. C. van Wagoner & G. T. Bertram (Eds.), *Sequence*
1431 *Stratigraphy of Foreland Basin Deposits: Outcrop and Subsurface Examples from the Cretaceous of*
1432 *North America* (Vol. 64): American Association of Petroleum Geologists.

1433 Watkins, S. E., Whittaker, A. C., Bell, R. E., McNeill, L. C., Gawthorpe, R. L., Brooke, S. A. S., & Nixon, C. W.
1434 (2018). Are landscapes buffered to high-frequency climate change? A comparison of sediment fluxes
1435 and depositional volumes in the Corinth Rift, central Greece, over the past 130 k.y. *GSA Bulletin*, 131,
1436 372-388. doi:10.1130/B31953.1

1437 Whipple, K. X. (2004). Bedrock rivers and the geomorphology record of active orogens. *Annual Review of Earth*
1438 *and Planetary Sciences*, 32(1), 151-185. doi:10.1146/annurev.earth.32.101802.120356

1439 Whitchurch, A., Carter, A., Sinclair, H., Duller, R., Whittaker, A., & Allen, P. (2011). Sediment routing system
1440 evolution within a diachronously uplifting orogen: Insights from detrital zircon thermochronological
1441 analyses from the South-Central Pyrenees. *American Journal of Science*, 311, 442-482.
1442 doi:10.2475/05.2011.03]

1443 Whittaker, A. C. (2012). How do landscapes record tectonics and climate? *Lithosphere*, 4(2), 160-164.
1444 doi:10.1130/rlf.l003.1

1445 Whittaker, A. C., Duller, R. A., Springett, J., Smithells, R. A., Whitchurch, A. L., & Allen, P. A. (2011). Decoding
1446 downstream trends in stratigraphic grain size as a function of tectonic subsidence and sediment
1447 supply. *GSA Bulletin*, 123(7-8), 1363-1382. doi:10.1130/B30351.1

1448 Wobus, C., Whipple, K. X., Kirby, E., Snyder, N., Johnson, J., Spyropolou, K., . . . Sheehan, D. (2006). Tectonics
1449 from topography: Procedures, promise, and pitfalls. In S. D. Willett, N. Hovius, M. T. Brandon, & D. M.
1450 Fisher (Eds.), *Tectonics, Climate, and Landscape Evolution*: Geological Society of America.

1451 Wobus, C. W., Tucker, G. E., & Anderson, R. S. (2010). Does climate change create distinctive patterns of
1452 landscape incision? *Journal of Geophysical Research: Earth Surface*, 115(F4).
1453 doi:10.1029/2009JF001562

1454 Wolfe, J. A., & Upchurch Jr., G. R. (1987). North American nonmarine climates and vegetation during the Late
1455 Cretaceous. *Palaeogeography, Palaeoclimatology, Palaeoecology*, 61(Supplement C), 33-77.
1456 doi:10.1016/0031-0182(87)90040-X

1457 Wolman, M. G. (1954). A method of sampling coarse river-bed material. *Eos Transactions American*
1458 *Geophysical Union*, 35(6), 951-956. doi:10.1029/TR035i006p00951

1459 Wright, S., & Parker, G. (2004). Flow resistance and suspended load in sand-bed rivers: Simplified stratification
1460 model. *Journal of Hydraulic Engineering*, 130(8), 796-805. doi:10.1061/(ASCE)0733-
1461 9429(2004)130:8(796)

1462 Yalin, M. S. (1964). Geometrical properties of sand waves. *Journal of the Hydraulics Division*, 90(5), 105-119.

1463 Yoshida, S., Willis, A., & Miall, A. D. (1996). Tectonic control of nested sequence architecture in the Castlegate
1464 Sandstone (Upper Cretaceous), Book Cliffs, Utah. *Journal of Sedimentary Research*, 66(4), 737-748.

1465 Zhang, J., Covault, J., Pyrcz, M., Sharman, G., Carvajal, C., & Milliken, K. (2018). Quantifying sediment supply to
1466 continental margins: Application to the Paleogene Wilcox Group, Gulf of Mexico. *AAPG Bulletin*,
1467 102(9), 1685-1702. doi:10.1306/01081817308

1468 Zhisheng, A., Kutzbach, J. E., Prell, W. L., & Porter, S. C. (2001). Evolution of Asian monsoons and phased uplift
1469 of the Himalaya–Tibetan plateau since Late Miocene times. *Nature*, 411(6833), 62-66.
1470 doi:10.1038/35075035

1471

1472

1473 **Supplementary Information for: *Reconstructing the morphologies and hydrodynamics of ancient***
1474 ***rivers from source to sink: Cretaceous Western Interior Basin, Utah, USA***

1475 **Sinéad J. Lyster^{1*}**, Alexander C. Whittaker¹, Gary J. Hampson¹, Elizabeth A. Hajek², Peter A. Allison¹
1476 and Bailey A. Lathrop¹

1477 ¹ Department of Earth Science and Engineering, Imperial College London, London, UK.

1478 ² Department of Geosciences, The Pennsylvania State University, Pennsylvania, USA.

1479 *s.lyster17@imperial.ac.uk

1480 **Contents:**

1481 **S1. Variables list**

1482 **S2. Field localities**

1483 **S3. Regional correlation – further information**

1484 **S4. Field data**

1485 **S5. Grain size sample sufficiency**

1486 **S6. Secondary field data**

1487 **S7. Goodness of fits on palaeoslope profiles inc. resolved steepness indexes**

1488 **S8. Additional results**

1489

1490 **S1. Variables list**

1491 Here we present a list of all variables assigned and used in this study (see Methods section):

1492	A_x	Upstream catchment area [m^2]
1493	C_1	Constant in Equation 9 associated with grain sphericity and roundness [-]
1494	C_2	Constant in Equation 9 associated with grain sphericity and roundness [-]
1495	c_H	Hack coefficient [-]
1496	D_x	xth percentile of the grain size distribution [m]
1497	Fr	Froude number [-]
1498	g	Acceleration due to gravity [m/s^2]
1499	H	Median formative flow depth [m]
1500	h	Hack exponent [m]
1501	h_d	Mean original bedform (i.e. dune) height [m]
1502	h_{xs}	Mean cross-set height [m]
1503	k	Erodibility constant [-]
1504	k_s	Steepness index [$m^{0.8}$ or m^1 or $m^{1.2}$]
1505	L_x	Upstream catchment length [m]
1506	n	Manning's constant [$s/m^{1/3}$]
1507	Q	Water discharge [m^2/s or m^3/s]
1508	R	Dimensionless submerged specific gravity of sediment in water [-]
1509	Re_p	Particle Reynold's number [-]
1510	S	Slope [-]
1511	U	Flow velocity [m/s]
1512	u_*	Bed shear velocity [m/s]

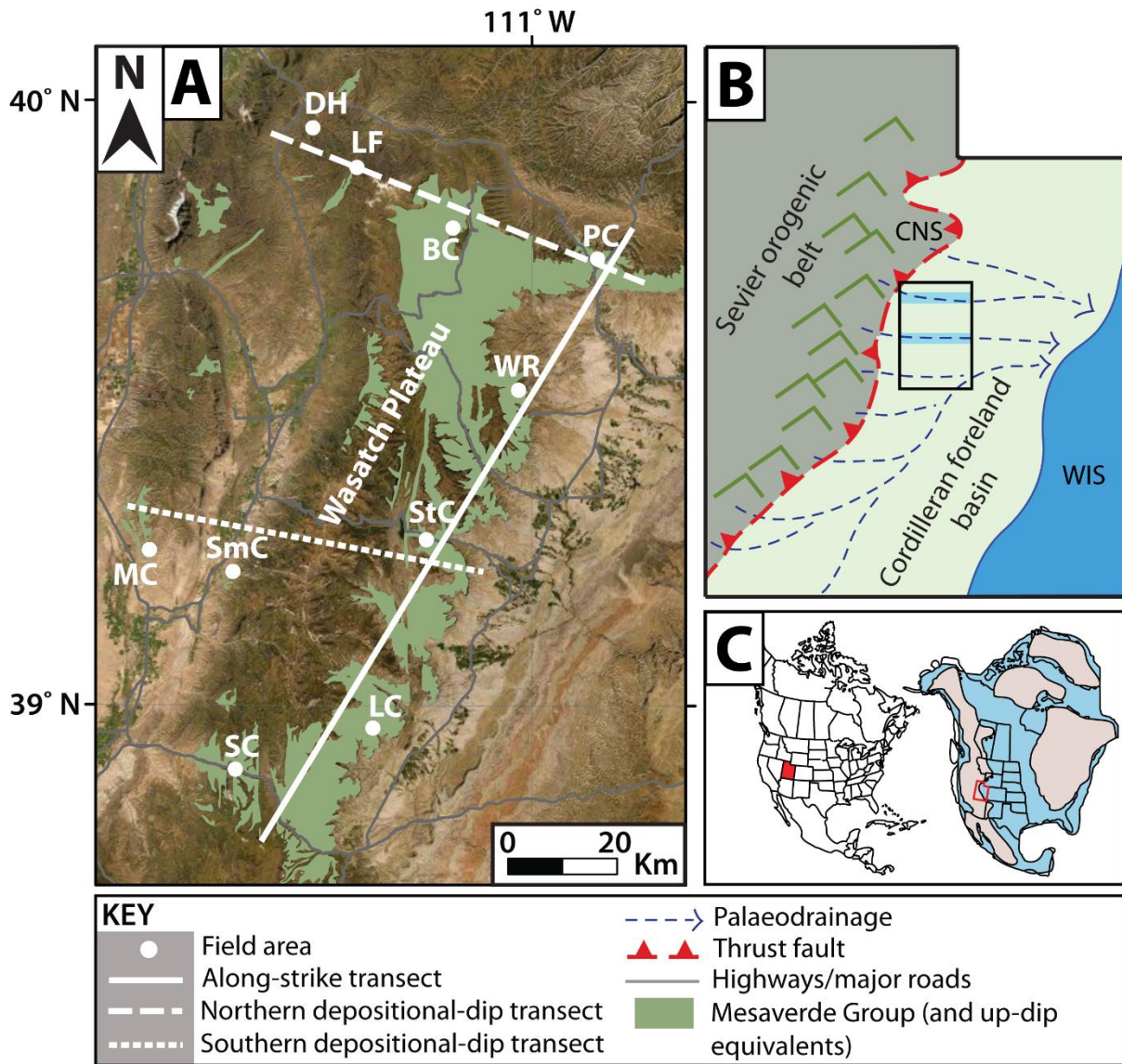
1513	ν	Kinematic viscosity of water [m^2/s]
1514	W	Channel width [m]
1515	w_s	Sediment settling velocity [m/s]
1516	Z	Rouse number [-]
1517	α_0	Constant in Equation 4 [-]
1518	α_1	Constant in Equation 4 [-]
1519	α_2	Constant in Equation 4 [-]
1520	β	Eddy viscosity and diffusivity constant [-]
1521	θ	Concavity index [-]
1522	κ	von Karman constant [-]
1523	λ	Bedform wavelength [m]
1524	ρ	Fluid density [kg/m^3]
1525	τ^*	Dimensionless bed shear stress, Shields stress [-]
1526	τ_b	Bed shear stress [$\text{kg}/\text{m}/\text{s}^2$]
1527		

1528 **S2. Field localities**

1529 Palaeohydrological data were collected at each field site, as described in the Methods. These data
 1530 centred on grain-size and cross-set measurements, but additionally included measurement of channel
 1531 geometries and palaeocurrent indicators.

1532 Field localities were grouped spatially, typically by the canyon in which they were located. From north-
 1533 northeast to south-southwest, localities were grouped into 5 field areas along a depositional strike
 1534 transect: Price Canyon, Wattis Road, Straight Canyon (including Joe's Valley Reservoir), Link Canyon
 1535 and Salina Canyon (Fig. S1; reproduced from Fig. 1 in the main text). These 5 field areas represent 5
 1536 parallel transverse fluvial systems draining the Sevier orogenic front. Further data were collected
 1537 along two up-dip to down-dip depositional-dip transects, to encompass an upstream to downstream
 1538 element for 2 of these palaeorivers (Fig. S1). The northern depositional-dip transect included field
 1539 localities that were grouped as Dry Hollow, Lake Fork, Bear Canyon, and terminating at Price Canyon.
 1540 Meanwhile, the southern depositional-dip transect included field localities that were grouped as
 1541 Mellor Canyon, Sixmile Canyon, and terminating at Straight Canyon. These transects are in line with
 1542 those implemented in previous work, both along-strike (Hampson et al., 2012; Hampson et al., 2013;
 1543 Flood & Hampson, 2014, 2015; Chamberlin & Hajek, 2019) and up-dip to down-dip (Robinson &
 1544 Slingerland, 1998; Horton et al., 2004; Aschoff & Steel, 2011b, 2011a).

1545 For each field area, localities were typically within 5 km of one another. There exist a few exceptions
 1546 to this, in which localities were slightly more spread out (<10 km). These field areas were characterised
 1547 by post-depositional extensional faulting and so we encompassed localities that were either along-
 1548 depositional strike, or further down-dip on downthrown fault blocks — when restored, it is
 1549 anticipated that these field localities would have been in close proximity. All field localities are detailed
 1550 in Table S1 and have been subdivided by both field area and stratigraphic interval. It is important to
 1551 note that some field localities are duplicated across stratigraphic intervals — this is where data have
 1552 time-averaged across stratigraphic intervals.



1553

1554 **Figure S1:** Study area showing key localities mentioned in the supplement, reproduced from Figure 1
 1555 in the main manuscript. Part A) Field areas in central Utah, USA, which include Bear Canyon (BC), Dry
 1556 Hollow (DH), Lake Fork (LF), Link Canyon (LC), Mellor Canyon (MC), Price Canyon (PC), Salina Canyon
 1557 (SC), Sixmile Canyon (SmC), Straight Canyon (StC) and Wattis Road (WR). The solid white line indicates the
 1558 along-depositional-strike transect defined in this study, the dashed white line indicates the
 1559 northern depositional-dip transect defined in this study, and the dotted white line indicates the
 1560 southern depositional-dip transect defined in this study. Part B) A conceptual diagram of Utah
 1561 palaeogeography and palaeodrainage in the Campanian (Late Cretaceous). Likely configurations of
 1562 drainage toward the Western Interior Seaway (WIS) are indicated by dashed blue lines. CNS =
 1563 Charleston–Nebo Salient. The black outlined box indicates the study area (i.e. part A), and the two
 1564 highlighted drainage routes (shaded blue) represent the northern and southern depositional-dip
 1565 transects defined in this study (see Part A). Part C) The location of Utah relative to the modern North
 1566 American continent (left) and the Late Cretaceous North American continent (right), which features
 1567 the Western Interior Seaway (blue). Utah is highlighted as a red box.

1568

1569 **Table S1:** Field localities visited in this study, for each field area (e.g. Price Canyon, Wattis Road, etc).
 1570 Field localities are further subdivided into their respective stratigraphic intervals (1–7). 1 = lower
 1571 Blackhawk Formation; 2 = middle Blackhawk Formation; 3 = upper Blackhawk Formation; 4 = lower
 1572 Castlegate Sandstone; 5 = middle Castlegate Sandstone; 6 = upper Castlegate Sandstone (Bluecastle
 1573 Tongue); 7 = (lowermost) Price River Formation. It is important to note that some field localities are
 1574 duplicated across stratigraphic intervals — this is where data have been time-averaged across
 1575 stratigraphic intervals. Where ‘N/A’ is reported, this is the absence of data (typically due to lack of
 1576 access or lack of outcrop).

Location and stratigraphic interval		Field sites	Elevation, m (±3–4)
Bear Canyon	Lower Blackhawk Formation (1)	N/A	N/A
	Middle Blackhawk Formation (2)	N39 49 53.4, W111 08 32.8	2383
		N39 46 59.3, W111 10 37.8	2325
	Upper Blackhawk Formation (3)	N39 47 31.9, W111 11 33.6	2347
		N39 47 57.4, W111 12 23.0	2373
		N39 48 04.1, W111 12 37.0	2416
		N39 48 00.5, W111 12 31.9	2371
	Lower Castlegate Sandstone (4)	N39 48 05.4, W111 12 27.5	2439
		N39 48 07.6, W111 12 35.6	2426
	Middle Castlegate Sandstone (5)	N39 50 18.2, W111 11 31.8	2263
		N39 50 10.4, W111 11 16.6	2261
	Upper Castlegate Sandstone (6)	N39 50 17.6, W111 11 42.6	2282
		N39 49 52.7, W111 08 30.5	2341
		N39 48 12.7, W111 12 33.3	2495
N39 48 09.8, W111 12 30.1		2485	
Price River Formation (7)	N39 51 06.7, W111 11 01.7	2200	
	N39 50 33.8, W111 11 17.0	2236	
	N39 49 53.4, W111 08 32.8	2383	
Dry Hollow	Lower Blackhawk Formation (1)	N/A	N/A
	Middle Blackhawk Formation (2)	N39 57 35.2, W111 28 42.6	1769
		N3957 35.2, W111 28 43.5	1773
	Upper Blackhawk Formation (3)	N39 57 35.2, W111 28 42.6	1769
		N3957 35.2, W111 28 43.5	1773
	Lower Castlegate Sandstone (4)	N39 57 34.8, W111 28 40.6	1764
	Middle Castlegate Sandstone (5)	N39 57 33.0, W111 23 38.0	1730
		N39 57 33.8, W111 28 37.8	1756
Upper Castlegate Sandstone (6)	N39 57 33.0, W111 23 38.0	1730	
	N39 57 33.8, W111 28 37.8	1756	
Price River Formation (7)	N/A	N/A	
Lake Fork	Lower Blackhawk Formation (1)	N/A	N/A
	Middle Blackhawk Formation (2)	N/A	N/A
	Upper Blackhawk Formation (3)	N/A	N/A
	Lower Castlegate Sandstone (4)	N39 53 16.1, W111 23 49.5	2058

	Middle Castlegate Sandstone (5)	N39 53 36.6, W111 23 27.7	2063
		N39 53 29.7, W111 23 06.8	2115
	Upper Castlegate Sandstone (6)	N39 53 36.6, W111 23 27.7	2063
		N39 53 29.7, W111 23 06.8	2115
	Price River Formation (7)	N39 53 23.0, W111 22 59.1	2131
		N39 53 21.3, W111 22 57.6	2170
Link Canyon	Lower Blackhawk Formation (1)	N38 57 42.1, W111 19 57.4	2363
		N38 57 39.7, W111 19 53.9	2383
		N38 57 41.4, W111 19 53.0	2398
	Middle Blackhawk Formation (2)	N38 57 44.3, W111 19 53.8	2421
		N38 57 48.4, W111 19 53.9	2473
	Upper Blackhawk Formation (3)	N38 57 58.3, W111 19 57.3	2538
		N38 57 52.8, W111 19 55.8	2509
		N38 57 51.4, W111 19 55.0	2500
	Lower Castlegate Sandstone (4)	N38 58 05.9, W111 19 56.6	2572
	Middle Castlegate Sandstone (5)	N38 58 08.0, W111 19 55.8	2584
	Upper Castlegate Sandstone (6)	N38 58 10.6, W111 19 54.2	2600
	Price River Formation (7)	N38 58 15.8, W111 20 15.0	2643
Mellor Canyon	Lower Blackhawk Formation (1)	N39 15 07.5, W111 49 04.0	1751
		N39 15 05.2, W111 49 04.8	1732
		N39 15 03.3, W111 49 06.6	1721
		N39 15 02.3, W111 49 07.3	1715
		N39 15 00.7, W111 49 05.8	1711
		N39 15 00.0, W111 49 09.8	1701
		N39 14 59.6, W111 49 15.3	1717
		N39 14 59.8, W111 49 23.6	1691
		N39 14 58.0, W111 49 25.0	1683
	Middle Blackhawk Formation (2)	N39 15 07.5, W111 49 04.0	1751
		N39 15 05.2, W111 49 04.8	1732
		N39 15 03.3, W111 49 06.6	1721
		N39 15 02.3, W111 49 07.3	1715
		N39 15 00.7, W111 49 05.8	1711
		N39 15 00.0, W111 49 09.8	1701
		N39 14 59.6, W111 49 15.3	1717
		N39 14 59.8, W111 49 23.6	1691
		N39 14 58.0, W111 49 25.0	1683
	Upper Blackhawk Formation (3)	N39 15 07.5, W111 49 04.0	1751
		N39 15 05.2, W111 49 04.8	1732
		N39 15 03.3, W111 49 06.6	1721
		N39 15 02.3, W111 49 07.3	1715
		N39 15 00.7, W111 49 05.8	1711
		N39 15 00.0, W111 49 09.8	1701
		N39 14 59.6, W111 49 15.3	1717
		N39 14 59.8, W111 49 23.6	1691

		N39 14 58.0, W111 49 25.0	1683
	Lower Castlegate Sandstone (4)	N39 15 11.4, W111 49 00.9	1809
		N39 15 09.8, W111 49 01.6	1784
		N39 15 08.8, W111 49 01.9	1770
	Middle Castlegate Sandstone (5)	N39 15 11.4, W111 49 00.9	1809
		N39 15 09.8, W111 49 01.6	1784
		N39 15 08.8, W111 49 01.9	1770
	Upper Castlegate Sandstone (6)	N39 15 11.4, W111 49 00.9	1809
		N39 15 09.8, W111 49 01.6	1784
		N39 15 08.8, W111 49 01.9	1770
	Price River Formation (7)	N39 15 11.4, W111 49 00.9	1809
		N39 15 09.8, W111 49 01.6	1784
		N39 15 08.8, W111 49 01.9	1770
Price Canyon	Lower Blackhawk Formation (1)	N/A	N/A
	Middle Blackhawk Formation (2)	N/A	N/A
	Upper Blackhawk Formation (3)	N39 44 11.0, W110 50 47.7	1932
		N39 44 08.4, W110 50 46.9	1947
	Lower Castlegate Sandstone (4)	N39 45 05.1, W110 53 10.3	1920
		N39 44 48.5, W110 49 58.1	1969
		N39 44 52.6, W110 49 55.4	1983
	Middle Castlegate Sandstone (5)	N39 45 01.3, W110 49 43.5	2000
		N39 45 03.0, W110 49 40.6	1999
	Upper Castlegate Sandstone (6)	N39 45 10.5, W110 49 35.8	2008
	N39 45 12.0, W110 49 34.8	2003	
	Price River Formation (7)	N39 46 18.3, W110 48 12.1	2115
		N39 45 58.8, W110 48 30.1	2095
		N39 45 47.1, W110 48 41.6	2044
		N39 45 32.1, W110 49 02.0	2035
Salina Canyon	Lower Blackhawk Formation (1)	N38 54 00.8, W111 39 53.8	1861
	Middle Blackhawk Formation (2)	N38 53 51.5, W111 39 02.3	1885
	Upper Blackhawk Formation (3)	N38 54 29.6, W111 41 46.8	1802
		N38 54 13.8, W111 39 05.9	1926
	Lower Castlegate Sandstone (4)	N38 54 52.9, W111 38 06.5	2036
		N38 54 52.3, W111 38 08.7	2017
	Middle Castlegate Sandstone (5)	N38 54 50.6, W111 38 18.1	2009
		N38 54 52.6, W111 38 20.2	2030
		N38 54 53.7, W111 38 ~20.2	2035
		N38 54 33.0, W111 42 32.7	1779
Upper Castlegate Sandstone (6)	N38 54 57.1, W111 38 20.3	2076	
	N38 54 59.4, W111 38 13.1	2111	
	Price River Formation (7)	N38 55 04.1, W111 38 15.7	2152
Sixmile Canyon	Lower Blackhawk Formation (1)	N39 12 43.1, W111 38 55.0	1876
		N39 12 25.4, W111 39 12.5	1860
	Middle Blackhawk Formation (2)	N39 12 43.1, W111 38 55.0	1876

		N39 12 25.4, W111 39 12.5	1860	
	Upper Blackhawk Formation (3)	N39 12 43.1, W111 38 55.0	1876	
		N39 12 25.4, W111 39 12.5	1860	
	Lower Castlegate Sandstone (4)	N39 12 51.6, W111 37 32.9	1967	
		N39 12 51.6, W111 37 54.7	1931	
		N39 12 44.5, W111 38 10.4	1892	
		N39 12 44.9, W111 38 13.8	1923	
		N39 12 49.6, W111 37 40.1	1952	
	Middle Castlegate Sandstone (5)	N39 12 51.6, W111 37 32.9	1967	
		N39 12 51.6, W111 37 54.7	1931	
		N39 12 44.5, W111 38 10.4	1892	
		N39 12 44.9, W111 38 13.8	1923	
		N39 12 49.6, W111 37 40.1	1952	
	Upper Castlegate Sandstone (6)	N39 12 51.6, W111 37 32.9	1967	
		N39 12 51.6, W111 37 54.7	1931	
		N39 12 44.5, W111 38 10.4	1892	
		N39 12 44.9, W111 38 13.8	1923	
		N39 12 49.6, W111 37 40.1	1952	
	Price River Formation (7)	N39 12 46.4, W111 36 57.8	1995	
Straight Canyon	Lower Blackhawk Formation (1)	N39 16 56.6, W111 13 58.0	2027	
		N39 16 46.2, W111 13 41.9	2010	
		N39 16 29.1, W111 13 11.9	1996	
	Middle Blackhawk Formation (2)	N39 17 16.2, W111 14 37.5	2047	
		N39 17 15.7, W111 14 30.4	2043	
		N39 17 05.7, W111 14 10.5	2037	
	Upper Blackhawk Formation (3)	N39 17 36.5, W111 16 16.7	2146	
		N39 17 19.3, W111 16 00.0	2129	
		N39 17 20.9, W111 15 19.8	2102	
	Lower Castlegate Sandstone (4)	N39 17 51.9, W111 16 18.0	2161	
	Middle Castlegate Sandstone (5)	N39 18 28.6, W111 16 13.2	2181	
	Upper Castlegate Sandstone (6)	N39 18 55.2, W111 16 06.2	2238	
		Price River Formation (7)	N/A	
	Wattis Road	Lower Blackhawk Formation (1)	N39 31 45.5, W111 02 16.0	2577
Middle Blackhawk Formation (2)		N39 31 11.9, W111 01 56.9	2692	
		N39 31 19.8, W111 01 58.4	2655	
Upper Blackhawk Formation (3)		N39 31 20.7, W111 02 37.2	2798	
		N39 31 14.3, W111 02 13.8	2765	
Lower Castlegate Sandstone (4)		N39 31 28.6, W111 02 44.9	2844	
Middle Castlegate Sandstone (5)		N39 31 31.7, W111 02 50.6	2877	
		N39 31 30.2, W111 02 46.4	2861	
Upper Castlegate Sandstone (6)		N39 31 33.5, W111 02 53.2	2889	
	Price River Formation (7)	N/A		

1577

1578

1579 **S3. Regional correlation**

1580 In addition to grouping field localities in space, localities were also grouped in time. In this study 7
1581 stratigraphic intervals were defined, which were used to reconstruct the palaeohydrological evolution
1582 of ancient rivers draining the Sevier orogenic front. These intervals are all Campanian in age, which
1583 spanned a duration of 11.5 Myr (83.6 ± 0.2 to 72.1 ± 0.2 Ma) in the Late Cretaceous. These 7 intervals
1584 are defined as: 1 = lower Blackhawk Formation; 2 = middle Blackhawk Formation; 3 = upper Blackhawk
1585 Formation; 4 = lower Castlegate Sandstone; 5 = middle Castlegate Sandstone; 6 = upper Castlegate
1586 Sandstone (Bluecastle Tongue); 7 = (lowermost) Price River Formation. These intervals are referred to
1587 in the Results and in Fig. 2 of the main text. It is important to note that these stratigraphic intervals
1588 are not of equal duration — age constraints across these intervals are derived from correlation with
1589 ammonite biozones in the down-dip Mancos Shale, which have been age-constrained by radiometric
1590 dating of volcanic ash beds (Gill & Hail Jr, 1975; Fouch et al., 1983; Cobban et al., 2006) — see recent
1591 review by Seymour and Fielding (2013). The lowermost Blackhawk Formation is correlated with the
1592 *Scaphites hippocrepis II* zone (83.5 ± 0.7 – 81.86 ± 0.36 Ma), the middle Blackhawk Formation with the
1593 *Baculites obtusus* zone (80.58 ± 0.55 Ma), and the top of the Blackhawk Formation with the *Baculites*
1594 *asperiformis* zone (79 Ma). The lower and middle Castlegate Sandstone are correlated with the
1595 *Baculites perplexus*, *Baculites scotti* ($75.84\pm 0.26/75.56\pm 0.11$ Ma), *Didymoceras nebrascense* and
1596 *Didymoceras stevensoni* (75.19 ± 0.28 Ma) zones. The upper Castlegate Sandstone is correlated with
1597 the *Exiteloceras jenneyi* zone (75.08 ± 0.11 Ma) and, finally, the Price River Formation is correlated with
1598 the *Didymoceras cheyennense* and *Baculites jenseni* zones (74.67 ± 0.15 – 71.98 ± 0.31 Ma) (Fouch et al.,
1599 1983; Cobban et al., 2006).

1600 *Down-dip: Eastern Wasatch Plateau*

1601 Along the eastern front of the Wasatch Plateau (Fig. S1), it is straightforward to assign field localities
1602 to their appropriate stratigraphic intervals by facies associations, following extensive work that has
1603 been undertaken in this region (Lawton, 1983, 1986b; Miall, 1994; van Wagoner, 1995; Yoshida et al.,
1604 1996; Miall & Arush, 2001; Lawton et al., 2003; Adams & Bhattacharya, 2005; Hampson et al., 2012;
1605 Hampson et al., 2013; Flood & Hampson, 2014; Hampson et al., 2014; Flood & Hampson, 2015).

1606 The lower–middle Campanian Blackhawk Formation, (Hampson, 2010; Hampson et al., 2012)
1607 represents deposition on coastal plains behind wave-dominated deltaic shorelines which, up-section,
1608 pass landward into alluvial and fluvial plains (Hampson et al., 2012; Hampson et al., 2013). The size
1609 and abundance of channelized fluvial sandstone bodies (deposited by both single- and multi-thread
1610 rivers) increase from base to top of the Blackhawk Formation (Adams & Bhattacharya, 2005; Hampson
1611 et al., 2012; Hampson et al., 2013; Flood & Hampson, 2015). The Blackhawk Formation comprises
1612 intervals 1, 2 and 3 in this study, i.e. the lower, middle and upper Blackhawk Formation. The Blackhawk
1613 Formation is slightly challenging to subdivide into stratigraphic intervals as it is typically
1614 undifferentiated along the eastern Wasatch Plateau front (with the exception of Price Canyon)
1615 (Hampson et al., 2012; Hampson et al., 2013) — this is, in part, because the upper half of the
1616 Blackhawk Formation lacks mappable coal zones or other stratigraphic markers along the Wasatch
1617 Plateau front (Hampson et al., 2012; Hampson et al., 2013). This study follows Flood and Hampson
1618 (2014, 2015) in subdividing the Blackhawk Formation into the lower, middle, and upper Blackhawk
1619 Formation. While these divisions may not be exact, given variation in outcrop exposure at Price
1620 Canyon, Wattis Road, Straight Canyon, Link Canyon and Salina Canyon, as well as north–south
1621 variation in stratigraphic thickness, they are appropriate for the temporal and spatial scales

1622 considered here. At Price Canyon, only the Desert Member of the Blackhawk Formation is fluvial, and
1623 so data were only collected from this member, which were then assigned to the upper Blackhawk
1624 Formation stratigraphic interval. For Wattis Road, Straight Canyon, Link Canyon, and Salina Canyon,
1625 field localities were assigned to the lower, middle and upper Blackhawk Formation, following
1626 Hampson et al. (2012); Hampson et al. (2013); Flood and Hampson (2014, 2015), based on (1)
1627 adjacency to the contact with the overlying Castlegate Sandstone or underlying Star Point Sandstone;
1628 (2) where the outcrop was positioned, stratigraphically, within the entire stratigraphic thickness of the
1629 Blackhawk Formation at the field area in question; (3) architectural and facies observations — up-
1630 section the Blackhawk Formation is more palaeo-landward and preserves an increase in the size and
1631 abundance of channelized fluvial sandstone bodies; (4) presence and abundance of coal zones, which
1632 are associated with the lower and middle Blackhawk Formation, but are most abundant in the lower
1633 Blackhawk Formation (Flood & Hampson, 2014, 2015).

1634 The middle–upper Campanian Castlegate Sandstone is situated atop the Blackhawk Formation and is
1635 an extensive and easily recognisable cliff-forming deposit — the basal contact separates braided fluvial
1636 deposits from underlying coastal plain deposits of the Blackhawk Formation (van Wagoner, 1995;
1637 Yoshida et al., 1996). In this study the Castlegate Sandstone comprises intervals 4, 5 and 6, i.e. the
1638 lower, middle and upper Castlegate Sandstone respectively. The lower and upper Castlegate
1639 Sandstone both comprise amalgamated braided fluvial channel-belt deposits, whereas the middle
1640 Castlegate Sandstone comprises less amalgamated, more meandering, fluvial channel-belt deposits
1641 with interbedded mudstones (Fouch et al., 1983; Lawton, 1986b; Miall, 1994; Yoshida et al., 1996;
1642 Miall & Arush, 2001).

1643 The ledge-forming upper Campanian Price River Formation conformably overlies the Castlegate
1644 Sandstone and is interval 7 in this study. It is recognised by transition from amalgamated fluvial
1645 channel-belt deposits of the upper Castlegate Sandstone to large channelized sandstone bodies (~10–
1646 30m thick) with interbedded siltstones and mudstones — channelized sandstone bodies form ~75%
1647 of the formation (Lawton, 1983, 1986b). This transition is also recognised by a break in slope. Data
1648 were collected for channelized sandstone bodies of the lowermost Price River Formation (where
1649 accessible) atop the contact with the underlying upper Castlegate Sandstone.

1650 *Up-dip: Western Wasatch Plateau*

1651 Importantly, in this study data were additionally collected along two up-dip to down-dip transects, to
1652 capture upstream to downstream trends for 2 of the 5 transverse fluvial systems. This requires
1653 correlation of the 7 aforementioned stratigraphic intervals (along the eastern Wasatch Plateau front)
1654 with up-dip strata on the western and central Wasatch Plateau. Up-dip field sites along the northern
1655 depositional dip transect include Dry Hollow, Lake Fork, and Bear Canyon, meanwhile up-dip field sites
1656 along the southern depositional-dip transect include Mellor Canyon and Sixmile Canyon. These
1657 depositional-dip transects follow those of Robinson and Slingerland (1998); Horton et al. (2004). Bear
1658 Canyon can be excluded from subsequent considerations as it has been mapped using Blackhawk–
1659 Castlegate–Price River nomenclature.

1660 Up-dip, on the western Wasatch Plateau, correlative strata include more proximal sediments of the
1661 Indianola Group and Price River Formation, which is now known to not be time-equivalent with the
1662 down-dip Price River Formation exposed near Price, Utah (Robinson & Slingerland, 1998; Horton et
1663 al., 2004; Aschoff & Steel, 2011b, 2011a). Here, to avoid confusion, up-dip strata are referred to as the

1664 Price River Conglomerate, following Aschoff and Steel (2011b, 2011a). It is to be noted that the Price
1665 River Conglomerate has elsewhere been referred to as the Conglomerate of Thistle (Valora, 2010).
1666 The detail of up-dip correlations is limited by poor exposure on the Wasatch Plateau and difficulty in
1667 dating conglomerates. Nevertheless, work by Robinson and Slingerland (1998) successfully used
1668 palynology to establish correlation of the lower Castlegate Sandstone with up-dip conglomerates
1669 exposed across a variety of localities on the Wasatch Plateau (Fig. 2). Correlations were corroborated
1670 by field observations, e.g. correlation of a white, quartzite-dominated, cobble–boulder conglomerate
1671 in the Charleston–Nebo Salient of the Sevier thrust belt with the Castlegate–Price River succession in
1672 the Book Cliffs to the east, which can be traced in seismic reflection data (Robinson & Slingerland,
1673 1998; Horton et al., 2004). These works were used in the field to establish correlations.

1674 The up-dip upper Sixmile Canyon Formation of the Indianola Group is predominantly characterised by
1675 synorogenic gravel–sand fluvial facies, spanning polymictic fluvial conglomerates to medium–coarse-
1676 grained sandstones (Lawton, 1982, 1986a, 1986b). The upper Sixmile Canyon Formation is time-
1677 correlative with the Blackhawk Formation (Lawton, 1982; Fouch et al., 1983; Lawton, 1986b), and
1678 therefore encompasses intervals 1, 2, and 3 in this study. Meanwhile, the up-dip Price River
1679 Conglomerate is characterised by quartzite-dominated synorogenic conglomerates wherein debris
1680 flow facies interact with gravel–sand fluvial facies (Robinson & Slingerland, 1998; Aschoff & Steel,
1681 2011b, 2011a). The Price River Conglomerate is time-correlative with the down-dip lower, middle, and
1682 upper Castlegate Sandstone, and Price River Formation (Robinson & Slingerland, 1998; Horton et al.,
1683 2004), and therefore encompasses intervals 4, 5, 6 and 7 in this study.

1684 Given uncertainties in age constraints, a conservative approach to correlation is taken in this study.
1685 Up-dip, at Dry Hollow, Lake Fork, Mellor Canyon, and Sixmile Canyon, the upper Sixmile Canyon
1686 Formation of the Indianola Group (intervals 1–3) is time-averaged, and the entire Price River
1687 Conglomerate (intervals 4–7) is also time-averaged. It can be said that, up-dip, time-averaging across
1688 intervals 1–3 and 4–7, respectively, may lead to loss of temporal signal. However, exceptions were
1689 made to time-averaging where field localities were known to be situated at the top of the upper
1690 Sixmile Canyon Formation or at the top/base of the Price River Conglomerate. Currently, it is not
1691 possible to generate time-correlations at higher resolution. Nevertheless, the observation was made
1692 that within the upper Sixmile Canyon Formation and Price River Conglomerate, respectively, median
1693 grain-sizes and mean cross-set heights for each grain-size facies were generally similar throughout
1694 sections. The main impact of time-averaging across sections was therefore that our results do not
1695 account for how the proportions of different grain-size facies change up-section.

1696 In the northern transect, for up-dip field areas of Dry Hollow and Lake Fork, assignment of field
1697 localities to their appropriate stratigraphic intervals (as per the previous paragraph) is simple as
1698 regional mapping has differentiated the Indianola Group into its respective members, including the
1699 Sixmile Canyon Formation, and has also mapped the Price River Conglomerate (though it is mapped
1700 with its alternative name, i.e. Conglomerate of Thistle). However, in the southern transect, for up-dip
1701 field areas of Mellor Canyon and Sixmile Canyon, assignment is less simple as regional mapping is older
1702 and predates recent advances in regional correlation (c.f. Robinson & Slingerland, 1998; Horton et al.,
1703 2004; Aschoff & Steel, 2011b, 2011a). In Sixmile Canyon, the Indianola Group is differentiated into its
1704 respective members. However, what would be Price River Conglomerate has here been mapped as
1705 the Price River Formation — but it is now known that the up-dip Price River Formation on the western
1706 Wasatch Plateau is time-correlative with *both* the Castlegate Sandstone and Price River Formation on

1707 the eastern Wasatch Plateau (Robinson & Slingerland, 1998; Horton et al., 2004; Aschoff & Steel,
1708 2011b, 2011a). This is taken into account accordingly and considered to be Price River Conglomerate.
1709 Secondly, in Mellor Canyon, the entire stratigraphy is undifferentiated — it is all mapped as
1710 undifferentiated Indianola Group sediments, and is capped unconformably by the North Horn
1711 Formation. As such, in this study the stratigraphy in Mellor Canyon was newly logged so that
1712 stratigraphy could be appropriately assigned, (expanding on work by Robinson and Slingerland (1998))
1713 (Fig. S2). Observations of up-dip, more proximal sediments in the northern depositional-dip transect
1714 (i.e. at Dry Hollow) were extrapolated to Mellor Canyon. These included observations that the Price
1715 River Conglomerate is characterised by quartzite-dominated synorogenic conglomerates wherein
1716 debris flow facies interact with gravel–sand fluvial facies (Robinson & Slingerland, 1998; Aschoff &
1717 Steel, 2011b, 2011a), and the upper Sixmile Canyon Formation of the Indianola Group is
1718 predominantly characterised by synorogenic gravel–sand fluvial facies spanning polymictic
1719 conglomerates to medium–coarse-grained sands (Lawton, 1982, 1986a, 1986b). In logging the Mellor
1720 Canyon section, quartzite-dominated debris conglomerates with interspersed gravel–sand
1721 channelized bodies were successfully identified, and then classified as Price River Conglomerate (Fig.
1722 S2). In addition, the more polymictic fluvial conglomerates and channelized sandstone bodies, which
1723 can be likened to the upper Sixmile Canyon Formation, were also successfully identified (Fig. S2). It is
1724 unclear whether logged strata encompass the entire Sixmile Canyon Formation, or just the uppermost
1725 Sixmile Canyon Formation. However the entire Sixmile Canyon Formation at Sixmile Canyon has a
1726 stratigraphic thickness of over 1.2 km, whereas at Mellor Canyon our logging is for the uppermost 240
1727 m of Sixmile Canyon Formation — it is therefore reasonable to assign these sediments to the upper
1728 Sixmile Canyon Formation (Fig. S2).

1729

1730 [SUPPLEMENTARY FIGURE 2 ATTACHED AS PDF “LYSTER_ETAL_SUPPINFO_FIG2.PDF”]

1731 **Figure S2:** Measured section through the Sixmile Canyon Formation (Indianola Group) and
1732 (extrapolated) Price River Conglomerate at Mellor Canyon.

1733

1734 **S4 Field data**

1735 Palaeohydrologic field data collection was primarily focused on grain-size and cross-set measurements
1736 but, as mentioned, additionally included measurement of channel geometries and palaeocurrent
1737 indicators. In this section raw field data are presented for grain-size measurements (Table S2) and
1738 cross-set measurements (Table S3), as these are the data that we propagate through our quantitative
1739 palaeohydrologic framework to reconstruct various palaeohydrologic parameters (see Methods). Data
1740 are tabulated and subdivided by field area and stratigraphic interval. First, extended information
1741 pertaining to grain-size data collection is presented.

1742 *Grain-Size*

1743 At each field site, the coarse-fraction (>2 mm in diameter) and sand-fraction (<2 mm in diameter)
1744 grain-size of channel-fill deposits was established (Fig. 3a,b in main text). For coarse-fractions (>2 mm),
1745 grain-size distributions were measured via Wolman point counts (Wolman, 1954). For each count, 100
1746 clasts were randomly selected across a 1 m² area of exposed outcrop (or 2 m², where grain-size was
1747 boulder-grade) and the long axis was measured (Fig. 3a). The long axis was measured as opposed to

1748 the intermediate axis because: (1) it is objectively easier, and more efficient, to identify and
 1749 consistently measure the long axis (Brooke et al., 2018; Watkins et al., 2020); (2) the ratio between
 1750 the long and intermediate axis is broadly constant in fluvial gravels, near 0.7 (e.g. Litty & Schlunegger,
 1751 2017; Litty et al., 2017); (3) any measured axis is an apparent axis given the arbitrary orientation of
 1752 the outcrop exposure, so it is therefore consistent and easiest to measure the longest observed. For
 1753 sand-fractions (<2 mm), scaled photographs were instead processed in *ImageJ* software and the long
 1754 axis of 50 randomly selected grains were similarly measured (Fig. 3b) (where sand-fractions were
 1755 poorly sorted 100 clasts were counted for certainty). Grain-size distributions were then used to
 1756 establish the median grain size, D_{50} , and 84th percentile, D_{84} . Finally, where grain-size facies in channel-
 1757 fill deposits were disparate, e.g. gravel topped with sand, data were collected for each grain-size facies
 1758 and the proportions of each facies were estimated (Fig. 3c).

1759 To recover spatio-temporal grain-size distribution trends along several time-averaged stratigraphic
 1760 intervals, it was crucial that representative time-averaged data were collected. Not only were grain-
 1761 size data collected for each grain-size facies (Fig. 3a–c), depending on overall outcrop extent Wolman
 1762 point counts were also repeated and/or additional scaled photographs were taken for *ImageJ*
 1763 processing at intermittent stratigraphic intervals (e.g. one count per 5–10 m of strata or per
 1764 channelized body). The extent of each field site can be approximated as the extent of outcrop
 1765 apparent in Fig. 3c–h. From these data an average sand-fraction grain size and an average gravel-
 1766 fraction grain size was produced for each field site. As each space–time interval includes multiple field
 1767 sites, this results in multiple average sand- and gravel-fraction grain-sizes per interval, encompassing
 1768 channel-fill deposits from several channelized bodies. Finally, weighted, bulk-grain size distribution
 1769 was produced for each space–time interval using the gravel- vs sand-fraction weightings at each field
 1770 site — each field site within a space–time interval was assigned equal weighting. For example, say
 1771 data were collected from two field sites for one space–time interval. If one of these sites was 100%
 1772 sand-grade, and the second site was 80% sand-grade and 20% gravel-grade, then the bulk grain-size
 1773 for that space–time interval would be calculated as follows: 50% would be the average sand-fraction
 1774 grain size at Site 1, 40% would be the average sand-fraction grain-size at Site 2, and 10% would be the
 1775 average gravel-fraction grain-size at Site 2.

1776

1777 **Table S2:** Grain-size data collected and used in this study. Bulk grain-sizes include both the sand
 1778 fraction grain-size and the gravel fraction grain-size, which are weighted according to their respective
 1779 facies proportions. Gravel fraction grain-sizes solely represent the gravel fraction. Where ‘N/A’ is
 1780 reported, this is the absence of data (due to lack of access) or, in the case of gravel fraction grain-sizes,
 1781 absence of a gravel fraction in the exposed outcrop. D_{50} and D_{84} represent the median and 84th
 1782 percentile of grain-size, respectively. Grain-size data are reported for each field location, through
 1783 stratigraphic intervals 1–7: 1 = lower Blackhawk Formation; 2 = middle Blackhawk Formation; 3 =
 1784 upper Blackhawk Formation; 4 = lower Castlegate Sandstone; 5 = middle Castlegate Sandstone; 6 =
 1785 upper Castlegate Sandstone (Bluecastle Tongue); 7 = (lowermost) Price River Formation.

Location and stratigraphic interval	Bulk grain-size		Gravel fraction grain-size	
	D_{50} (mm)	D_{84} (mm)	D_{50} (mm)	D_{84} (mm)
Lower Blackhawk Formation (1)	N/A	N/A	N/A	N/A

Bear Canyon	Middle Blackhawk Formation (2)	0.24	0.38	N/A	N/A
	Upper Blackhawk Formation (3)	0.22	0.30	N/A	N/A
	Lower Castlegate Sandstone (4)	0.26	0.36	N/A	N/A
	Middle Castlegate Sandstone (5)	0.19	0.26	74.92	166.21
	Upper Castlegate Sandstone (6)	0.34	5.00	10.00	15.00
	Price River Formation (7)	0.39	3.00	10.00	20.00
	Dry Hollow	Lower Blackhawk Formation (1)	N/A	N/A	N/A
Middle Blackhawk Formation (2)		35.00	65.00	35.00	65.00
Upper Blackhawk Formation (3)		35.00	65.00	35.00	65.00
Lower Castlegate Sandstone (4)		65.00	126.5	65.00	126.5
Middle Castlegate Sandstone (5)		67.00	147.5	80.00	179.00
Upper Castlegate Sandstone (6)		67.00	147.5	80.00	179.00
Price River Formation (7)		N/A	N/A	N/A	N/A
Lake Fork	Lower Blackhawk Formation (1)	N/A	N/A	N/A	N/A
	Middle Blackhawk Formation (2)	N/A	N/A	N/A	N/A
	Upper Blackhawk Formation (3)	N/A	N/A	N/A	N/A
	Lower Castlegate Sandstone (4)	30.00	50.00	30.00	50.00
	Middle Castlegate Sandstone (5)	30.00	60.00	30.00	63.00
	Upper Castlegate Sandstone (6)	30.00	60.00	30.00	63.00
	Price River Formation (7)	13.00	46.50	32.00	60.00
Link Canyon	Lower Blackhawk Formation (1)	0.31	0.43	N/A	N/A
	Middle Blackhawk Formation (2)	0.30	0.56	N/A	N/A
	Upper Blackhawk Formation (3)	0.27	0.40	N/A	N/A
	Lower Castlegate Sandstone (4)	0.62	1.55	5.00	9.00
	Middle Castlegate Sandstone (5)	0.27	0.42	N/A	N/A
	Upper Castlegate Sandstone (6)	0.25	0.31	N/A	N/A
	Price River Formation (7)	0.14	0.18	N/A	N/A
Mellor Canyon	Lower Blackhawk Formation (1)	10.00	30.00	20.00	36.00
	Middle Blackhawk Formation (2)	10.00	30.00	20.00	36.00
	Upper Blackhawk Formation (3)	10.00	30.00	20.00	36.00
	Lower Castlegate Sandstone (4)	24.00	52.00	34.00	65.00
	Middle Castlegate Sandstone (5)	24.00	52.00	34.00	65.00
	Upper Castlegate Sandstone (6)	24.00	52.00	34.00	65.00
	Price River Formation (7)	24.00	52.00	34.00	65.00
Price Canyon	Lower Blackhawk Formation (1)	N/A	N/A	N/A	N/A
	Middle Blackhawk Formation (2)	N/A	N/A	N/A	N/A
	Upper Blackhawk Formation (3)	0.27	0.40	N/A	N/A
	Lower Castlegate Sandstone (4)	0.18	0.25	13.00	30.00
	Middle Castlegate Sandstone (5)	0.17	0.21	N/A	N/A
	Upper Castlegate Sandstone (6)	0.26	0.39	N/A	N/A
	Price River Formation (7)	0.32	0.72	6.00	11.00
Salina Canyon	Lower Blackhawk Formation (1)	0.13	0.17	N/A	N/A
	Middle Blackhawk Formation (2)	0.49	0.67	N/A	N/A

	Upper Blackhawk Formation (3)	0.39	0.58	3.94	7.00
	Lower Castlegate Sandstone (4)	0.48	1.03	6.00	10.00
	Middle Castlegate Sandstone (5)	0.28	0.71	6.00	14.00
	Upper Castlegate Sandstone (6)	0.32	0.41	N/A	N/A
	Price River Formation (7)	0.31	0.38	N/A	N/A
Sixmile Canyon	Lower Blackhawk Formation (1)	0.29	0.68	22.00	40.00
	Middle Blackhawk Formation (2)	0.29	0.68	22.00	40.00
	Upper Blackhawk Formation (3)	0.29	0.68	22.00	40.00
	Lower Castlegate Sandstone (4)	0.81	15.00	18.00	35.00
	Middle Castlegate Sandstone (5)	0.81	15.00	18.00	35.00
	Upper Castlegate Sandstone (6)	0.81	15.00	18.00	35.00
	Price River Formation (7)	0.43	5.00	8.00	15.00
Straight Canyon	Lower Blackhawk Formation (1)	0.37	0.48	N/A	N/A
	Middle Blackhawk Formation (2)	0.24	0.32	N/A	N/A
	Upper Blackhawk Formation (3)	0.23	0.32	N/A	N/A
	Lower Castlegate Sandstone (4)	0.64	0.97	N/A	N/A
	Middle Castlegate Sandstone (5)	0.46	11.00	10.00	23.00
	Upper Castlegate Sandstone (6)	0.34	0.52	6.00	10.00
	Price River Formation (7)	N/A	N/A	N/A	N/A
Wattis Road	Lower Blackhawk Formation (1)	0.24	0.28	N/A	N/A
	Middle Blackhawk Formation (2)	0.26	0.30	N/A	N/A
	Upper Blackhawk Formation (3)	0.29	0.36	N/A	N/A
	Lower Castlegate Sandstone (4)	0.39	0.49	N/A	N/A
	Middle Castlegate Sandstone (5)	0.26	0.35	N/A	N/A
	Upper Castlegate Sandstone (6)	0.24	0.30	N/A	N/A
	Price River Formation (7)	N/A	N/A	N/A	N/A

1786

1787

1788 **Table S3:** Cross-set data collected and used in this study. Mean cross-set heights are estimated from
1789 mean maximum cross-set heights (see Methods). Where 'N/A' is reported, this is the absence of data
1790 (due to lack of access) or, rarely, absence of cross-sets. Cross-set data are reported for each field
1791 location, through stratigraphic intervals 1–7: 1 = lower Blackhawk Formation; 2 = middle Blackhawk
1792 Formation; 3 = upper Blackhawk Formation; 4 = lower Castlegate Sandstone; 5 = middle Castlegate
1793 Sandstone; 6 = upper Castlegate Sandstone (Bluecastle Tongue); 7 = (lowermost) Price River Formation.

Location and stratigraphic interval		Mean maximum cross-set height (m)	Predicted mean cross-set height (m)	Standard error on predicted mean cross-set height (m)	Number of cross-sets measured
Bear Canyon	Lower Blackhawk Formation (1)	N/A	N/A	N/A	N/A

	Middle Blackhawk Formation (2)	0.19	0.13	0.0039	123
	Upper Blackhawk Formation (3)	0.11	0.08	0.0012	117
	Lower Castlegate Sandstone (4)	0.13	0.09	0.0026	47
	Middle Castlegate Sandstone (5)	0.19	0.13	0.0091	28
	Upper Castlegate Sandstone (6)	0.23	0.16	0.0046	244
	Price River Formation (7)	0.18	0.13	0.0041	105
Dry Hollow	Lower Blackhawk Formation (1)	N/A	N/A	N/A	N/A
	Middle Blackhawk Formation (2)	N/A	N/A	N/A	N/A
	Upper Blackhawk Formation (3)	N/A	N/A	N/A	N/A
	Lower Castlegate Sandstone (4)	N/A	N/A	N/A	N/A
	Middle Castlegate Sandstone (5)	N/A	N/A	N/A	N/A
	Upper Castlegate Sandstone (6)	N/A	N/A	N/A	N/A
	Price River Formation (7)	N/A	N/A	N/A	N/A
Lake Fork	Lower Blackhawk Formation (1)	N/A	N/A	N/A	N/A
	Middle Blackhawk Formation (2)	N/A	N/A	N/A	N/A
	Upper Blackhawk Formation (3)	N/A	N/A	N/A	N/A
	Lower Castlegate Sandstone (4)	0.18	0.13	0.0250	2
	Middle Castlegate Sandstone (5)	0.12	0.08	0.0090	13
	Upper Castlegate Sandstone (6)	0.12	0.08	0.0090	13
	Price River Formation (7)	0.10	0.07	0.0089	8
Link Canyon	Lower Blackhawk Formation (1)	0.19	0.13	0.0046	94
	Middle Blackhawk Formation (2)	0.21	0.15	0.0112	54
	Upper Blackhawk Formation (3)	0.24	0.17	0.0064	83

	Lower Castlegate Sandstone (4)	0.24	0.17	0.0115	50
	Middle Castlegate Sandstone (5)	0.19	0.13	0.0061	56
	Upper Castlegate Sandstone (6)	0.22	0.15	0.0046	67
	Price River Formation (7)	0.22	0.15	0.0060	26
Mellor Canyon	Lower Blackhawk Formation (1)	0.17	0.12	0.0041	206
	Middle Blackhawk Formation (2)	0.17	0.12	0.0041	206
	Upper Blackhawk Formation (3)	0.17	0.12	0.0041	206
	Lower Castlegate Sandstone (4)	0.11	0.08	0.0028	62
	Middle Castlegate Sandstone (5)	0.11	0.08	0.0028	62
	Upper Castlegate Sandstone (6)	0.11	0.08	0.0028	62
	Price River Formation (7)	0.11	0.08	0.0028	62
Price Canyon	Lower Blackhawk Formation (1)	N/A	N/A	N/A	N/A
	Middle Blackhawk Formation (2)	N/A	N/A	N/A	N/A
	Upper Blackhawk Formation (3)	0.18	0.13	0.0053	104
	Lower Castlegate Sandstone (4)	0.16	0.12	0.0032	77
	Middle Castlegate Sandstone (5)	0.16	0.12	0.0032	58
	Upper Castlegate Sandstone (6)	0.18	0.13	0.0046	62
	Price River Formation (7)	0.29	0.20	0.0056	146
Salina Canyon	Lower Blackhawk Formation (1)	0.20	0.14	0.0046	34
	Middle Blackhawk Formation (2)	0.21	0.15	0.0046	21
	Upper Blackhawk Formation (3)	0.23	0.16	0.0054	77
	Lower Castlegate Sandstone (4)	0.22	0.15	0.0056	57
	Middle Castlegate Sandstone (5)	0.18	0.12	0.0033	140

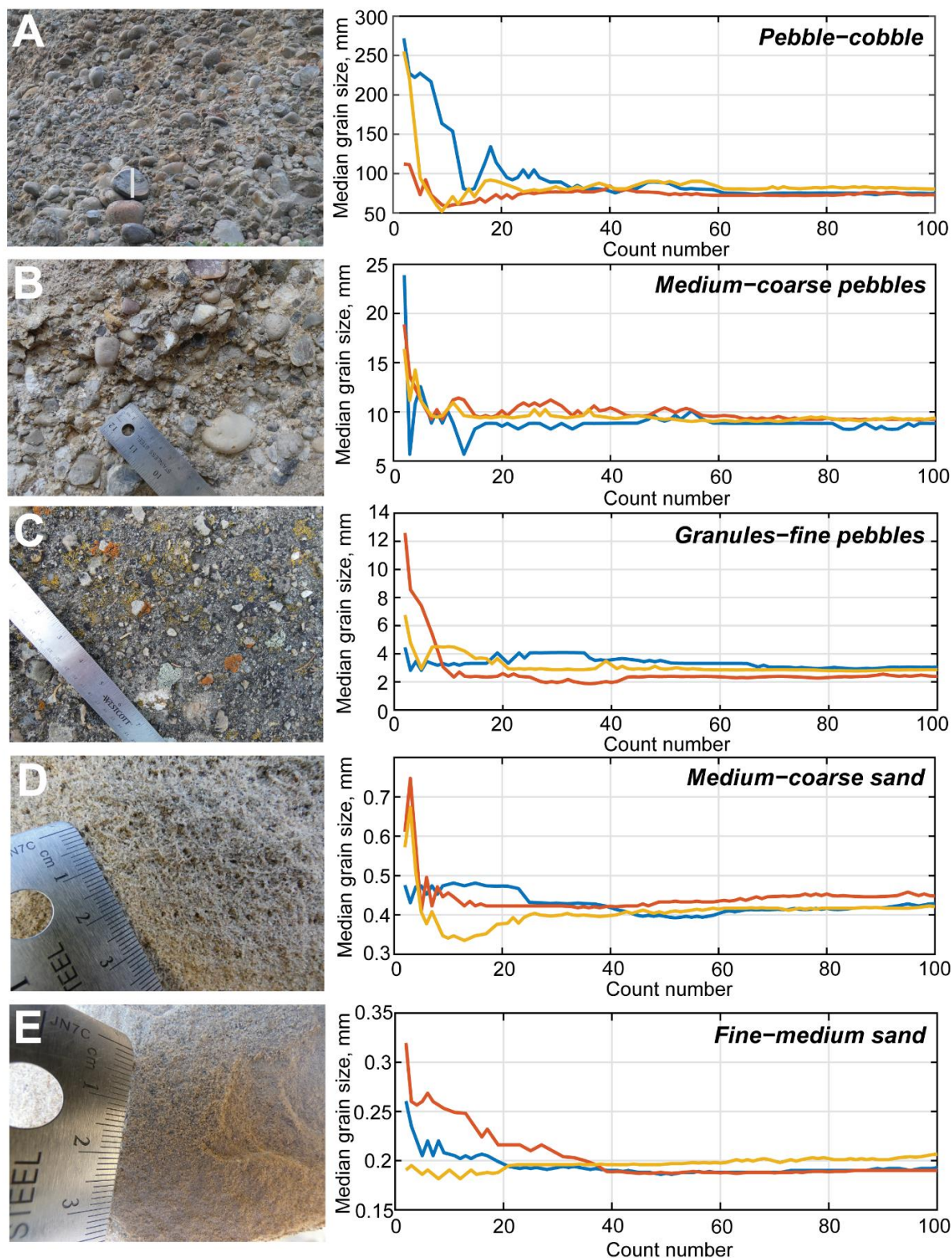
	Upper Castlegate Sandstone (6)	0.16	0.11	0.0030	106
	Price River Formation (7)	0.24	0.17	0.0072	41
Sixmile Canyon	Lower Blackhawk Formation (1)	0.35	0.25	0.0201	40
	Middle Blackhawk Formation (2)	0.35	0.25	0.0201	40
	Upper Blackhawk Formation (3)	0.35	0.25	0.0201	40
	Lower Castlegate Sandstone (4)	0.33	0.23	0.0185	76
	Middle Castlegate Sandstone (5)	0.33	0.23	0.0185	76
	Upper Castlegate Sandstone (6)	0.33	0.23	0.0185	76
	Price River Formation (7)	0.18	0.13	0.0047	37
Straight Canyon	Lower Blackhawk Formation (1)	0.25	0.18	0.0036	116
	Middle Blackhawk Formation (2)	0.20	0.14	0.0037	69
	Upper Blackhawk Formation (3)	0.19	0.13	0.0021	84
	Lower Castlegate Sandstone (4)	0.18	0.13	0.0031	52
	Middle Castlegate Sandstone (5)	0.16	0.11	0.0028	49
	Upper Castlegate Sandstone (6)	0.23	0.16	0.0037	107
	Price River Formation (7)	N/A	N/A	N/A	N/A
Wattis Road	Lower Blackhawk Formation (1)	0.17	0.12	0.0028	40
	Middle Blackhawk Formation (2)	0.18	0.12	0.0030	49
	Upper Blackhawk Formation (3)	0.18	0.12	0.0024	61
	Lower Castlegate Sandstone (4)	0.18	0.12	0.0034	33
	Middle Castlegate Sandstone (5)	0.16	0.11	0.0025	60
	Upper Castlegate Sandstone (6)	0.18	0.12	0.0037	29
	Price River Formation (7)	N/A	N/A	N/A	N/A

1794

1795 **S5. Grain-size sample sufficiency**

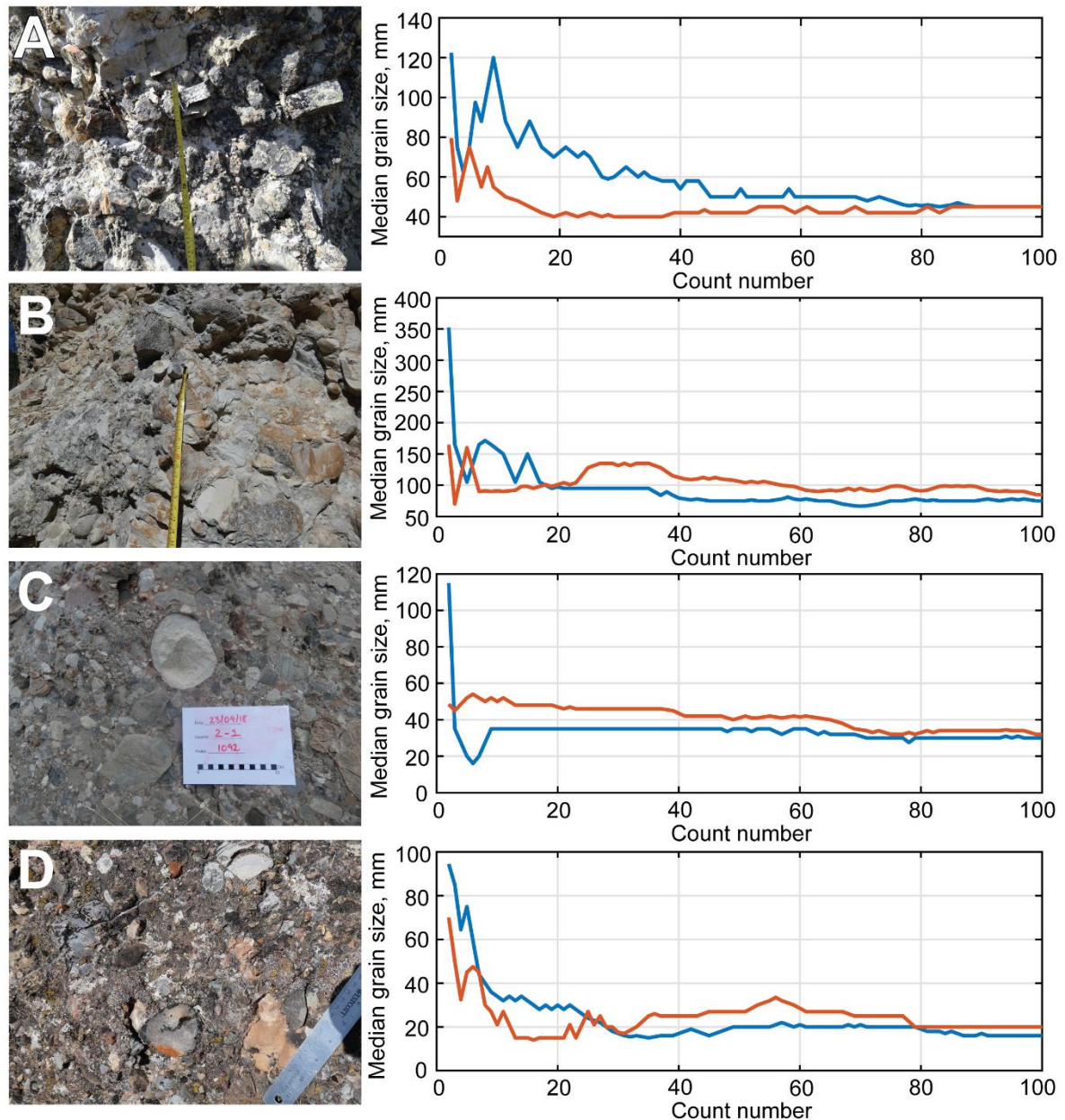
1796 Ancillary data collection was conducted to test whether grain-size sample size was sufficient. These
1797 tests determined that counts of 100 and 50 clasts for coarse-fractions and sand-fractions, respectively,
1798 successfully recovered stable D_{50} estimates.

1799 To check whether sample size in grain-size counts is sufficient, the iterative D_{50} was calculated to
1800 determine the number of counts required to produce stable estimates of D_{50} for each grain-size
1801 fraction (Figs S3, S4). D_{50} estimates were considered to be stable when the iterative D_{50} fluctuates
1802 within ~ 10 mm for boulder- and cobble-grade sediments, within $\sim 2\text{--}3$ mm for pebble-grade sediments
1803 and within ~ 0.1 mm for sand-grade sediments. Iterative estimates of D_{50} suggest that, for coarse-
1804 fractions, $< 80\text{--}90$ clast counts are sufficient to converge towards the median (Figs S3, S4), whereas for
1805 sand-fractions, $< 30\text{--}40$ counts are required (Fig. S3). Therefore, counts of 100 and 50 for coarse-
1806 fractions and sand-fractions, respectively, should successfully recover stable D_{50} estimates. However,
1807 where sand-fractions were poorly sorted 100 clasts were counted for certainty.



1808

1809 **Figure S3:** The iterative convergence of median grain-size for (A) pebbles-cobbles, (B) medium-coarse
 1810 pebbles, (C) granules-fine pebbles, (D) medium-coarse sand, and (E) fine-medium sand, as calculated
 1811 from scaled photographs in ImageJ software. Three repeat counts were taken for each scaled
 1812 photograph (red, blue and yellow solid lines). White bar in part A is 400 mm long.



1813

1814 **Figure S4:** The iterative convergence of median grain-size for different outcrops of gravel-grade
 1815 sediments (A–D), as calculated from field Wolman counts. Repeat counts were taken (red and blue
 1816 solid lines).

1817 **S6. Secondary field data**

1818 As discussed in the main text, extensive work in this region has already focused on measuring
 1819 geometries of architectural scale elements, which has increasingly exploited access to high-resolution
 1820 imagery and three-dimensional outcrop models (Hajek & Heller, 2012; Rittersbacher et al., 2014; Flood
 1821 & Hampson, 2015; Chamberlin & Hajek, 2019). These tools lend themselves to precise constraints on
 1822 architectural geometries. As such, to the decision was made to primarily focus on grain-size and cross-
 1823 set measurements in our field data collection, and secondary data providing constraints on
 1824 architectural geometries were subsequently compiled. Specifically, data were compiled for
 1825 independent indicators/proxies of palaeoflow depths (Table S4) and palaeoflow width (Table S5). The
 1826 latter is particularly difficult to constrain from outcrop and, as such, indicators of palaeoflow width

1827 tend to offer apparent widths, maximum widths, or a first-order sense as to the magnitude of width.
 1828 These secondary data are supplemented by some of our own field observations at each field locality,
 1829 where possible (Tables S4, S5), which were measured with a Haglof Laser Geo laser range finder to a
 1830 precision of ± 5 cm.

1831 Given that we implement our field data in an entirely quantitative framework, independent
 1832 observations and measurements of palaeoflow depths and palaeoflow widths are useful to
 1833 corroborate estimates from this study (see Results). In addition, these constraints on the approximate,
 1834 or order-of-magnitude, widths of these palaeorivers are further useful in probing the planform
 1835 morphologies of these systems in both space and time (see Results).

1836

1837 **Table S4:** A compilation of field measurements (secondary data from published literature) for
 1838 architectural scale elements, e.g. bar heights, that are commonly used as palaeoflow depth proxies.
 1839 For each secondary data set we include the stratigraphic interval it would be assigned in this study (1–
 1840 7) and the field location from which the data set was collected. 1 = lower Blackhawk Formation; 2 =
 1841 middle Blackhawk Formation; 3 = upper Blackhawk Formation; 4 = lower Castlegate Sandstone; 5 =
 1842 middle Castlegate Sandstone; 6 = upper Castlegate Sandstone (Bluecastle Tongue); 7 = Price River
 1843 Formation.

Stratigraphic interval	Location	Value (m)	Proxy	Reference
Lower Blackhawk Formation (1)	South of Straight Canyon	7	Mean apparent height of channelized fluvial sandstone bodies	Flood and Hampson (2015)
Middle Blackhawk Formation (2)	South of Straight Canyon	8	Mean apparent height of channelized fluvial sandstone bodies	Flood and Hampson (2015)
Upper Blackhawk Formation (3)	South of Straight Canyon	7, 6	Mean apparent height of channelized fluvial sandstone bodies	Flood and Hampson (2015)
Blackhawk Formation (1–3)	Link Canyon	2 to >14	Channel story height	Hampson et al. (2013)
Blackhawk Formation (1–3)	Salina Canyon	0.5–2	Fining upward bed sets	Adams and Bhattacharya (2005)
Blackhawk Formation (1–3)	Salina Canyon	1–2	Bar heights	Adams and Bhattacharya (2005)
Blackhawk Formation (1–3)	Salina Canyon	5–8	Channel-belt sandstone body heights	Adams and Bhattacharya (2005)
Lower Castlegate Sandstone (4)	Price Canyon	4.1	Mean bar height	Hajek and Heller (2012)

Lower Castlegate Sandstone (4)	Price Canyon	1.1–7.6	Bar height	McLaurin and Steel (2007)
Lower Castlegate Sandstone (4)	Price Canyon	4.1 (1.5 to >8)	Mean bar height (and range)	Lynds and Hajek (2006)
Castlegate Sandstone (4–6)	Price Canyon	2.6	Mean bar height	Chamberlin and Hajek (2019)
Castlegate Sandstone (4–6)	Straight Canyon	3.6	Mean bar height	Chamberlin and Hajek (2019)
Castlegate Sandstone (4–6)	Salina Canyon	3.9	Mean bar height	Chamberlin and Hajek (2019)
Castlegate Sandstone (4–6)	Salina Canyon	1.5–2	Bar heights	Adams and Bhattacharya (2005)
Castlegate Sandstone (4–6)	Salina Canyon	3–5	Channel story heights	Adams and Bhattacharya (2005)
Blackhawk Formation (1–3)	Bear Canyon	2.1, 2.5, 3.9, 2.3, 1.8, 3.1, 3.5, 3.6, 2.5, 1.6, 2.5, 2.3, 1.5, 2.6	Lateral accretion set heights/channelized fluvial sandstone body heights	This study
Blackhawk Formation (1–3)	Salina Canyon	3.5, 4.6, 2, 2.1, 2.7, 5.8, 7.5, 3.7, 5.8, 6.6, 6.7	Lateral accretion set heights/channelized fluvial sandstone body heights	This study
Blackhawk Formation (1–3)	Link Canyon	3, 5.1, 5.4, 4.8, 4.7, 3.5, 2.1, 3, 4.5, 3.1, 3.2, 2.2, 1.5, 2.5, 3.3, 3.8, 4.4, 4.5, 3.2	Lateral accretion set heights/channelized fluvial sandstone body heights	This study
Blackhawk Formation (1–3)	Price Canyon	2.4, 2.3, 1.9, 1.9, 1.7, 1.6, 1.5	Lateral accretion set heights/channelized fluvial sandstone body heights	This study
Blackhawk Formation (1–3)	Straight Canyon	3.5, 5, 2, 3.5, 6.7, 3, 6, 3.7	Lateral accretion set heights/channelized fluvial sandstone body heights	This study

Blackhawk Formation (1–3)	Wattis Road	2.2, 3.5, 2.3, 2, 2.4, 1.7	Lateral accretion set heights/channelized fluvial sandstone body heights	This study
Castlegate Sandstone (4–6)	Bear Canyon	4, 6.4, 2.8, 2.9, 4.7, 3.4, 2.9, 4.1, 3.2, 2.1, 2.1	Lateral accretion set heights/channelized fluvial sandstone body heights	This study
Castlegate Sandstone (4–6)	Price Canyon	3.4, 3, 3.5, 2, 2.2, 2.8, 3	Lateral accretion set heights/channelized fluvial sandstone body heights	This study
Castlegate Sandstone (4–6)	Wattis Road	3.9, 4	Lateral accretion set heights/channelized fluvial sandstone body heights	This study
Castlegate Sandstone (4–6)	Salina Canyon	1.6, 2.8, 2.2, 2, 3.8, 3.2, 2.3, 2.8, 1.9, 3.7, 2.4, 2.3, 2.6, 4.1	Lateral accretion set heights/channelized fluvial sandstone body heights	This study
Castlegate Sandstone (4–6)	Link Canyon	1.6, 3.6, 2.3, 4.3, 3.1, 3.6, 2, 3.8, 0.75, 1.1, 1.1, 1.3, 2.4, 2.5	Lateral accretion set heights/channelized fluvial sandstone body heights	This study
Price River Formation (1–3)	Price Canyon	7	Lateral accretion set heights/channelized fluvial sandstone body heights	This study
Price River Formation (7)	Bear Canyon	3.7, 2.1, 2.4, 2.15, 4.1, 5.2, 0.9, 2.2, 1.4	Lateral accretion set heights/channelized fluvial sandstone body heights	This study

1844

1845 **Table S5:** A compilation of field measurements (secondary data from published literature) for
1846 architectural scale elements, e.g. sandstone bodies, that are commonly used as a proxy to infer the
1847 magnitude of channel width. For each secondary data set we include the stratigraphic interval it would
1848 be assigned in this study (1–7) and the field location from which the data set was collected. 1 = lower
1849 Blackhawk Formation; 2 = middle Blackhawk Formation; 3 = upper Blackhawk Formation; 4 = lower

1850 *Castlegate Sandstone; 5 = middle Castlegate Sandstone; 6 = upper Castlegate Sandstone (Bluecastle*
 1851 *Tongue); 7 = (lowermost) Price River Formation.*

Stratigraphic interval	Location	Value (m)	Proxy	Reference
Lower Blackhawk Formation (1)	South of Straight Canyon	350	Mean apparent width of channelized fluvial sandstone bodies	Flood and Hampson (2015)
Middle Blackhawk Formation (2)	South of Straight Canyon	370	Mean apparent width of channelized fluvial sandstone bodies	Flood and Hampson (2015)
Upper Blackhawk Formation (3)	South of Straight Canyon	420, 390	Mean apparent width of channelized fluvial sandstone bodies	Flood and Hampson (2015)
Blackhawk Formation (1–3)	Link Canyon	30 to >310	Channel story widths	Hampson et al. (2013)
Blackhawk Formation (1–3)	Link Canyon	>120 to >740	Channel belt widths	Hampson et al. (2013)
Blackhawk Formation (1–3)	Salina Canyon	8~50	Bar widths	Adams and Bhattacharya (2005)
Lower Castlegate Sandstone (4)	Price Canyon	30, 35 (max >100)	Thalweg and bar widths	McLaurin and Steel (2007)
Castlegate Sandstone (4–6)	Price Canyon	58	Mean bar package width	Chamberlin and Hajek (2019)
Castlegate Sandstone (4–6)	Straight Canyon	180	Mean bar package width	Chamberlin and Hajek (2019)
Castlegate Sandstone (4–6)	Salina Canyon	87	Mean bar package width	Chamberlin and Hajek (2019)

1852

1853

1854 **S7. Goodness of fits on palaeoslope profiles inc. resolved steepness indexes**

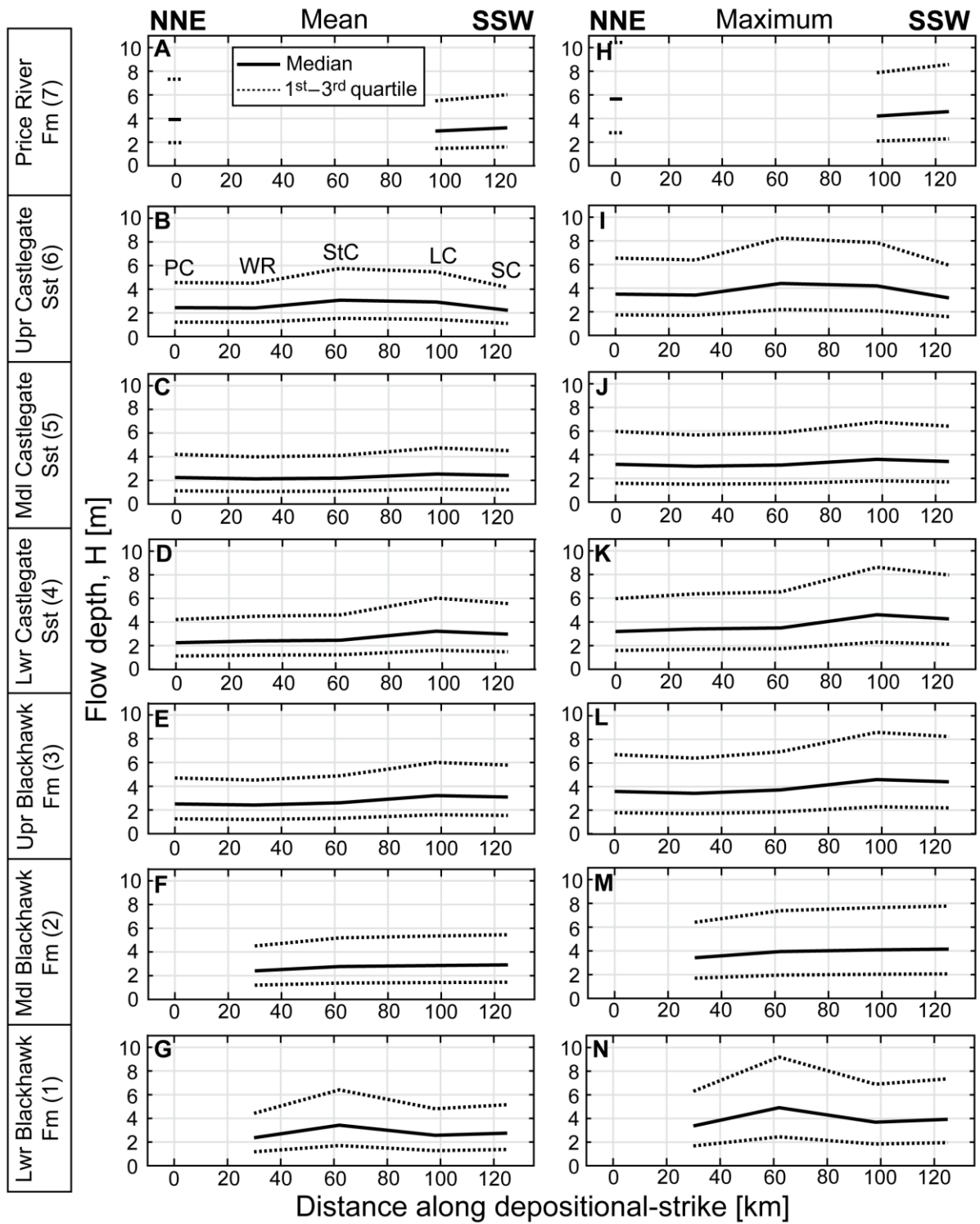
1855 As described in the Methods, palaeorelief was reconstructed in the alluvial domain of Late Cretaceous
 1856 central Utah palaeorivers. Initially, palaeoslope was reconstructed using 2 independent methods, a
 1857 Shields stress inversion (Equation 3) and the approach of Trampush et al. (2014) (Equation 4).
 1858 Palaeoslope estimates from each method were then used to estimate palaeorelief (see Methods and
 1859 Results). In doing so, we a non-linear least squares regression was used to derive best-fit palaeoslope

1860 profiles for the defined northern and southern transects using Equation 7. In doing so, three different
1861 values for the concavity index, θ , were assumed given that concavity in these ancient rivers is not
1862 known. Plausible values of 0.4, 0.5 and 0.6 were used for θ . Using the two sets of palaeoslope
1863 estimates (Equations 3 and 4) and the three different concavity values, a variety of steepness indexes,
1864 k_s (Equation 7), were recovered for the defined northern and southern depositional-dip transects, for
1865 each stratigraphic interval (where possible). These results are presented here; Table S6 details all k_s
1866 values recovered when reconstructing best-fit palaeoslope profiles, and also reports goodness of fit
1867 (R^2).

1868 **Table S6:** Steepness indexes, k_s , recovered for the defined northern and southern depositional-dip transects, through each stratigraphic interval (1–7), where
 1869 possible. 1 = l Blackhawk Formation; 2 = middle Blackhawk Formation; 3 = upper Blackhawk Formation; 4 = lower Castlegate Sandstone; 5 = middle Castlegate
 1870 Sandstone; 6 = upper Castlegate Sandstone (Bluecastle Tongue); 7 = (lowermost) Price River Formation. k_s values are calculated using palaeoslope estimates
 1871 derived from both Equations 3 and 4, and using a concavity index, θ , of either 0.4, 0.5, or 0.6. R^2 values are given for each k_s value.

Transect	Stratigraphic interval	Concavity index, θ											
		0.4				0.5				0.6			
		Shields stress inversion (Equation 3)		Trampush et al. 2014 (Equation 4)		Shields stress inversion (Equation 3)		Trampush et al. 2014 (Equation 4)		Shields stress inversion (Equation 3)		Trampush et al. 2014 (Equation 4)	
k_s (m ^{0.8})	R^2	k_s (m ^{0.8})	R^2	k_s (m ¹)	R^2	k_s (m ¹)	R^2	k_s (m ^{1.2})	R^2	k_s (m ^{1.2})	R^2		
Northern transect	Price River Fm (7)	18.3	0.67	12.3	0.81	34.9	0.77	23.1	0.89	64.7	0.84	42.4	0.94
	Upper Castlegate Sst (6)	16.4	0.34	10.2	0.91	22.5	0.25	14.6	0.88	30.2	0.16	20.3	0.82
	Middle Castlegate Sst (5)	16.4	0.34	10.3	0.91	22.5	0.25	14.6	0.88	30.2	0.17	20.3	0.82
	Lower Castlegate Sst (4)	14.1	0.58	9.6	0.99	19.6	0.5	13.8	0.98	26.7	0.41	19.3	0.95
	Upper Blackhawk Fm (3)	6.1	0.98	8.3	0.99	8.6	0.99	11.6	0.98	12.0	0.99	16.0	0.96
	Middle Blackhawk Fm (2)	6.1	0.96	8.1	0.98	8.6	0.99	11.4	0.99	11.9	0.99	15.8	0.99
	Lower Blackhawk Fm (1)	N/A	N/A	N/A	N/A	N/A	N/A	N/A	N/A	N/A	N/A	N/A	N/A
Southern transect	Price River Fm (7)	15.8	0.90	5.9	0.98	22.6	0.95	8.4	0.99	31.8	0.98	11.7	0.99
	Upper Castlegate Sst (6)	15.3	0.88	5.8	0.94	22.2	0.94	8.3	0.97	31.5	0.97	11.6	0.98
	Middle Castlegate Sst (5)	15.4	0.88	5.9	0.92	22.4	0.94	8.4	0.94	31.6	0.97	11.7	0.94
	Lower Castlegate Sst (4)	15.4	0.88	5.9	0.93	22.3	0.94	8.4	0.95	31.6	0.97	11.7	0.94
	Upper Blackhawk Fm (3)	3.5	0.91	3.1	0.89	5.1	0.96	4.4	0.89	7.2	0.98	6.1	0.86
	Middle Blackhawk Fm (2)	3.5	0.91	3.1	0.90	5.1	0.96	4.3	0.90	7.2	0.98	6.0	0.88
	Lower Blackhawk Fm (1)	3.5	0.90	3.0	0.91	5.1	0.95	4.3	0.92	7.2	0.98	6.0	0.91

1872



1874

1875 **Figure S5:** Reconstructed palaeoflow depths for the 5 parallel fluvial systems, for each stratigraphic
 1876 interval where possible. Parts A–G depict reconstructed palaeoflow depths from estimated mean cross-
 1877 set heights, whereas parts H–N depict reconstructed palaeoflow depths from measured maximum
 1878 cross-set heights. Results are presented as along-depositional strike transects from NNE (left; 0 km) to
 1879 SSW (right; 125 km). Field sites span Price Canyon (PC), Wattis Road (WR), Straight Canyon (StC), Link

1880 Canyon (LC) and Salina Canyon (SC). Solid lines indicate median palaeoflow depths and dashed lines
1881 indicated the 1st and 3rd quartiles of palaeoflow depths.

1882

1883 Adams, M. M., & Bhattacharya, J. P. (2005). No change in fluvial style across a sequence boundary, Cretaceous
1884 Blackhawk and Castlegate formations of central Utah, U.S.A. *Journal of Sedimentary Research*, 75(6),
1885 1038-1051. doi:10.2110/jsr.2005.080

1886 Aschoff, J., & Steel, R. (2011a). Anatomy and development of a low-accommodation clastic wedge, upper
1887 Cretaceous, Cordilleran Foreland Basin, USA. *Sedimentary Geology*, 236(1), 1-24.
1888 doi:10.1016/j.sedgeo.2010.10.006

1889 Aschoff, J., & Steel, R. (2011b). Anomalous clastic wedge development during the Sevier-Laramide transition,
1890 North American Cordilleran foreland basin, USA. *GSA Bulletin*, 123(9-10), 1822-1835.
1891 doi:10.1130/B30248.1

1892 Brooke, S. A. S., Whittaker, A., Armitage, J. J., D'Arcy, M., & Watkins, S. E. (2018). Quantifying sediment
1893 transport dynamics on alluvial fans from spatial and temporal changes in grain size, Death Valley,
1894 California. *Journal of Geophysical Research: Earth Surface*, 123, 2039-2067.

1895 Chamberlin, E. P., & Hajek, E. A. (2019). Using bar preservation to constrain reworking in channel-dominated
1896 fluvial stratigraphy. *Geology*, 47(6), 531-534. doi:10.1130/G46046.1

1897 Cobban, W. A., McKinney, K. C., Obradovich, J. D., & Walasczyk, I. (2006). A USGS zonal table for the Upper
1898 Cretaceous Middle Cenomanian–Maastrichtian of the Western Interior of the United States based on
1899 Ammonites, Inoceramids, and radiometric ages: U.S. Geological Survey, Open-File Report 2006-1250.
1900 1-46.

1901 Flood, Y. S., & Hampson, G. J. (2014). Facies and architectural analysis to interpret avulsion style and variability:
1902 Upper Cretaceous Blackhawk Formation, Wasatch Plateau, central Utah, U.S.A. *Journal of*
1903 *Sedimentary Research*, 84(9), 743-762. doi:10.2110/jsr.2014.59

1904 Flood, Y. S., & Hampson, G. J. (2015). Quantitative analysis of the dimensions and distribution of channelized
1905 fluvial sandbodies within a large outcrop dataset: Upper Cretaceous Blackhawk Formation, Wasatch
1906 Plateau, central Utah, U.S.A. *Journal of Sedimentary Research*, 85(4), 315-336.
1907 doi:10.2110/jsr.2015.25

1908 Fouch, T. D., Lawton, T. F., Nichols, D. J., Cashion, W. B., & Cobban, W. A. (1983). Patterns and timing of
1909 synorogenic sedimentation in Upper Cretaceous rocks of central and northeast Utah. In M. W.
1910 Reynolds & E. D. Dolly (Eds.), *Mesozoic Paleogeography of West-Central United States* (pp. 305-336):
1911 SEPM Rocky Mountain Section.

1912 Gill, J. R., & Hail Jr, W. J. (1975). Stratigraphic sections across Upper Cretaceous Mancos Shale-Mesaverde
1913 Group boundary, eastern Utah and western Colorado. *U.S. Geological Survey Publication*, 68.
1914 doi:10.3133/oc68

1915 Hajek, E. A., & Heller, P. L. (2012). Flow-depth scaling in alluvial architecture and nonmarine sequence
1916 stratigraphy: Example from the Castlegate Sandstone, central Utah, U.S.A. *Journal of Sedimentary*
1917 *Research*, 82(2), 121-130. doi:10.2110/jsr.2012.8

1918 Hampson, G. J. (2010). Sediment dispersal and quantitative stratigraphic architecture across an ancient shelf.
1919 *Sedimentology*, 57(1), 96-141. doi:10.1111/j.1365-3091.2009.01093.x

1920 Hampson, G. J., Duller, R. A., Petter, A. L., Robinson, R. A. J., & Allen, P. A. (2014). Mass-balance constraints on
1921 stratigraphic interpretation of linked alluvial–coastal–shelfal deposits from source to sink: example
1922 from Cretaceous Western Interior Basin, Utah and Colorado, U.S.A. *Journal of Sedimentary Research*,
1923 84(11), 935-960. doi:10.2110/jsr.2014.78

1924 Hampson, G. J., Jewell, T. O., Irfan, N., Gani, M. R., & Bracken, B. (2013). Modest change in fluvial style with
1925 varying accommodation in regressive alluvial-to-coastal-plain wedge: Upper Cretaceous Blackhawk
1926 Formation, Wasatch Plateau, central Utah, U.S.A. *Journal of Sedimentary Research*, 83(2), 145-169.
1927 doi:10.2110/jsr.2013.8

- 1928 Hampson, G. J., Royhan Gani, M., Sahoo, H., Rittersbacher, A., Irfan, N., Ranson, A., . . . Bracken, B. (2012).
1929 Controls on large-scale patterns of fluvial sandbody distribution in alluvial to coastal plain strata:
1930 Upper Cretaceous Blackhawk Formation, Wasatch Plateau, Central Utah, USA. *Sedimentology*, 59(7),
1931 2226-2258. doi:10.1111/j.1365-3091.2012.01342.x
- 1932 Horton, B. K., Constenius, K. N., & DeCelles, P. G. (2004). Tectonic control on coarse-grained foreland-basin
1933 sequences: An example from the Cordilleran foreland basin, Utah. *Geology*, 32(7), 637-640.
1934 doi:10.1130/G20407.1
- 1935 Lawton, T. F. (1982). Lithofacies correlations within the Upper Cretaceous Indianola Group, central Utah. *Utah*
1936 *Geological Association Publication*, 10, 199-213.
- 1937 Lawton, T. F. (1983). Late Cretaceous fluvial systems and the age of foreland uplifts in central Utah. In J. D.
1938 Lowell (Ed.), *Rocky Mountain Foreland Basins and Uplifts* (pp. 181-199). Denver: Rocky Mountain
1939 Association of Geologists.
- 1940 Lawton, T. F. (1986a). Compositional trends within a clastic wedge adjacent to a fold-thrust belt: Indianola
1941 Group, central Utah, USA. In P. A. Allen & P. Homewood (Eds.), *Foreland Basins* (pp. 411-423).
1942 London: Blackwell.
- 1943 Lawton, T. F. (1986b). Fluvial Systems of the Upper Cretaceous Mesaverde Group and Paleocene North Horn
1944 Formation, Central Utah: A Record of Transition from Thin-Skinned to Thick-Skinned Deformation in
1945 the Foreland Region. In J. A. Peterson (Ed.), *Paleotectonics and sedimentation in the Rocky Mountain*
1946 *Region, United States (Vol. 41): American Association of Petroleum Geologists*.
1947 doi:10.1306/M41456C20
- 1948 Lawton, T. F., Pollock, S. L., & Robinson, R. A. J. (2003). Integrating sandstone petrology and nonmarine
1949 sequence stratigraphy: application to the Late Cretaceous fluvial systems of southwestern Utah, USA.
1950 *Journal of Sedimentary Research*, 73, 398-406.
- 1951 Litty, C., & Schlunegger, F. (2017). Controls on pebbles' size and shape in streams of the Swiss Alps. *The Journal*
1952 *of Geology*, 125(1), 101-112. doi:10.1086/689183
- 1953 Litty, C., Schlunegger, F., & Viveen, W. (2017). Possible threshold controls on sediment grain properties of
1954 Peruvian coastal river basins. *Earth Surf. Dynam.*, 5(3), 571-583. doi:10.5194/esurf-5-571-2017
- 1955 Lynds, R., & Hajek, E. (2006). Conceptual model for predicting mudstone dimensions in sandy braided-river
1956 reservoirs. *AAPG Bulletin*, 90(8), 1273-1288. doi:10.1306/03080605051
- 1957 McLaurin, B. T., & Steel, R. J. (2007). Architecture and origin of an amalgamated fluvial sheet sand, lower
1958 Castlegate Formation, Book Cliffs, Utah. *Sedimentary Geology*, 197(3), 291-311.
1959 doi:10.1016/j.sedgeo.2006.10.005
- 1960 Miall, A. D. (1994). Reconstructing fluvial macroform architecture from two-dimensional outcrops; examples
1961 from the Castlegate Sandstone, Book Cliffs, Utah. *Journal of Sedimentary Research*, 64(2b), 146-158.
1962 doi:10.1306/D4267F78-2B26-11D7-8648000102C1865D
- 1963 Miall, A. D., & Arush, M. (2001). The Castlegate Sandstone of the Book Cliffs, Utah: Sequence stratigraphy,
1964 paleogeography, and tectonic controls. *Journal of Sedimentary Research*, 71(4), 537-548.
1965 doi:10.1306/103000710537
- 1966 Rittersbacher, A., Howell, J. A., & Buckley, S. J. (2014). Analysis of fluvial architecture in the Blackhawk
1967 Formation, Wasatch Plateau, Utah, U.S.A., using large 3D photorealistic models. *Journal of*
1968 *Sedimentary Research*, 84(2), 72-87. doi:10.2110/jsr.2014.12
- 1969 Robinson, R. A. J., & Slingerland, R. L. (1998). Grain-size trends, basin subsidence and sediment supply in the
1970 Campanian Castlegate Sandstone and equivalent conglomerates of Central Utah. *Basin Research*, 10,
1971 109-127.
- 1972 Seymour, D. L., & Fielding, C. R. (2013). High resolution correlation of the Upper Cretaceous stratigraphy
1973 between the Book Cliffs and the western Henry Mountains syncline, Utah, U.S.A. *Journal of*
1974 *Sedimentary Research*, 83(6), 475-494. doi:10.2110/jsr.2013.37

- 1975 Trampush, S. M., Huzurbazar, S., & McElroy, B. (2014). Empirical assessment of theory for bankfull
1976 characteristics of alluvial channels. *Water Resources Research*, 50(12), 9211-9220.
1977 doi:10.1002/2014WR015597
- 1978 Valora, P. M. (2010). *Late Cretaceous to Paleocene Tectono-Stratigraphic Evolution of the Southern Part of the*
1979 *Provo Salient, Sevier Fold-Thrust Belt, Central Utah: New Insights from Geologic Mapping, Growth-*
1980 *Strata Analysis and Structural Modeling in the Thistle, UT 7.5' Quadrangle.* (M.S. thesis), Colorado
1981 School of Mines, Golden, Colorado.
- 1982 van Wagoner, J. C. (1995). Sequence Stratigraphy and Marine to Nonmarine Facies Architecture of Foreland
1983 Basin Strata, Book Cliffs, Utah, U.S.A. In J. C. van Wagoner & G. T. Bertram (Eds.), *Sequence*
1984 *Stratigraphy of Foreland Basin Deposits: Outcrop and Subsurface Examples from the Cretaceous of*
1985 *North America* (Vol. 64): American Association of Petroleum Geologists.
- 1986 Watkins, S. E., Whittaker, A. C., Bell, R. E., Brooke, S. A. S., Ganti, V., Gawthorpe, R. L., . . . Nixon, C. W. (2020).
1987 Straight from the source's mouth: Controls on field-constrained sediment export across the entire
1988 active Corinth Rift, central Greece. *Basin Research*, n/a(n/a). doi:10.1111/bre.12444
- 1989 Wolman, M. G. (1954). A method of sampling coarse river-bed material. *Eos Transactions American*
1990 *Geophysical Union*, 35(6), 951-956. doi:10.1029/TR035i006p00951
- 1991 Yoshida, S., Willis, A., & Miall, A. D. (1996). Tectonic control of nested sequence architecture in the Castlegate
1992 Sandstone (Upper Cretaceous), Book Cliffs, Utah. *Journal of Sedimentary Research*, 66(4), 737-748.
- 1993